



Title	Study on Efficient Water Oxidation under Modal Strong Coupling Conditions
Author(s)	曹, 艶鳳
Citation	北海道大学. 博士(情報科学) 甲第14591号
Issue Date	2021-03-25
DOI	10.14943/doctoral.k14591
Doc URL	http://hdl.handle.net/2115/81411
Type	theses (doctoral)
File Information	Yanfeng_Cao.pdf



[Instructions for use](#)

Study on Efficient Water Oxidation under Modal Strong Coupling Conditions

Thesis by

Yanfeng Cao

In Partial Fulfillment of the Requirements

for the Degree of

Doctor of Philosophy



GRADUATE SCHOOL OF INFORMATION SCIENCE AND

TECHNOLOGY

HOKKAIDO UNIVERSITY

SAPPORO, JAPAN

2021

Dedication

This thesis is dedicated to my family for their endless love.

Table of Contents

Acknowledgements	1
Thesis Abstract.....	3
Chapter 1 Introduction	6
1.1 Background and motivation	6
1.2 Surface plasmon resonance	7
1.2.1 SPR in noble metal nanostructures.....	8
1.2.2 Characteristics of LSPR	13
1.2.3 Relaxation Processes of LSPR	18
1.2.4 Applications of LSPR.....	19
1.3 Fabrication of plasmonic nanostructures.....	21
1.3.1 Electron beam lithography	21
1.3.2 Chemical growth method	22
1.3.3 Other methods	24
1.4 Plasmon-induced hot-electron generation and transfer	24
1.4.1 Metal-semiconductor contact induced band bending	24
1.4.2 Mechanism of plasmon-induced hot-electron generation	26
1.4.3 Near-field enhancement	28
1.4.4 Application of plasmon-induced hot-electron generation	29
1.5 Strong coupling of plasmon and nanocavity modes.....	32
1.6 Outlook of this thesis	34
1.7 Reference	36
Chapter 2 Size effect on the Modal Strong Coupling Conditions	40
2.1 Introduction.....	40
2.2 Experimental section.....	41
2.2.1 Fabrication of Au-NPs/TiO ₂ /Au-film photoelectrodes.....	41
2.2.2 Characterizations.....	42
2.2.3 Photoelectrochemical measurement.....	42
2.3 Results and discussions	43
2.3.1 Dependence on the size of Au-NPs.....	43
2.3.2 Dependence on inlaid depth of Au-NPs	47
2.3.3 Charge separation under modal strong coupling condition	50
2.4 Conclusions.....	50
2.5 References	51
Chapter 3 Efficient Hot-Electron Transfer under Modal Strong Coupling Conditions with Sacrificial Electron Donors	52
3.1 Introduction.....	52
3.2 Experimental section.....	53
3.2.1 Fabrication of Au-NPs/TiO ₂ /Au-film photoelectrodes.....	53
3.2.2 Characterizations.....	53
3.2.3 Photoelectrochemical measurement.....	53
3.2.4 Transient absorption decay of Au nanodisks/TiO ₂	54
3.2.5 <i>In situ</i> spectroelectrochemical measurement.....	55

3.3 Results and discussions	57
3.3.1 Dependence on concentration of electron donors	57
3.3.2 <i>In situ</i> optical measurement of photoelectrodes	59
3.3.3 Plasmon-induced hot-electron transfer.....	65
3.3.4 Hot-electron transfer efficiency.....	67
3.4 Conclusions.....	68
3.5 References.....	69
Chapter 4 Near-Field Engineering for Boosting the Photoelectrochemical Activity to a Modal Strong Coupling Structure	70
4.1 Introduction.....	70
4.2 Experimental section.....	71
4.2.1 Fabrication of Au@Au-NPs/TiO ₂ /Au-film photoelectrodes	71
4.2.2 Characterizations.....	72
4.2.3 Numerical simulations	72
4.2.4 Photoelectrochemical measurement.....	73
4.3 Results and discussions	73
4.3.1 Finite element method (FEM) simulation	73
4.3.2 Constant potential electrolysis (CPE) process.....	76
4.3.3 Morphologies of the prepared photoelectrodes.....	78
4.3.4 Optical properties.....	83
4.3.5 Photoelectrochemical activity	85
4.4 Conclusions.....	89
4.5 References.....	89
Chapter 5 Conclusions and future perspectives	91
5.1 Conclusions.....	91
5.2 Future perspectives	92
Publications.....	93

Acknowledgements

I would like to express my sincere acknowledgments to all of those who helped me during my doctoral studies at Hokkaido University. The utmost appreciations go to my supervisor, Professor Hiroaki Misawa, for his patient guidance. I have continuously benefited from his tremendous knowledge and unique perspectives on researches. I would like to thank him for giving me such a precious opportunity to study in his lab which is a first-rate experimental platform. His insightful and encouraged advice inspired me and made my research and life go smoothly. He is an incomparable mentor for me. He has encouraged and inspired me to keep moving on the way to my Doctoral degree, even to be a scientist in the future. Without his patient supervision, advice and help, I could not have harvested so much for these years. Without his constant trust and patient guidance, this thesis could not have been completed smoothly.

I would also like to greatly thank to Prof. Tomoya Oshikiri for giving me numerous scientific advice and helping me revising my manuscripts with his precious time. His plentiful of insightful discussions and constructive comments as well as sophisticated writing skills has benefited me not only in my present research but in my future career. I would also like to express my special thanks to Prof. Xu Shi for his help in my entrance exam, my life in Hokkaido, and research work. He has taught me numerous scientific knowledge as well as experimental skills about my research and helped me a lot both in research and life here. He helped me revising my manuscripts even he was so busy and gave me plentiful of scientific advice. He is always kind and patient to me when I need help. It is my great pleasure to work with him.

I would like to give my special thanks to Ms. Yumiko Yamaguchi, who helped me a lot for documents preparation all the time with her great patience and carefulness. Without Ms. Yamaguchi's help, I could not enjoy my study and life in Hokkaido University. I would like to give my great thanks to Dr. Shuai Zu for his constructive advice on my experiments and manuscripts. I would also like to express my great thanks to our former members, Prof. Kosei Ueno, Dr. Quan Sun and Dr. Jie Li, who gave me

numerous help both in my research and life.

I would like to express my special appreciation to all the colleagues and graduates in the Prof. Misawa's Laboratory for their help and friendships. I would like to appreciate Ms. Xiaoqian Zang for her help in my life in Hokkaido and research work. Without her patient translation, I would never have enjoyed my study and life here. She took care of me so much. I would have never forgot the days when we worked and played together. I would also like to express my thanks to Mr. Yaguang Wang and Mr. En Cao for their help both in my research work and life in Hokkaido. I would also like to express my great thanks to other laboratory members, Mr. Keisuke Nakamura, Mr. Yen-En Liu, Ms. Azusa Onishi, Mr. Yoshiki Suganami, Mr. Kazuki Furuya, Ms. Xin Fan. They were all very kind and helped me a lot both in my experiments and life in Hokkaido. They are wonderful and generous colleagues and partners. It has been my great pleasure to work with them. I would also like to express my special appreciation to all of my friends who supported and inspired me to strive for my goal. All of them made my life more colorful and memorable.

I would also like to express my deep gratitude to the staff in Research Institute for Electronic Science. I really appreciate all the kindly support they have given me and wish them all the very best in the future.

I am indebted to the China Scholarship Council (CSC) for their generous funding, which removed financial concerns from my decision to embark on this journey.

Special thanks to my family: my husband, my parents and my brother. Words cannot express how grateful I am to my family for all of the sacrifices that they have made for me. Without their support, love, and encouragement, I could not have finished my research work and thesis. I dedicate this thesis to them.

Thesis Abstract

Improving the efficiency of converting the abundant solar energy to the chemical energy is one of the most significant strategies to address the current environmental and energy crisis. For example, the photocatalytic artificial photosynthesis such as water splitting under the irradiation of solar light provides us convenient approaches for energy production and environmental conservation. In recent decades, the concept of photocatalysis combined with localized surface plasmon resonances (LSPRs), which are the collective oscillation of charge carriers at the surfaces of metallic nanoparticles (NPs), has accelerated progress in boosting the photocatalytic activity in visible light and even infrared light. However, it is difficult to harvest visible light effectively with monolayer of metallic NPs. Recently, it was reported that a modal strong coupling between a Fabry-Pérot (FP) nanocavity mode and an LSPR showed a large and broad absorption by optical hybrid modes. In this thesis, essential properties of modal strong coupling between FP nanocavity mode and LSPR was investigated to improve the photoelectrochemical water oxidation under visible light irradiation. Au-NPs/TiO₂/Au-film (ATA) structure was employed to achieve the modal strong coupling.

At first, I investigated the particle size effect of Au-NPs on the photoelectrochemical properties under the modal strong coupling condition. The ATA structure was produced based on the technology of sputtering, atomic layer deposition (ALD), thermal evaporation, and annealing, respectively. Au-NPs with various particle sizes were employed for the TiO₂ surface decoration and providing the LSPR mode, which could couple with the FP-nanocavity mode of TiO₂/Au film. The experimental results illustrated that Au-NPs with a size around 12 nm showed superior properties not only in photoelectrochemical performance but economically friendly. The absorption spectrum of ATA structure exhibited distinct dual bands at wavelength longer than 550 nm when Au-NPs were partially inlaid in TiO₂. The photoelectrochemical measurement showed that the ATA structure exhibited obvious photocurrent enhancement. (Chapter 2).

Then, I investigated the hot-electron transfer efficiency on a photoanode under the modal strong coupling conditions by monitoring the photoelectrochemical activities, including IPCE and internal quantum efficiency (IQE) using triethanolamine (TEOA) as an efficient electron donor to sufficiently accelerate the surface reaction. In the presence of TEOA, the IPCEs of the lower branches of hybrid modes formed by the strong coupling were improved as much as 4.0 times, whereas these for upper branches were up to 4.5 time. Furthermore, in the wavelength range 500-800 nm, it the average IQE was calculated to 3%. In addition, the Fermi level changes due to the generation and consumption of hot-carriers in the ATA structure also discussed by performing in situ spectroelectrochemical measurements (Chapter 3).

In the ATA structure, however, Au-NPs are partially inlaid inside TiO_2 to increase the interaction between the nanocavity and LSPR. The intensified near-field is generated at the bottom of Au-NPs rather than the surface of TiO_2 according to the simulation results. This fact indicates that hot electron and hole pairs are produced and separated at the inlaid interface of Au-NPs/ TiO_2 inside TiO_2 . For the photoelectrochemical reactions, the holes must transfer to the surface of TiO_2 to participate the oxidation reaction. This migration process of holes has an adverse effect on the photoelectrochemical reactions by inducing the recombination. Therefore, the hot-spot of the near-field should be near the reaction surface for the efficient water oxidation. In order to tailor the near-field distribution, a postdeposited Au on ATA structure was implemented using a facile constant potential electrolysis technique to postdeposit Au on ATA photoelectrode (Au@ATA). In Au@ATA structure, a strong near-field is induced at the interface of postdeposited Au and TiO_2 , where the water oxidation reaction occurs effectively. Consequently, the average IPCE of Au@ATA is approximately 1.3-fold higher than that of ATA. Both simulated and experimental results showed that the interface established in postdeposited Au and TiO_2 was significant in improving photoelectrochemical performance (Chapter 4).

In summary, photoelectrochemical properties on the modal strong coupling structure between FP-nanocavity and LSPR under visible light irradiation were

investigated using the ATA structure to achieve the efficient water oxidation. The structure of ATA was optimized by varying the size and inlaid depth of Au-NPs. The photoelectrochemical study with the sacrificial electron donor revealed that the hot-electron injection efficiencies of the photoanode under modal strong coupling condition are significantly larger than that of the conventional plasmonic anode. Furthermore, it was found that the near-field enhancement near the interface of the three-phase boundary between the interface of Au-NPs, TiO₂ and aqueous solution was significant in water oxidation on the ATA. Additionally, the enhanced near-field distribution of Au nanostructures can be engineered by simply adjusting their shape and size. It provides the possibility for constructing low-costing artificial photosynthesis systems. These results guarantee the future researches to investigate the mechanism of hot-carrier-induced photoelectrochemical properties.

Keywords: localized surface plasmon resonance, Fabry-Pérot nanocavity, modal strong coupling, near-field enhancement, photoelectrochemistry, water oxidation

Chapter 1 Introduction

1.1 Background and motivation

In 1972, A. Fujishima and K. Honda discovered that water could be photoelectrochemically split into oxygen (O_2) on a Titanium dioxide (TiO_2) photoelectrode under UV light irradiation and H_2 on a platinum dark electrode. Since then, tremendous researches on photocatalysis and photoelectrochemical cells were triggered.¹ Although TiO_2 is considered as the most widely employed “golden” photocatalyst among the various photocatalysts owing to its various advantages including stable, nontoxic, low-cost, it cannot absorb light in visible region because of the large bandgap.²⁻⁴ Plasmon-enhanced photoresponses of TiO_2 in visible and/or near infrared region is considered as promising method in improving the photocatalytic performance.^{5,6} The utilization of noble metal nanoparticles brings out numerous benefits to photocatalysis (Figure 1.1).⁶ Noble Metallic nanoparticles with LSPR have attracted mushrooming interest with a wide range of research topics, including photovoltaic devices,^{7,8} surface-enhanced Raman scattering (SERS),⁹ solar cells,^{10,11} photoelectric catalysis systems.^{12,13} Notwithstanding plentiful number of researches have focused on photoelectrochemical performance with Au-NPs/ TiO_2 systems, it is still significant to study the photoelectrochemical performance that hinge on the interfacial structure of Au-NPs/ TiO_2 . The interfacial configuration between Au-NPs and TiO_2 is significant in the electron transfer process and it is easy to be predicted and design. Therefore, it is convenient to design plasmon-enhanced energy conversion systems in low-cost, high-efficient, ecofriendly, and lightweight.

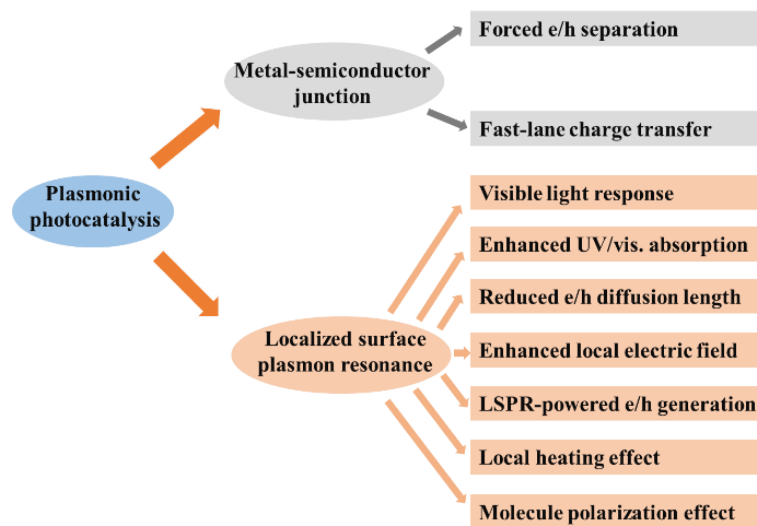


Figure 1.1 Major benefits of plasmonic photocatalysis.

1.2 Surface plasmon resonance

Plasmonic is a widespread and ongoing research area on nanomaterials. Noble metal nanostructures exhibit characteristic optical performances. These properties can be used to control and route light in nanometer scales. Plasmonic relates to the basics and applications of surface plasmon resonance (SPR). SPR is established on the interaction between conduction electrons in noble metal and electromagnetic radiation. This phenomenon can result in both localized optical far-field and near-field scattering. The utilization of optical properties generated by noble metallic nanoparticles can be traced back to ancient time. The Lycurgus Cup is a famous production based on plasmonic. When the Cup is irradiated from the front or the back, it displays different colors because of the SPR in glass-embedded gold nanoparticles, as shown in Figure 1.2.¹⁴



Figure 1.2 The Lycurgus Cup before (left) and after (right) irradiation.¹⁴

1.2.1 SPR in noble metal nanostructures

(1) Dielectric function of metals¹⁵⁻¹⁸

Drude model is deemed to the first approximation to depict metal dielectric function. In this model, only free electrons in metals are taken into account. When an electromagnetic wave with the frequency of ω irradiates on the metal, the free electrons are forced to oscillate. So, the metal dielectric function is shown as following,

$$\varepsilon_m(\omega) = 1 - \frac{\omega_p^2}{\omega^2 + i\omega\gamma} \quad (1.1)$$

where the frequency of bulk plasma is ω_p . The constant of bulk damping is γ . γ is determined by the electrons' mean free path l and Fermi velocity v_F , in which $\gamma = \frac{v_F}{l}$.

Also, ω_p can be described as $\omega_p = \sqrt{\frac{ne^2}{\varepsilon_0 m_e}}$, in which the free electrons' density is n , the electric charge is e , the vacuum permittivity is ε_0 , and the electrons' effective mass is m_e .

Several processes can result in the damping of electron oscillation: electron and phonon collisions, electron and ion collisions, and electron and electron collisions.

The complex dielectric function is described as $\varepsilon_m(\omega) = \varepsilon_1(\omega) + i\varepsilon_2(\omega)$, in which $\varepsilon_1(\omega)$ is the real part and $i\varepsilon_2(\omega)$ is the imaginary one. They are defined by the following equations,

$$\varepsilon_1(\omega) = 1 - \frac{\omega_p^2 \tau^2}{1 + \omega^2 \tau^2} \quad (1.2)$$

$$\varepsilon_2(\omega) = \frac{\omega_p^2 \tau}{\omega(1 + \omega^2 \tau^2)} \quad (1.3)$$

where $\gamma = 1/\tau$. τ is the free electrons' relaxation time. At room temperature, τ is typically on the order of 10^{-14} s, thereby γ is 100 THz.

According to the reports,^{16,19} $\omega \gg \gamma$, simple approximate expression of the dielectric function is obtained. Under this simple condition, the dielectric function is determined by the real part and shown as following,

$$\varepsilon_m(\omega) = 1 - \frac{\omega_p^2}{\omega^2} \quad (1.4)$$

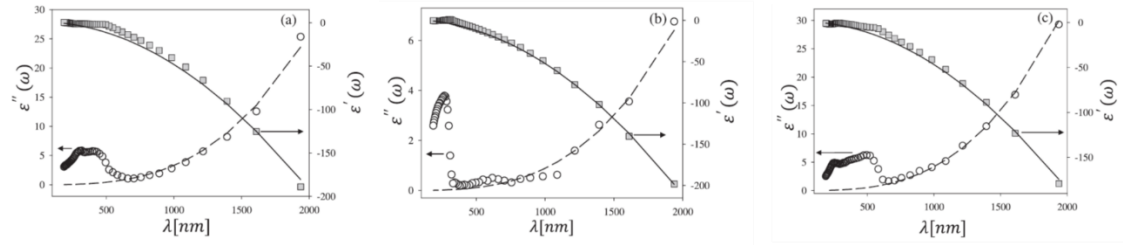


Figure. 1.3 Real (solid line) and imaginary (dashed line) parts of free-electron contribution for (a) gold, (b) silver and (c) copper obtained by Eq. (1.1). Grey squares are the real parts of experimental bulk dielectric function, and hollow circles are the imaginary ones.¹⁷

Based on the Drude model experimental results, the real part and imaginary part of the dielectric functions for Au, Ag, Cu are summarized in Figure 1.3.¹⁶ For Au, when $\lambda \geq 750$ nm, the curves plotted by the Drude model could well fitted to those of experimental data. Moreover, Ag is $\lambda \geq 300$ nm and Cu is $\lambda \geq 700$ nm. The interband transition onsets of Au, Ag and Cu are 2.3 eV, 3.7 eV, and 2.1 eV, respectively, which are approximately in accordance with the aforementioned results.²⁰ Obviously, the curves cannot fit well at shorter wavelength for these metals. The reason is that interband transition can lead to increment of the dielectric function's imaginary part. Therefore, the Drude model can approximately provide an illustration of the dielectric functions for Au, Ag, Cu at visible even near-infrared region. In this wavelength region,

the free electrons of the metal mainly devote to the function.

(2) SPR

The freely conducted electrons at the noble metal surface can travel through the material untrammelled. These electrons can be excited as well as compel to oscillate relative to the metal atoms under the illumination from visible to near-infrared light. This phenomenon is defined as plasma oscillation. Under illumination, the free electrons can oscillate collectively. These electrons are in resonance with the oscillated electric field of incident light. Therefore, SPR appears. The energetic plasmonic electrons are generated via the non-radiative excitation of SPR. SPR is a promising optical technology with numerous applications, *e.g.* sensing,²¹ surface enhanced Raman scattering (SERS),^{22,23} molecule detection,^{24,25} solar cells,^{26,27} photocatalysis,²⁸ and so on. SPR can be classified into surface plasmon polariton (SPP) and localized surface plasmon resonance (LSPR).

SPP, also known as propagating surface plasmon resonance (PSPR), is the excitation of the coupled state between plasma oscillations and photons at the interface of metals and dielectric materials. SPP provides a promising research way in fields including energy, environment, medicine, and biology. The major applications of SPP, are waveguides,^{29,30} near-field optics,³¹ SERS,³² data storage,³³ solar cells,³⁴ chemical sensors and biosensors.^{35,36} Along the x direction, as displayed in Figure 1.4a, the electromagnetic wave can propagate as an evanescent wave at the metal surface. SPP is described by the dispersion relation as follows:

$$k_{SPP} = k \sqrt{\frac{\varepsilon_d \varepsilon_m}{\varepsilon_d + \varepsilon_m}} \quad (1.4)$$

where the wave vector of SPP is k_{SPP} . The wave vector of incident light is $k = \omega/c$. dielectric constant of the surrounding environment (dielectric) is ε_d . The metal's dielectric constant is ε_m .

When $\varepsilon_d + \varepsilon_m = 0$, the surface charges can oscillate collectively, thereby exciting SPP. The frequency of many metals is in the UV light region, while the metal is no longer metallic beyond the frequency. As a result, the SPP frequency is given as

following:

$$\omega_{SPP} = \frac{\omega_P}{\sqrt{1+\epsilon_d}} \quad (1.5)$$

Therefore, the frequency of bulk plasma is higher than that of the resonance.³⁷ Typically, owing to the mismatch of wavevector between SPP and irradiation light, SPP could not be excited directly on the metal surface by light irradiation. Nevertheless, prism or grating can be used as coupling medium to couple the light into SPP.³⁸⁻⁴⁰

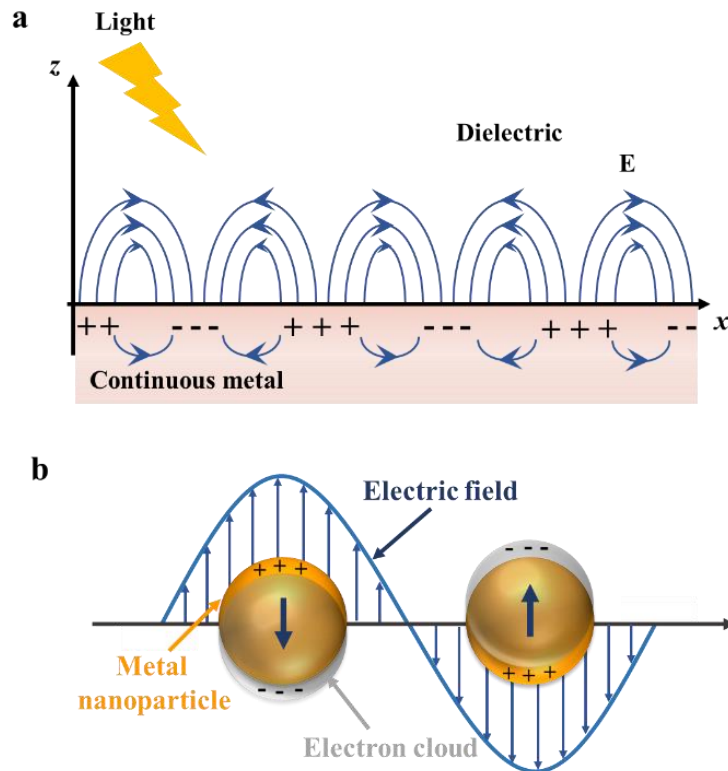


Figure 1.4 Schematics of (a) SPP and (b)LSPR.

When the surface of metallic nanostructures (such as nanoparticles, nanorods, nanostars, etc.) is rough or with small bumps, surface plasmons will be mainly localized inside the metallic nanostructure and around the interface. Therefore, LSPR is defined as a non-propagating excitation of SPR at the surface of noble metal structures. The oscillation of charge in spherical metallic nanoparticle is distinct with that in continuous metal.¹⁵ LSPR can be excited directly by incident light.

As displayed in Figure 1.4b, when incident light irradiates on metallic nanoparticles, free electrons of metallic nanoparticles are excited and then oscillate collectively at the

particles' surface. When the electron cloud at the particle's surface displaces relative to the metal nuclei, the displaced electron cloud will restore to the nuclei owing to the Coulomb interactions between the electron cloud and nuclei. This collective oscillation behavior of electron cloud relative to the nanoparticle is defined as LSPR. LSPR is generated when the oscillation frequency of free electrons is same as the incident photon's frequency.⁴¹⁻⁴³ Four factors can determine the oscillation frequency: the density of electrons, the shape of the charge distribution, the size of the charge distribution, the effective electron mass. Therefore, the incident light energy can be effectively converted into the kinetic energy of the free electrons' collective oscillation.⁴¹

When the wavelength of the irradiation light is much larger than the nanoparticle's size, a quasistatic approximation can be employed to the metallic nanoparticle. The polarizability of the nanoparticle is described as,

$$\alpha = 4\pi R^3 \frac{\varepsilon_m(\omega) - \varepsilon_d}{\varepsilon_m(\omega) + 2\varepsilon_d} \quad (1.6)$$

where the nanoparticle's radius is R . Evidently, a maximum polarizability will be achieved with a minimum $|\varepsilon_m(\omega) + 2\varepsilon_d|$, resulting in the LSPR. For metal, thus, the resonant condition without considering damping of electron oscillation as well as following Drude model is as following,

$$\varepsilon'(\omega) = -2\varepsilon_d \quad (1.7)$$

Therefore, for Eq. 1.7, it can be further expressed as following by applying Eq. 1.4,

$$\omega_{LSPR} = \frac{\omega_p}{\sqrt{1+2\varepsilon_d}} \quad (1.8)$$

Thus, LSPR's resonance frequency is also directly determined by the dielectric environment. When the metallic nanosphere is in air ($\varepsilon_d = 1$), ω_{LSPR} is $\frac{\omega_p}{\sqrt{3}}$.

On the other hand, in 1908, an analytical solution to Maxwell's equations was originally developed by Gustav Mie. It can describe the extinction spectra (extinction = scattering + absorption) of metallic nanospheres in arbitrary size.^{41, 44} Up to now, Mie theory is the merely simple and precise solution to Maxwell's equations that is related to metal nanoparticles.

$$C_{Ext} = C_{Sca} + C_{Abs} \quad (1.9)$$

where the extinction cross section is C_{Ext} . The scattering cross section is C_{Sca} . The absorption cross section is C_{Abs} .

Under a quasistatic approximation, the extinction cross section can be expressed as following,

$$C_{Ext} = \frac{24\pi^2 R^3 \sqrt{\epsilon_d^2}}{\lambda} \left[\frac{\epsilon_2}{(\epsilon_1 + 2\epsilon_d)^2 + \epsilon_2^2} \right] \quad (1.10)$$

Because the polarization α is resonantly enhanced, the metallic nanoparticle can scatter and absorb light effectively. The corresponded C_{Sca} and C_{Abs} are given by,

$$C_{Sca} = \frac{k^4}{6\pi} |\alpha|^2 \quad (1.11)$$

$$C_{Abs} = kIm[\alpha] \quad (1.12)$$

Where $Im[\alpha]$ is the imaginary part of α .

According to Drude-Lorentz Model,⁴⁵ the resonance frequency of LSPR is satisfied when $\epsilon_1 + 2\epsilon_d = 0$. Under the condition of resonance frequency of LSPR, the polarizability of metallic nanoparticles (α), C_{Ext} , C_{Sca} and C_{Abs} will reach the corresponding maximum values. For example, peak appears in the extinction spectrum.

The above approximation can be only applied to metallic nanospheres with any size. Furthermore, for metal nanoparticles in other shape, it only needs to introduce a shape factor in order to employ the similar approximation.^{46,47}

1.2.2 Characteristics of LSPR

Ascribing to the unique properties and extensive applications, LSPR has achieved considerable recent interest. The extinction cross section is extremely high of the plasmonic nanostructures. Also, the structures can concentrate incident light in a nanoscale region near to their surface. In other words, LSPR can determine the absorption spectra of metallic nanoparticles. Moreover, the properties of LSPR (such as absorption band) for metallic nanostructures depend on the shape, size and nanoparticles' composition, and the nanoparticles' surrounding.

(1) Large extinction cross section

Extinction cross section is one of the key physical properties of plasmonic nanostructures exploited in many applications, including photovoltaics and biosensing. The sum of the scattering cross section and absorption cross section can determine the value of extinction cross section (Eq. 1.9). The interaction strength of a plasmonic nanostructure with electromagnetic radiation is quantified by its extinction cross section, which means that stronger interaction probability ascribes to a larger extinction cross-section.⁴⁸

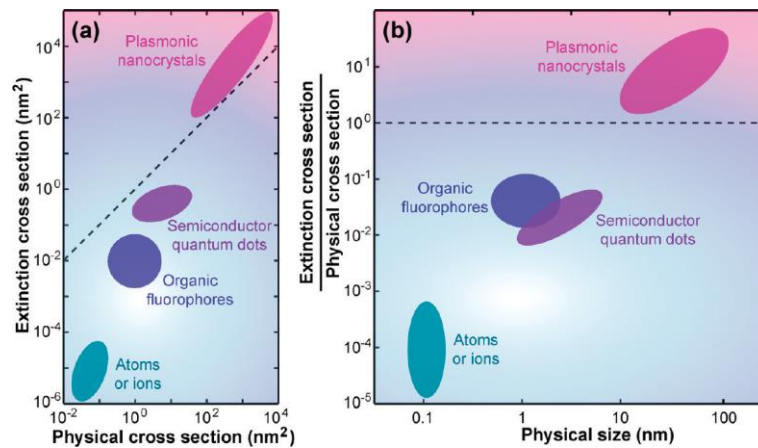


Figure 1.5 Comparison of extinction cross sections of various optical species. (a) Plot of the extinction cross section versus the physical cross section. (b) Plot of the ratio between the extinction and physical cross sections versus the physical size of optical species.⁴⁹

Four most common forms of nano scaled optical species were summarized by Ming et al.⁴⁹ The forms are plasmonic nanocrystals, atoms/ions, semiconductor quantum dots, and organic fluorophores (Figure 1.5). When the optical species' orthographic projection normal to the plane of the incident light, their physical cross section can be determined. As illustrated in Figure 1.5, with enlarging the size, cross sections for absorption and scattering of the optical species increase. Whereas, the cross section for scattering increase more rapidly than that of the absorption. Compared to their own physical cross sections, plasmonic nanocrystals is the only optical species that exhibit larger extinction cross section.

(2) Near-field enhancement

Near-field enhancement is another prominent property associated with plasmonic nanostructures. Localized electric fields can be generated around the metallic nanoparticles due to LSPR. According to Eq. 1.6, the strength of the localized electric fields is in orders of magnitude which is much higher than that of the incident field.⁵⁰

The electric field distributions obtained from finite-difference time-domain (FDTD) simulation with different shape of Au-NPs is summarized in Figure 1.7.⁵¹ From left to right is Au nanosphere, Au nanorod, and Au nanoplate. $|E|^2/|E_0|^2$ denotes the enhancement factor of the near-field. The intensity of the electric field around the Au-NPs is E . The intensity of the incident light is E_0 . Au-NPs' curvature can determine the intensity of the near-field.^{52,53} Its near-field becomes more intensified when the metallic nanostructure is sharper. Therefore, as illustrated in Figure 1.6, the near-field intensity of Au nanosphere is much lower than that of Au nanoplate and Au nanorod. Because of the factor of near-field enhancement at the tips is much higher than that of Au nanorod, Au bipyramid is considered as a prime structure.⁵³

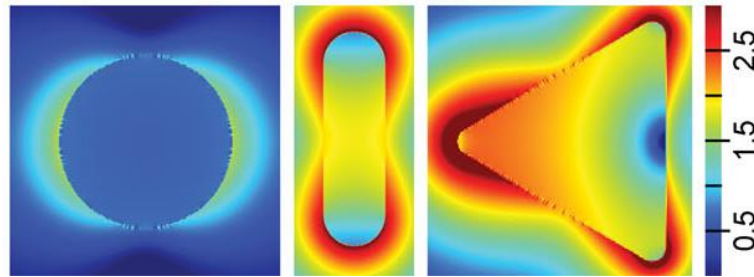


Figure 1.6 FDTD simulated electric field distribution for Au-NPs in different shape.⁵¹

The strong near-field of plasmonic nanoparticles provides a basic mechanism for diverse applications, such as SERS,⁵⁴⁻⁵⁶ photoelectrochemistry,⁵⁷, etc.

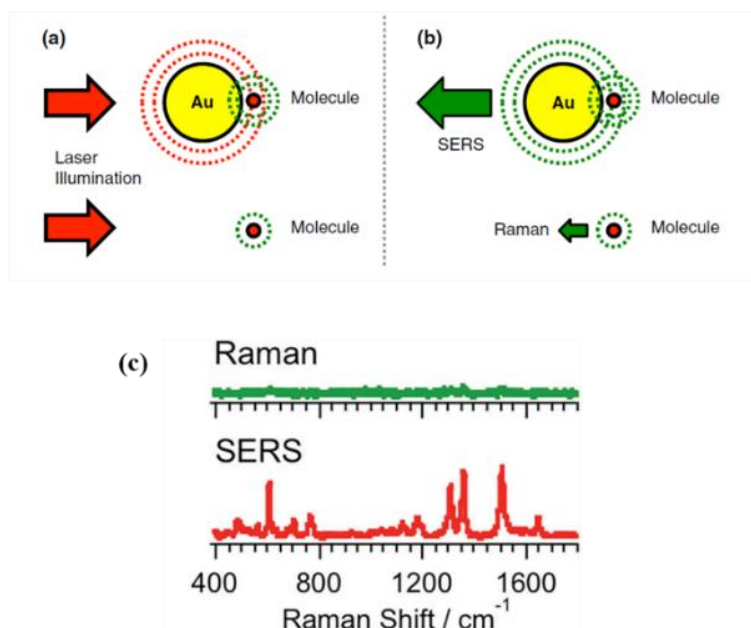


Figure 1.7 Basic SERS electromagnetic mechanism.^{55,56}

Raman scattering is the inelastic light scattering of molecules' vibrational excitation. This process is extremely inefficient. As shown in Figure 1.7, when the molecules are near or in contact with the plasmonic nanoparticles' surface, the Raman intensity can be significantly enhanced.^{55,56} It is partly due to the strong near-field promotes the molecules' excitation.⁵⁵

Plasmonic nanoparticles can improve the photoelectrochemical activities such as photocurrent generation of photoelectrodes by increasing the visible light absorption. As illustrated in Figure 1.8, a conspicuous increment about 66 times in photocurrent is observed for Au-NPs and the photocurrent is $0.3 \mu\text{A}$.⁵⁷ It has been intensively utilized in different types of solar cells, for example, dye-sensitized solar cells,⁵⁸⁻⁶⁰ organic solar cells,⁶¹ perovskite solar cells.⁶² It can improve the photocurrents and thereby enhance the power conversion efficiency (PCE).

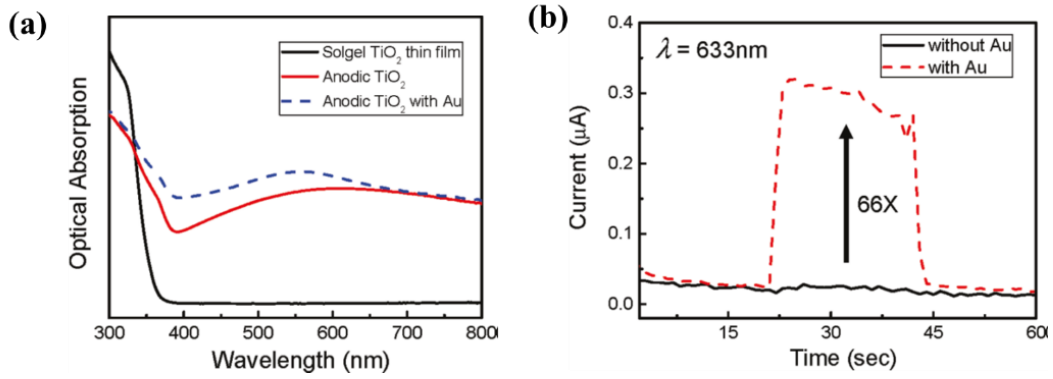


Figure 1.8 (a) Absorption spectra and (b) Photocurrent with $\lambda = 633$ nm light for 22 s of TiO₂ with and without Au-NPs.⁵⁷

(3) Tailorable absorption spectra

The absorption band of LSPR can be regulated by changing the size, shape, and chemical composition of the nanoparticles. The size of metallic nanoparticles has significant effects in scattering and absorption cross sections. As shown in Figure 1.9, when the size of Au-NP is enlarged from 20 nm to 80 nm, the LSPR's resonant wavelength shifts from 520 nm to 540 nm.⁶³

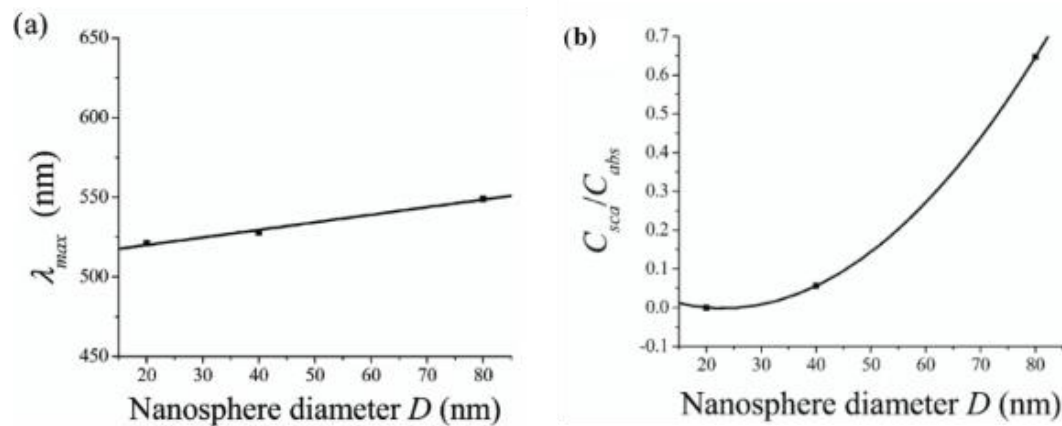


Figure 1.9 (a) Calculated resonant wavelength and (b) the calculated ratio C_{Sca}/C_{Abs} with various size of the Au-NP.⁶³

Moreover, the spectrum's peak position, shape and full width at half maximum (FWHM) is immensely related to the aspect ratio and configuration of nanostructures. As shown in Figure 1.10, the aspect ratio of Au nanorods can affect the resonant

wavelength. This wavelength can be tuned from visible light to near infrared light.⁶⁴

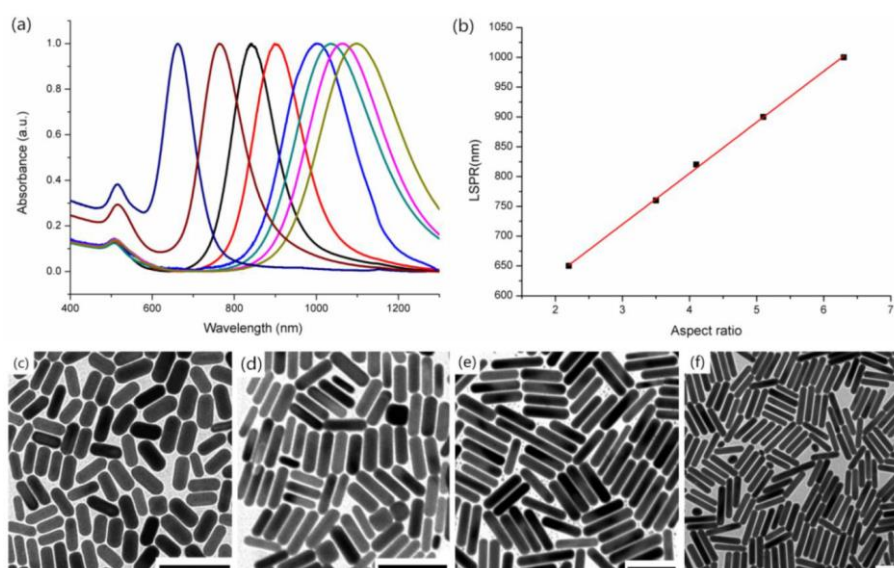


Figure 1.10 (a) Absorption spectra of Au nanorods with the longitudinal LSPR peaks (b) The relationship between the longitudinal LSPR peaks and calculated aspect ratios. (c-f) Representative TEM images of Au nanorods with the longitudinal LSPR peaks at (c) 650 nm, (d) 760 nm, (e) 920 nm, and (f) 1000 nm.⁶⁴

1.2.3 Relaxation Processes of LSPR

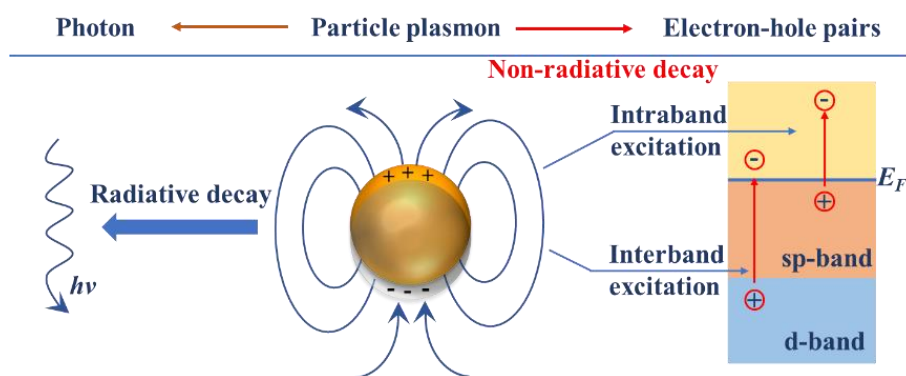


Figure 1.11 Schematic decay of LSPR.

LSPR has certain lifetime and it finally decays in two ways:⁶⁵ the radiative decay and the non-radiative decay (Figure 1.11). When the particle plasmons transform into photons, radiative decay takes place. It is the far-field light scattering and a thorough loss in LSPR. However, the non-radiative decay takes place via producing electron-

hole pairs. There are two categories for the non-radiative decay. One is the intraband excitation, which occurs within the conduction band. The other is the interband excitation, which is the transitions between d-bands of noble metals and conduction band.⁶⁵

1.2.4 Applications of LSPR

LSPR has been intensively investigated in various research areas owing to its unique and adjustable optical properties by manipulating the size, shape, as well as the chemical composition of the metal nanostructures. Till now, LSPRs have already been extensively utilized in the areas such as SERS,⁵⁴⁻⁵⁶ chemical and biological sensors,⁶⁶ photoelectric conversion systems,⁶⁷ photocatalysis,⁶ and so on. Herein, the applications in SERS, photovoltaics, and photocatalysis which are related to the studies in our laboratory are listed here. In addition, plasmonic photocatalysis will be discussed in the following section.

(1) SERS

Upon LSPR excitation, the plasmonic strong near-field is present at the metallic nanostructures' surface. The induced dipole in the molecule can be excited mutually with the induced dipole in the metal nanostructure. Thus, compared to free molecules, the field of the molecule-nanostructure group can be improved by 1~3 orders of magnitude. The SERS intensity is highly determined by incident (incoming) as well as scattered (outgoing) fields. When the incident and scattered fields resonant to the LSPR of metal nanostructures, SERS enhancement is brought about. SERS has already achieved tremendous research interest since its discovery in 1973. Owing to the non-destructive and ultra-high sensitivity, SERS is considered as an efficient analysis technology for identification, quantification and ultrasensitive detection of various molecules.⁶⁸

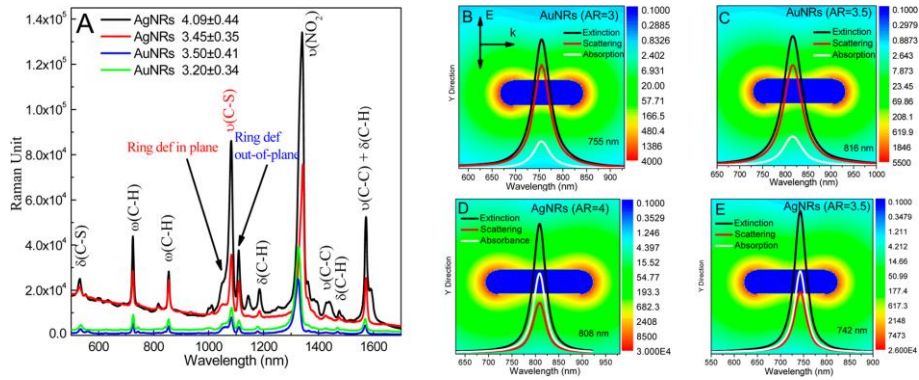


Figure 1.12 SERS of 4-nitrothiophenol on the surface of Au nanorods and Ag nanorods in different aspect ratios.⁶⁹

As shown in Figure 1.12,⁶⁹ the increment in Raman signal by Ag nanorods is more obvious than that of Au nanorods because of the higher the plasmon field intensity of Ag nanorods. The Rayleigh scattering of Au nanorods is stronger than that of Ag nanorods. Therefore, Au nanorods are recommended for optical plasmon imaging, while Ag nanorods are more efficient in plasmon sensing.⁶⁹

(2) Photovoltaics

LSPRs can be utilized to boost the overall power conversion efficiency, photocurrent generation ability, and absorption property in various types of photovoltaic devices, such as silicon solar cells,⁷⁰ dye-sensitized solar cells (DSSC),⁷¹ organic solar cells,⁷² and perovskite solar cells.⁷³

With the integration of unique metal nanogratings, Wei Wang et al.⁷⁰ realized the solar cell equipped with enhanced light absorption and polarization-insensitivity (Figure 1.13).

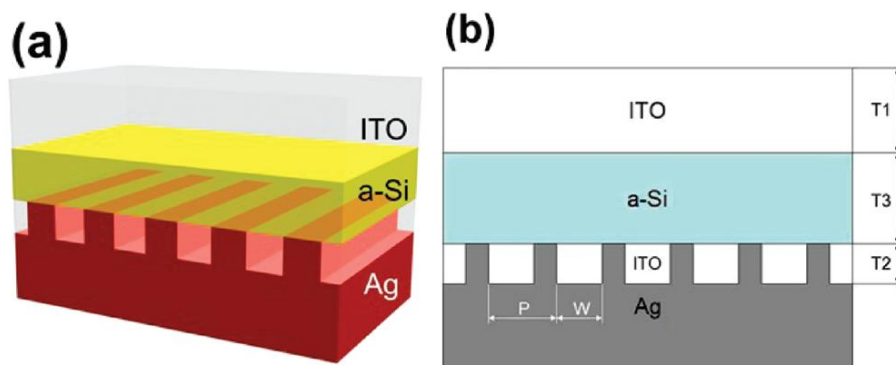


Figure 1.13 Schematics of the proposed solar cell structure.⁷⁰

Recently, Da-Wei Zhao et al.⁷³ reported a facile preparation method at low temperatures to embed Au-NPs in TiO₂ film. This structure could enhance both the stability and efficiency of n-i-p planar heterojunction perovskite solar cells (Figure 1.14).

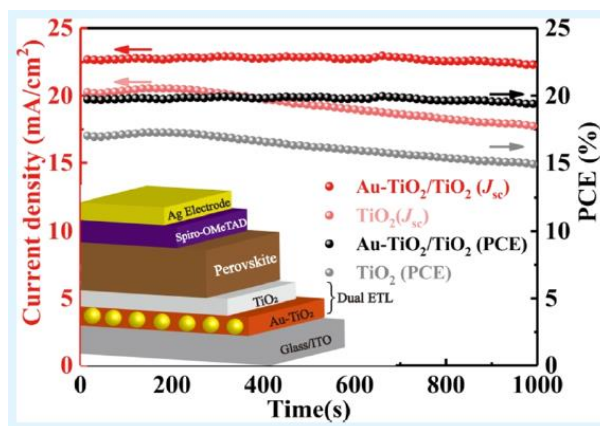


Figure 1.14 The proposed configuration of perovskite solar cell.⁷³

1.3 Fabrication of plasmonic nanostructures

Generally, it is much more convenient and easier to produce plasmonic nanostructures and their composite routinely under the rapid development of sophisticated chemical and lithographic methods. There are mainly two fabrication approaches of metal nanostructures, “top-down” and “bottom-up.” The “top-down” method is established based on sophisticated microfabrication. It has been developed over decades in semiconductor industry.⁷⁴ For, example, electron beam lithography (EBL) is considered as the prevailing technology in the top-down production of metallic nanostructures. However, the bottom-up method is based on the growth and self-assembly technologies. These technologies are originally developed in chemistry and biology.

1.3.1 Electron beam lithography

Figure 1.15 shows the procedure in fabricating periodic metal nanostructures by

EBL. First, electron-beam resist is spin-coated onto the substrate. Then the substrate is exposed to the electron beam. Then a metal layer is evaporated or sputtered on the substrate. After lift-off, the structures are obtained.

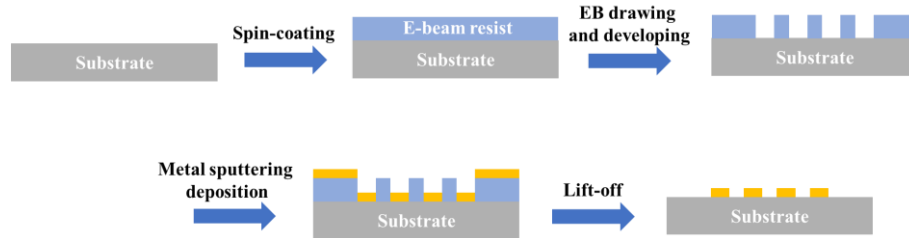


Figure 1.15 Preparation schematic for periodic metal nanostructures by EBL.

EBL provides an approach to fabricate relatively large numbers of metallic nanostructures in different shape and periodic layout. There are two major advantages for EBL.^{5,75,76} One is precisely control substrate's area, and the other is the low defect densities for the metallic nanostructures. However, the main disadvantages of EBL are costly and low output. Additionally, it is relatively challenging to utilize EBL to fabricate nanostructures smaller than 10 nm. Therefore, it is hard to fabricate structures with small interparticle spacings and sharp corners, which are attractive in metal nanostructure plasmonics.⁷⁴

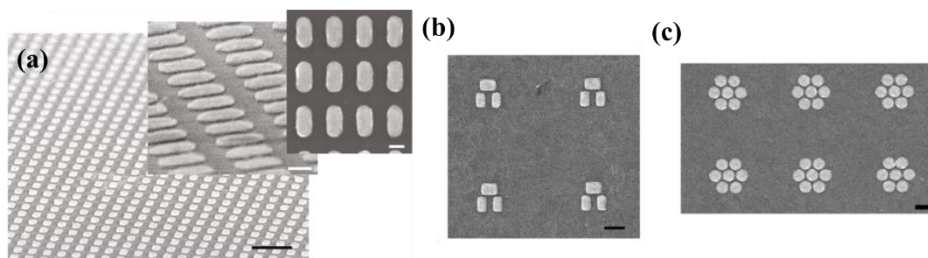


Figure 1.16 SEM images of various periodic shapes and arrangement fabricated by EBL.^{5,75,76}

1.3.2 Chemical growth method

In general, the bottom-up fabrication approaches can produce structures in precisely controlled configurations (including geometry and symmetry), and functionalities. Therefore, it is necessary to fabricate metal nanostructures with narrow size and shape

distributions to control the plasmonic properties (including absorption peak and shape) of nanostructures. The metal nanocrystals can work as meta-atoms to trigger the bottom-up process of plasmonic nanostructures.⁷⁷ As the structural features including size, shape, exposed facets, edges, vertices, and surface roughness are critical to the properties plasmonic nanostructures, it is crucial to fabricate such nanostructures with devisable and repeatable properties.

Up to now, numerous chemical growth strategies, such as photocatalytic reduction, electrochemical reduction, and chemical reduction have been exploited to fabricate plasmonic metallic nanostructures.^{74,77,78} As summarized in Figure 1.17, the shape of the obtained metal nanoparticles include nanospheres,⁷⁹ nanorods,⁸⁰ nanoplates,⁸¹ nanocubes,⁸² nanoshells, to name a few.

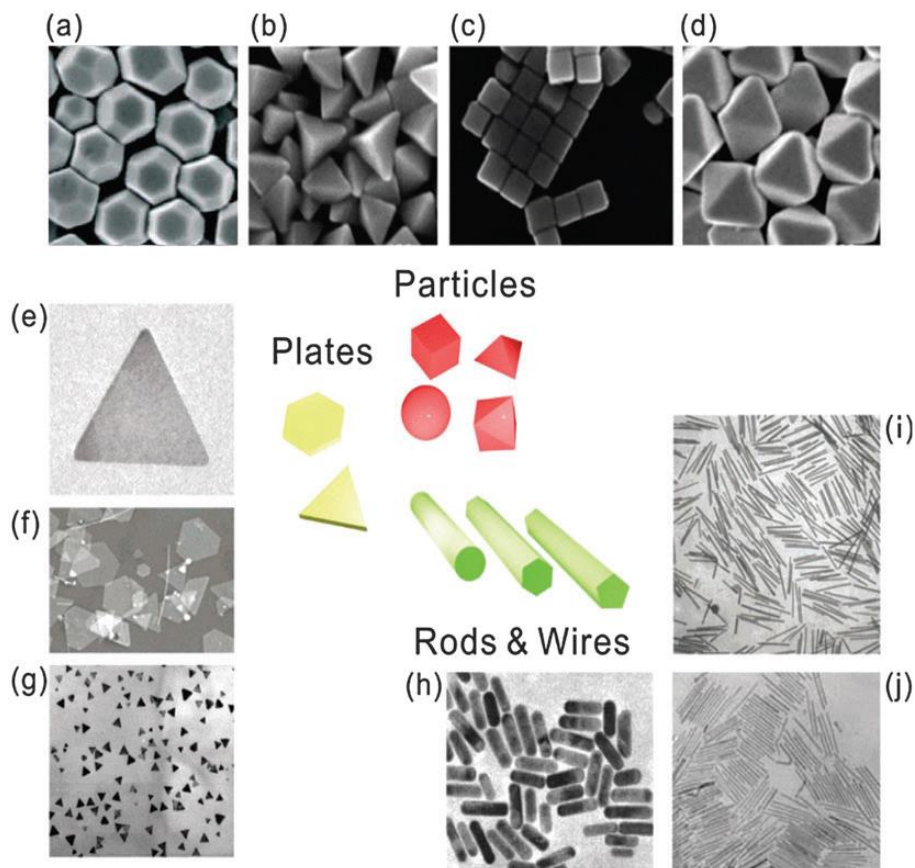


Figure 1.17 Examples of Au and Ag nanocrystal with various geometries prepared with different chemical growth methods.^{77, 82-90}

1.3.3 Other methods

Except for the above discussed two main fabrication methods, there are other approaches to fabricate plasmonic metal nanostructures with well-designed size and shape distribution. For example, focused-ion-beam (FIB) etching is considered as an alternative top-down method.⁹¹ In addition, the use of thermal or electron beam evaporation of metals on the substrate produce plasmonic nanoparticles with high dispersity. A discontinuous thin metal film is evaporated onto the substrate. Then the obtained structure is annealed in air or N₂ (depends on the metal) for some time at a given degree.^{92,93} It is considered as a high throughput and inexpensive fabrication method to produce metallic nanoparticles in high dispersity. However, the arrangement, orientation, and size of the nanoparticles cannot be well controlled.

1.4 Plasmon-induced hot-electron generation and transfer

Since the proposition of plasmon-induced electron-hole pairs generation and transfer mechanism in Au-NPs/TiO₂ systems by Tatsuma's group,^{94,95} plasmon-induced hot-electron generation and transfer from metal to semiconductor become a promising example in solar-to-energy conversion.

1.4.1 Metal-semiconductor contact induced band bending⁹⁶

When the semiconductor contacts with the metal, free electrons will transfer between them because of the work function (W) differentiation and cause band bending, which is firstly developed by Schottky and Mott. W is one of the crucial parameters in determining the electronic structure of metal and semiconductor. The relationship between W and Fermi level (E_F) is described as

$$W = E_{vac} - E_F \quad (1.13)$$

where E_{vac} is the vacuum energy.

Figure 1.18 is the energy band diagrams of n-type semiconductor and metal. Under the circumstance of the metal and semiconductor are contacted and the work function

of the metal (W_m) is higher than that of the semiconductor ($W_m > W_s$), electron flowing will occur from the semiconductor to the metal till their Fermi levels are matching. Under equilibrium of the electron transfer, electrostatic induction will result in negatively charged metal surface region as well as positively charged semiconductor. Consequently, the interfacial built-in electric field between semiconductor and metal is formed. However, the concentration of free charge carriers in the semiconductor is very low. Thus, it is difficult for the semiconductor to effectively screen the interfacial electric field between metal and semiconductor. And therefore, compared to the bulk, the concentration of free charge carriers close to the semiconductor surface is depleted. This region is called the space charge region. Band bending will occur in this region on account of the continuously shifted energy band edges in the semiconductor caused by interfacial electric field. In the n-type semiconductor (electrons work as majority charge carriers), when $W_m > W_s$, electron depletion occurs in the space charge region and thereby is defined as depletion layer. The feature of this depletion layer is of excessive positive charge. In this layer, because of the built-in electric field, the energy bands bend upward toward the interface. The band bending energy (E_{BB}) is given by

$$E_{BB} = W_m - W_s \quad (1.14)$$

In addition, when $W_m > W_s$ the n-type semiconductor, at the interface between metal and semiconductor, an energy barrier is formed, and it is called Schottky barrier (E_{SB}). E_{SB} can be determined by

$$E_{SB} = W_m - \chi_s \quad (1.15)$$

where χ_s is the semiconductor's electron affinity.

When $W_m < W_s$, the right part of Figure 1.18, the electron flow from metal to semiconductor will take place until their Fermi levels become equal. Under this circumstance, the electrons will gather at the space charge region. This region is defined as the accumulation layer. In the accumulation layer, the energy bands bend downward toward the interface between metal and semiconductor interface. Also, there is no energy barrier.

Generally, when the semiconductor's Fermi level is upper than that of the metal, it will decrease because the charge transfers to the metal. Vice versa.

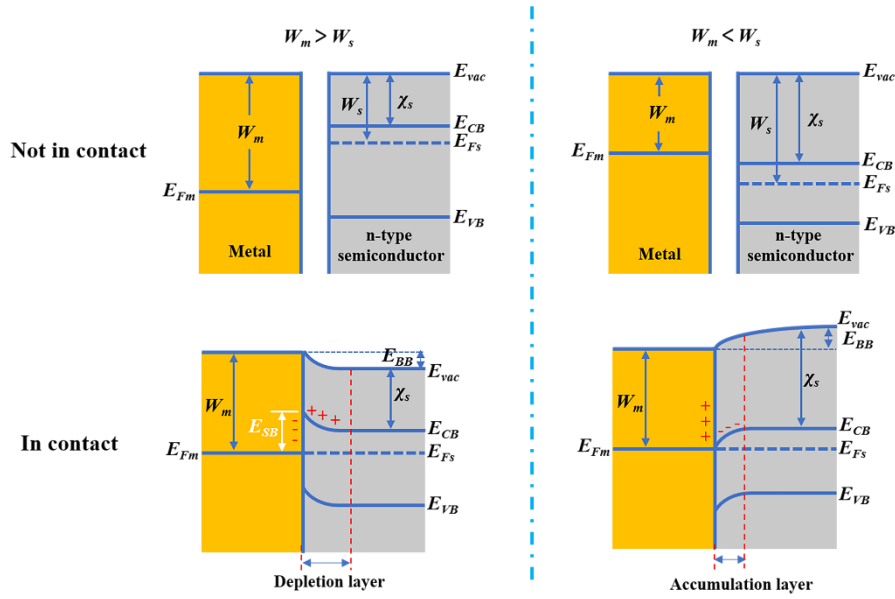


Figure 1.18 Energy band diagrams of contacted n-type semiconductor and metal. E_{vac} : vacuum energy, E_{CB} : minimum conduction band energy, E_{VB} : maximum valence band energy; E_{Fs} : semiconductor's Fermi level, E_{Fm} : metal's Fermi level.

1.4.2 Mechanism of plasmon-induced hot-electron generation⁹⁷

The plasmonic nanostructures, such as metal nanoparticles/TiO₂ systems, have been proposed for two different areas. One is to work as an effective light trapping part which is assembled into the photocatalytic systems and photovoltaic cells. The other is the direct transformation of collected photons into electricity through hot-electrons generation. Under the irradiation of incident light, the plasmonic nanocomposites induces LSPR excitation. And then, the plasmons will decay non-radiatively in a femtosecond time scale. The trapped energy is produced into electron-hole pairs and injected to the conduction band of semiconductor. The energy of those electrons is with high, usually 1-4 eV for silver nanoparticles (Ag-NPs) or Au-NPs. These highly energetic electrons are not thermal equilibrium to the atoms of the materials. Therefore, they are also called “hot-electrons.” Owing to enough kinetic energy, the hot- electrons can run away from the plasmonic metallic nanoparticles and will be gathered by the

connected semiconductor through the interfaces and forms a metal–semiconductor Schottky junction.

In general, three mechanisms can explain the separation of hot electron-hole pairs from the excited metallic nanostructure to the semiconductor (Figure 1.19).

Figure 1.19a illustrates the conventional plasmon-induced hot-electron generation mechanism. Through Landau damping, the photoexcited plasmon in metal can decay into hot electron-hole pairs. Then the hot-electrons inject into the conduction band of semiconductor in contact.

This conventional mechanism includes interfacial and distal photoelectric effect.⁹⁵ Both the energy and lifetime of the plasmon-induced hot-electrons can determine the transfer efficiency. Before flowing to the metal-semiconductor interface, the hot-electrons may recombine with the holes and also may relax through electron-electron scattering. Moreover, the energy of the hot-electrons is distributed in a broad range,⁹⁸ and most electrons are not energetic enough to surmount the Schottky barrier. Therefore, these hot-electrons are converted to heat rather than contributing to the charge separation. In most cases, therefore, the efficiency of conventional transfer mechanism is very low.

Figure 1.19b is the optical excitation process. The metal can be directly excited by light, the electrons are directly injected into the conduction band of semiconductor.⁹⁹

Figure 1.19c is a newly demonstrated mechanism, which is based on the strong interdomain mixing and coupling of semiconductor and metal levels. In this condition, the plasmon-induced hot-electrons are directly generated in the semiconductor, while holes are generated in the metal.⁹⁷

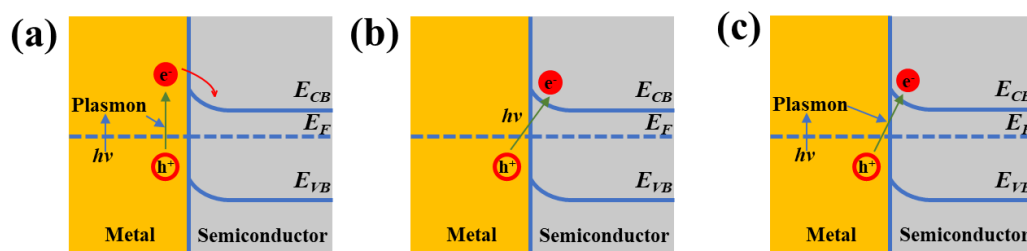


Figure 1.19 Schematics of charge separation pathways in metal-semiconductor configuration.

1.4.3 Near-field enhancement^{28,77,100-102}

Near-field is generally referred to the energetic electromagnetic field which is much higher than the energy of incident light. It is confined at the plasmonic nanostructures' surface.

In metal-semiconductor systems, the mechanism of near-field electromagnetic enhancement is on account of the interaction of the semiconductor with the energetic localized electric fields of metal under the excitation of the incident light. The strongest electric field is confined at the metal's surface. However, it will decrease exponentially with distance from the surface in 20~30 nm, and it will decrease linearly in further distance. The semiconductor will encounter these energetic electric fields when it nears to or contacts with the exciting metal nanostructure. Therefore, the efficiency of plasmon-induced electron-hole pairs generation at a nearby semiconductor via near-field enhancement is highly rely on the energy of the localized electric fields. The higher efficiency of the electron-hole generation ascribe to more intense localized electric field. As shown in Figure 1.20, in some regions of the semiconductor the rate of electron-hole pairs generation is improved in a few orders of magnitude.¹⁰³⁻¹⁰⁵

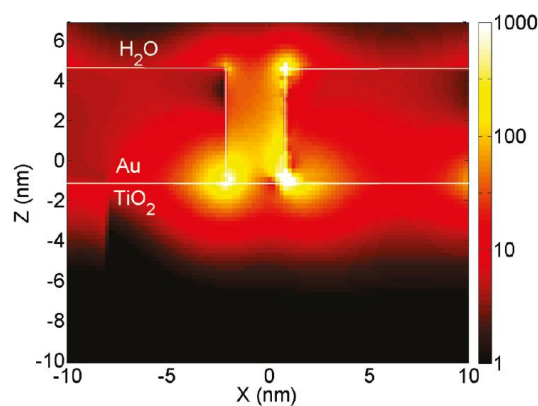


Figure 1.20 FDTD Simulation for electric field distribution of Au-TiO₂.¹⁰³

Up to now, tremendous researches have concentrated on investigating the relationship of plasmon-induced hot-electron formation and the localized electric field generated by LSPR. As shown in Figure 1.21a, Koichiro Saito et al.¹⁰⁶ could selectively

etch the bottom and top of Ag nanocubes by plasmon-induced electron-hole separation. This site-selective etching shows that the plasmonic near-field can induce the anodic reaction. Moreover, Figure 1.21b further illustrates the effects of plasmonic localized electric field intensity and distributions on the IQE of plasmon-induced electron-hole separation. Takuya Ishida et al.¹⁰⁷ revealed that the localized electric field at the surface of Au-NPs is improved by the plasmon coupling, which resulted in the improved IQE of plasmon-induced electron-hole separation.

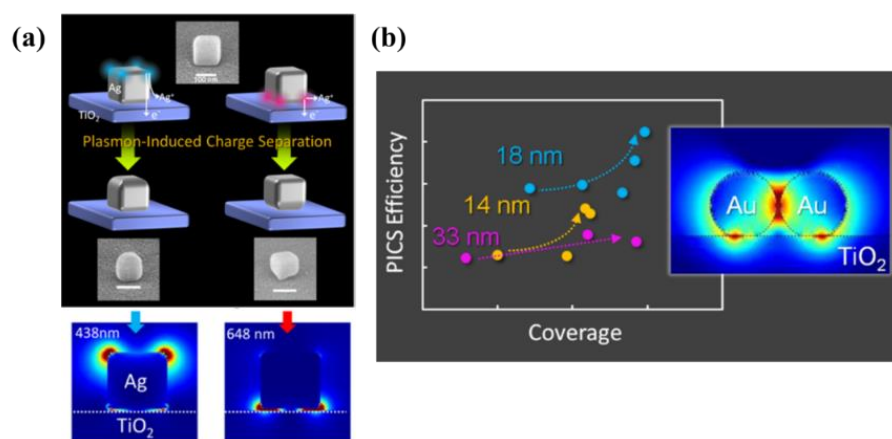


Figure 1.21 Investigation on the relationship of plasmon-induced hot-electron-hole generation and intensity of localized electric field. (a) Ag nanocubes on TiO₂¹⁰⁶ and (b) Au-NPs on TiO₂.¹⁰⁷

1.4.4 Application of plasmon-induced hot-electron generation

The transfer of hot-electrons from plasmonic nanostructures into the conduction band of the semiconductor matrix under irradiation significantly improves the conductivity of the system and also drive redox reactions. This mechanism has been extensively used in plasmon-enhanced photocatalytic degradation of organic molecules,^{108,109} water splitting,¹¹⁰ and CO₂ reduction into fuels.^{111,112} The plasmon-induced photocatalytic reactions provides a promising direction to enhance the absorption ability of the semiconductor.

Degradation of organic molecules is usually applied to evaluate photocatalytic efficiency. Parvaneh Sangpour et al.¹⁰⁸ reported photocatalytic degradation efficiency on methylene blue (MB) by TiO₂ deposited with various metal nanoparticles, and under

visible irradiation, the photocatalytic activity of Au/TiO₂ and Cu/TiO₂ were much higher (Figure 1.22a). Furthermore, Shuying Zhu et al.¹⁰⁹ found that when the dominant exposed facets of TiO₂ is {0 0 1}, the Au-NPs/TiO₂ composite tended to effectively degrade Rhodamine B (RhB) under visible light irradiation. (Figure 1.22b). Therefore, the structural and electronic properties of TiO₂ should also be crucial for higher photocatalytic efficiency.

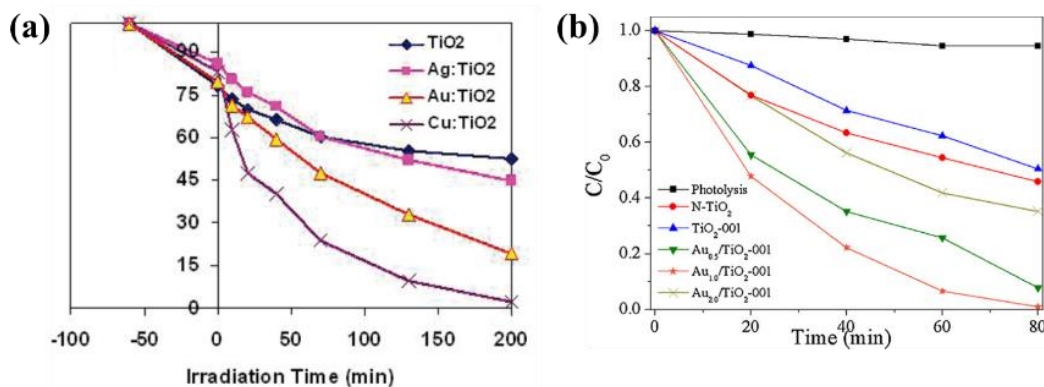


Figure 1.22 (a) Photodegradation of methylene blue (MB) with different metal (Au, Ag, Cu)/TiO₂.¹⁰⁸ (b) Photodegradation of Rhodamine B (RhB) with different Au/TiO₂.¹⁰⁹

Also, plasmonic nanostructures can facilitate water splitting under visible and near-infrared light irradiation. To date, numerous plasmonic nanoparticle/semiconductor systems have been investigated one after another. For example, with the utilization of the double sides of strontium titanate (SrTiO₃), Yuqing Zhong et al.¹¹⁰ successfully exploited a plasmon-induced water splitting system, which could be operated under irradiation by visible light (Figure 1.23). It was found that water oxidation could be facilitated by the plasmon-induced charge separation process at the interface between Au-NPs and SrTiO₃, while proton was reduced at the backside of SrTiO₃.

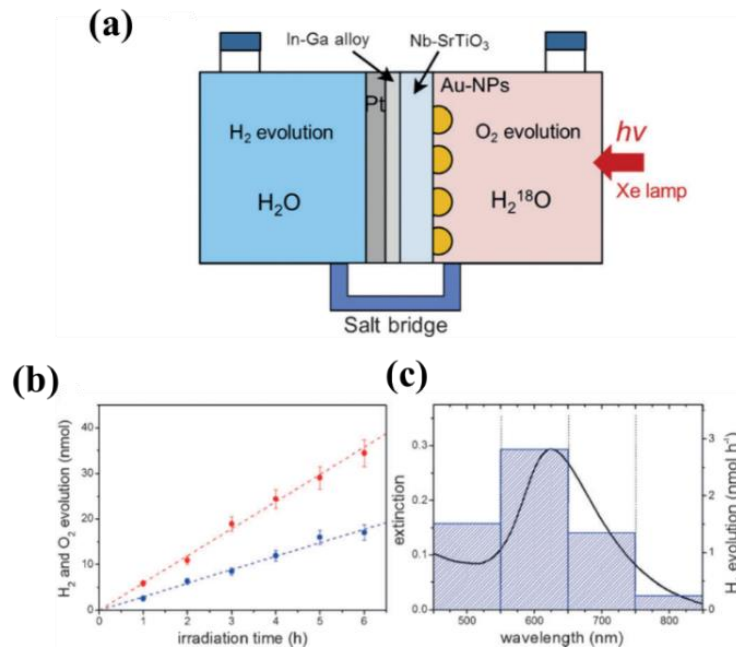


Figure 1.24 Water splitting (a) schematic, (b) and (c) experimental results of Au-NPs/Nb-SrTiO₃ photoelectrodes.¹¹⁰

In addition, photocatalytic reduction of CO₂ is considered as a promising strategy to decrease CO₂ emissions and simultaneously convert solar energy into storable chemical energy. For example, Huilei Zhao et al.¹¹¹ reported a well-designed Au/Al₂O₃/TiO₂ structure with a significant improvement in CO₂ photoreduction compared to Al₂O₃/TiO₂ (Figure 1.24). Moreover, Joseph S. DuChene et al. reported that Au/p-GaN photocathodes exhibited effective plasmon-induced photoelectrochemical CO₂ reduction.¹¹²

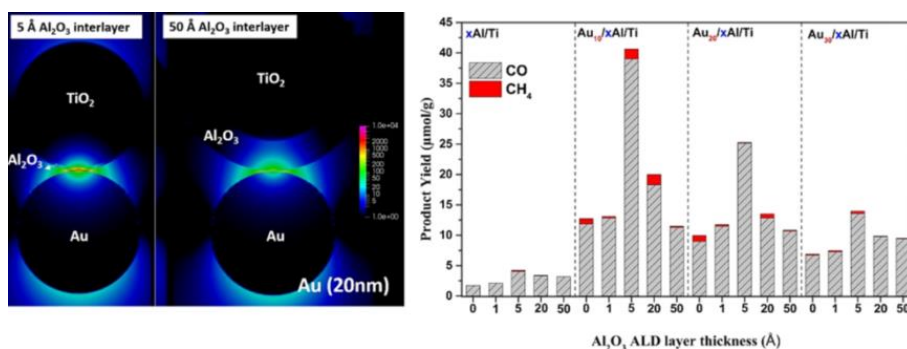


Figure 1.24 Plasmon-induced CO₂ reduction by Au/Al₂O₃/TiO₂.¹¹¹

1.5 Strong coupling of plasmon and nanocavity modes

Plasmonic photocatalysis are still featured insufficient light absorption due to the narrow-band LSPR. For the sake of improving the light harvesting efficiency of metal nanostructures, ascribing to the booming nanofabrication technologies, coupled plasmon systems with tunable spectrum and intensified near-field have been intensively studied. Nanogap dimer,^{113,114} dolmen,¹¹⁵⁻¹¹⁷ and oligomers¹¹⁸ are metal nanoparticles with short distance, which are considered as strong coupling. Metal nanostructures can also couple with optical modes, such as waveguide,¹¹⁹ cavity.¹²⁰⁻¹²³ The design of strong coupling system between plasmon and nanocavity has been developed to realize intensive and adjustable optical response. In this system, a high reflective metal layer is on the rear so that all light is channeled into the absorber layer owing to the blocked transmission by the rear.¹²⁴⁻¹²⁷ It is a promising approach to combine the plasmonic nanostructures and Fabry–Perot (FP) nanocavities together for plasmonic photocatalysis with broad and high absorption ability.¹²⁴

For example, Yuhua Lu et al.¹²¹ experimentally demonstrated the three-layered nanostructure Au-NPs/TiO₂/Au-film could efficiently harvest light across a broad wavelength range to boost the photoelectrochemical activities (Figure 1.25).

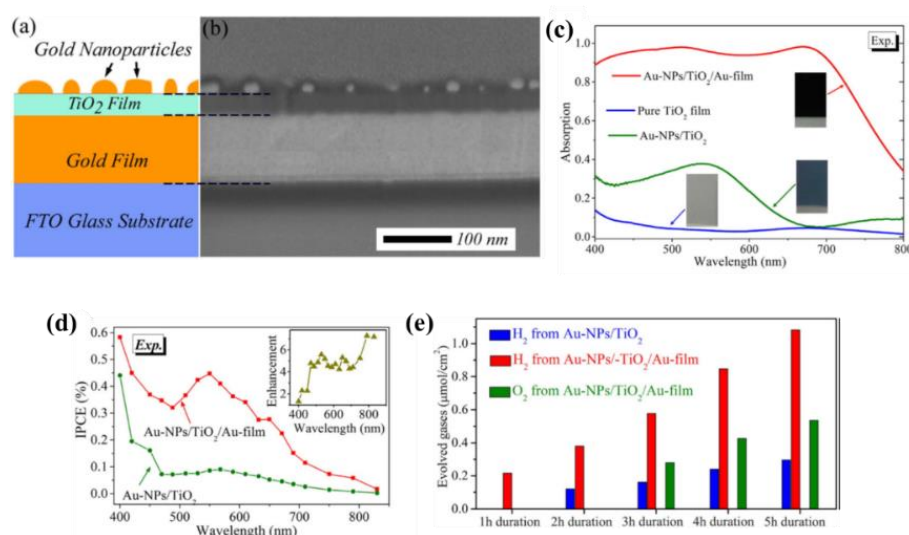


Figure 1.25 (a) Schematic, (b) SEM image, (c) absorption spectra, (d) IPCE spectra, and water splitting efficiency of Au-NPs/TiO₂/Au-film nanostructure.¹²¹

In these aforementioned Au-NP/TiO₂/Au-film nanostructures, Au-NPs are deposited on the top of TiO₂ film,^{121,123} resulting in weak interaction of cavity mode and LSPR. In order to address this disadvantage, our laboratory developed Au-NPs/TiO₂/Au-film nanostructure based on the strong coupling between FP-nanocavity and LSPR to harvest broadband light efficiently as well as facilitates water splitting reaction (Figure 1.26).¹²² In order to improve the interaction of nanocavity and LSPR, Au-NPs are partially inlaid by an additional thin TiO₂ film. The structure could absorb visible light higher than 98 % and effectively improve the IPCE compared to the structure without strong coupling.

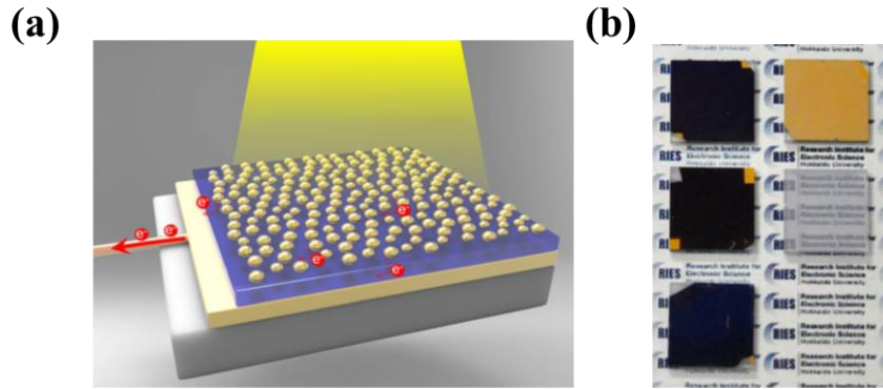


Figure 1.26 (a) Schematic and (b) Photographs of Au-NP/TiO₂/Au-film with partially inlaid Au-NPs.¹²²

Coupled harmonic oscillator model,¹¹⁹ which is usually used as the concept of strong coupling between cavity modes and an emitter, can be applied to calculate the splitting energy of the cavity and plasmon systems. In the coupled cavity-LSPR system, the LSPR field coupling strength is proportional to the LSPR dipole moment and the electric field in the cavity. The system can be described by the following Hamiltonian:

$$\begin{bmatrix} E_C & \frac{\hbar\Omega}{2} \\ \frac{\hbar\Omega}{2} & E_P \end{bmatrix} \quad (1.16)$$

where $E_C = \hbar\omega_C$ is the energy of the cavity mode. $E_P = \hbar\omega_P$ is the energy of the LSPR mode. $\hbar\Omega/2$ is the coupling constant.

After ignoring the cross-damping terms, which is the incoherent energy exchange between the uncoupled systems. The solution of the equation is given by:

$$H\Psi = \begin{bmatrix} E_C & \frac{\hbar\Omega}{2} \\ \frac{\hbar\Omega}{2} & E_P \end{bmatrix} \begin{bmatrix} \Psi_C \\ \Psi_P \end{bmatrix} = E \begin{bmatrix} \Psi_C \\ \Psi_P \end{bmatrix} \quad (1.17)$$

The eigenstate of the polariton, which consists of the eigenstates of the cavity and the LSPR, yields the dispersion of the coupled system:

$$E_{\pm}(\delta) = \frac{E_C + E_P}{2} \pm \frac{1}{2} \sqrt{(E_C - E_P)^2 + |\hbar\Omega|^2} \quad (1.18)$$

When $E_C = E_P$, the coupling system will result in a mode splitting of $\hbar\Omega$.

In addition, the strong coupling conditions based on the linewidth and the splitting energy is described as:

$$\hbar\Omega > \sqrt{\frac{\gamma_{UB}^2 + \gamma_{LB}^2}{2}} = \sqrt{\frac{\gamma_{cavity}^2 + \gamma_{LSPR}^2}{2}} \quad (1.19)$$

where $\hbar\Omega$ is the splitting energy. γ_{UB} and γ_{LB} are the linewidths of the upper and lower branches, respectively. γ_{cavity} and γ_{LSPR} are the linewidths of the nanocavity and LSPR modes, respectively.¹²²

Therefore, in order to develop plasmonic photocatalysis systems consisting of a nanocavity mode and LSPR mode with high efficiency under visible light, Eq. 1.19 can be employed to verify the structures fulfils the strong coupling conditions or not.

1.6 Outlook of this thesis

In the studies of plasmonic nanostructures, a single layer of monodispersed metallic nanoparticles decorated on TiO₂ film have been applied in most systems. Nevertheless, it is difficult for a single layer of metallic nanoparticles to harvest light efficiently, which can directly affect the generation and transformation of plasmon-induced hot electron-hole pairs in metal nanostructures. There have been numerous reports on boosting the efficiency of plasmon-induced charge separation by means of controlling the nanoparticle shape, size, interparticle distance, and so on. The studies on constructing an efficient light harvesting plasmonic system with enhanced photocurrent generation and water oxidation still deserve for investigating.

The aims of this thesis are fabrication of a novel modal strong coupling structures between the FP-nanocavity (TiO₂/Au-film) and LSPR (Au-NPs), investigation of their

hot-electrons separation properties, and further modification for enhanced photoelectrochemical performances. These studies will provide a better understanding and unique perspective to constructing plasmonic nanostructures with high photoelectrochemical and photocatalytic performances.

There are five chapters in this doctoral thesis. Chapter 1 reviews the basics and applications of surface plasmon resonance and the its related plasmon-induced charge separation process.

Chapter 2 relates to the original development strategy of the modal strong coupling photoelectrodes between FP-nanocavity and LSPR by Helicon sputter, ALD, thermal evaporation, and annealing. The morphologies, optical properties, and photoelectrochemical activity of the prepared structures are explored. The effect of Au-NP size and the inlaid depth on the properties of the prepared structures are investigated.

Chapter 3 relates to the investigation of the plasmon-induced hot-electron transfer efficiency under this modal strong coupling conditions. The effects of the modal strong coupling conditions on the IPCE and IQE by using triethanolamine (TEOA) as a sacrificial electron donor are discussed.

In Chapter 4, Au@ATA nanostructure is implemented using a facile constant potential electrolysis (CPE) technique to postdeposit Au on the modal strong coupling photoelectrode in order to tailor the near-field distribution of Au-NPs. Optical responses to deposition time and thickness of nanocavities as well as photoelectrochemical performances of the as-prepared photoelectrodes are investigated. Finite-element method (FEM) simulation is also performed to observe the distribution of near-field enhancement.

Chapter 5 makes a conclusion about this thesis.

1.7 Reference

- [1] A. Fujishima, K. Honda, *Nature*, **1972**, *238*, 37-38.
- [2] X. B. Chen, S. S. Mao, *Chem. Rev.*, **2007**, *107*, 2891-2959.
- [3] K. Nakata, A. Fujishima, *J. Photoch. Photobio. C*, **2012**, *13*, 169-189.
- [4] A. Y. Meng, L. Y. Zhang, B. Cheng, J. G. Yu, *Adv. Mater.*, **2019**, *31*, 1807660-1807690.
- [5] Y. Nishijima, K. Ueno, Y. Yokota, K. Murakoshi, H. Misawa, *J. Phys. Chem. Lett.*, **2010**, *1*, 2031-2036.
- [6] X. M. Zhang, Y. L. Chen, R.-S. Liu, D. P. Tsai, *Rep. Prog. Phys.*, **2013**, *76*, 046401.
- [7] S. Mubeen, J. Lee, N. Singh, S. Krämer, G. D. Stucky, M. Moskovits, *Nat. Nanotech.*, **2013**, *8*, 247-251.
- [8] Clavero, C, *Nat. Photon.*, **2014**, *8*, 95-103.
- [9] K. Kneipp, H. Kneipp, I. Itzkan, R. R. Dasari, M. S. Feld, *J. Phys.: Condens. Matter*, **2002**, *14*, R597-R624.
- [10] S. Linic, P. Christopher, D. B. Ingram, *Nat. Mater.*, **2011**, *10*, 911-921.
- [11] T. Oshikiri, K. Ueno, H. Misawa, *Angew. Chem. Int. Ed.*, **2014**, *53*, 9802-9805.
- [12] K. Ueno, H. Misawa, *J. Photoche. Photobio. C*, **2013**, *15*, 31-52.
- [13] D. B. Ingram, S. Linic, *J. Am. Chem. Soc.*, **2011**, *133*(14), 5202-5205.
- [14] <https://www.amusingplanet.com/2016/12/lycurgus-cup-piece-of-ancient-roman.html>
- [15] S. A. Maier, Plasmonics: fundamentals and applications. *Springer Science & Business Media*, **2007**.
- [16] L. J. Mendoza Herrera, D. M. Arboleda, D. C. Schinca, L. B. Scaffardi, *J. Appl. Phys.*, **2014**, *116*, 233105.
- [17] G. V. Hartland, *Chem. Rev.*, **2011**, *111*, 3858-3887.
- [18] C. Louis, O. Pluchery, *World Scientific*, **2017**.
- [19] P. B. Johnson, R. W. Christy, *Phys. Rev. B*, **1972**, *6*, 4370-4379.
- [20] H. Wang, F. Tam, N. K. Grady, N. J. Halas, *J. Phys. Chem. B*, **2005**, *109*, 18218-18222.
- [21] Y. Chen, H. Ming, *Photonic Sensors*, **2012**, *2*, 37-49.
- [22] A. Campion, P. Kambhampati, *Chem. Soc. Rev.*, **1998**, *27*, 241-250.
- [23] C. L. Haynes, A. D. McFarland, R. P. V. Duyne, *Anal. Chem.*, **2005**, *77*, 338 A-346 A.
- [24] C. Sonnichsen, B. M. Reinhard, J. Liphardt, A. P. Alivisatos, *Nat Biotech*, **2005**, *23*, 741-745.
- [25] K. Kneipp, Y. Wang, H. Kneipp, L. T. Perelman, I. Itzkan, R. R. Dasari, M. S. Feld, *Phys. Rev. Lett.*, **1997**, *78*, 1667-1670.
- [26] N. C. Jeong, C. Prasittichai, J. T. Hupp, *Langmuir*, **2011**, *27*, 14609-14614.
- [27] Y. H. Su, Y. F. Ke, S. L. Cai, Q. Y. Yao, *Light Sci. Appl.*, **2012**, *1*, e14.
- [28] W. B. Hou, S. B. Cronin, *Adv. Funct. Mater.*, **2013**, *23*, 1612-1619.
- [29] T. Holmgaard, S. I. Bozhevolnyi, *Phys. Rev. B*, **2007**, *75*, 245405-12.
- [30] G. R. Zhang, H. Liu, S. T. Jia, H. Y. Li, Z. Li, Q. H. Gong, J. J. Chen, *Adv. Quantum Technol.*, **2020**, *3*, 2000033-2000041.
- [31] S. Kawata, M. Ohtsu, M. Irie, *Springer*, **2001**.
- [32] M. Futamata, *J. Phys. Chem.*, **1995**, *99*, 11901-11908.
- [33] X. G. Luo, J. P. Shi, H. Wang, G. B. Yu, *Mod. Phys. Lett. B*, **2004**, *18*, 945-953.
- [34] D. Derkacs, S. H. Lim, P. Matheu, W. Mara, E. T. Yu, *Appl. Phys. Lett.*, **2006**, *89*, 093103.
- [35] S. M. Tripathi, A. Kumar, E. Marin, J. Meunier, *J. Lightwave Technol.*, **2008**, *26*, 1980-1985, 2008.
- [36] L. M. Wu, J. Guo, H. L. Xu, X. Y. Dai, Y. J. Xiang, *Photonics Res.*, **2016**, *4*, 262-266.
- [37] J. X. Zhang, L. D. Zhang, W. Xu, *J. Phys. D: Appl. Phys.*, **2012**, *45*, 113001 (19pp).
- [38] J. F. O'Hara, R. D. Averitt, A. J. Taylor, *Optics Express*, **2005**, *16*, 6117-6126.
- [39] P. Andrew, W. L. Barnes, *Science*, **2004**, *306*, 1002-1005.

- [40] T. Søndergaard, S. I. Bozhevolnyi, A. Boltasseva, *Phys. Rev. B*, **2006**, *73*, 045320.
- [41] K. L. Kelly, E. Coronado, L. L. Zhao, G. C. Schatz, *J. Phys. Chem. B*, **2003**, *107*, 668-677.
- [42] S. K. Ghosh, T. Pal, *Chem. Rev.*, **2007**, *107*, 4797-4862.
- [43] G. Mattei, P. Mazzoldi, H. Bernas, Metal nanoclusters for optical properties. Springer, Berlin, Heidelberg, **2009**, 287-316.
- [44] G. Mie, *Ann. Phys.*, **1908**, *25*, 377-445.
- [45] W. L. Barnes, A. Dereux, T. W. Ebbesen, *Nature*, **2003**, *424*, 824-830.
- [46] P. Mulvaney, J. Pérez-Juste, M. Giersig, L. M. Liz-Marzán, C. Pecharromán, *Plasmonics*, **2006**, *1*, 61-66.
- [47] C. Novo, A. M. Funston, A. K. Gooding, P. Mulvaney, *J. Am. Chem. Soc.*, **2009**, *131*, 14664-14666.
- [48] A. Zilli, W. Langbein, P. Borri, *ACS Photonics*, **2019**, *6*, 2149-2160.
- [49] T. Ming, H. J. Chen, R. B. Jiang, Q. Li, J. F. Wang, *J. Phys. Chem. Lett.*, **2012**, *3*, 191-202.
- [50] Y. Huang, L. W. Ma, M. J. Hou, J. H. Li, Z. Xie, Z. J. Zhang, *Scientific Reports*, **2016**, *6*, 30011.
- [51] R. B. Jiang, B. X. Li, C. H. Fang, J. F. Wang, *Adv. Mater.*, **2014**, *26*, 5274-5309.
- [52] T. K. Sau, A. L. Rogach, F. Jäckel, T. A. Klar, J. Feldmann, *Adv. Mater.*, **2010**, *22*, 1805-1825.
- [53] X. S. Kou, W. H. Ni, C. K. Tsung, K. Chan, H. Q. Lin, G. D. Stucky, J. F. Wang, *Small*, **2007**, *3*, 2103-2113.
- [54] N. R. Jana, T. Pal, *Adv. Mater.*, **2007**, *19*, 1761-1765.
- [55] N. C. Lindquist, P. Nagpal, K. M. McPeak, D. J. Norris, S. H. Oh, *Rep. Prog. Phys.*, **2012**, *75*, 036501.
- [56] J. Reguera, J. Langer, D. J. de Aberasturi, and L. M. Liz-Marzán, *Chem. Soc. Rev.*, **2017**, *46*, 3866-3885.
- [57] Z. W. Liu, W. B. Hou, P. Pavaskar, M. Aykol, S. B. Cronin, *Nano Lett.*, **2011**, *11*, 1111-1116.
- [58] M. Ihara, M. Kanno, S. Inoue, *Physica E*, **2010**, *42*, 2867-2871.
- [59] C. Nahm, H. Choi, J. Kim, D. R. Jung, C. Kim, J. Moon, B. Lee, B. Park, *Appl. Phys. Lett.*, **2011**, *99*, 253107.
- [60] Y. Li, H. Wang, Q. Feng, G. Zhou, Z. S. Wang, *Energy Environ. Sci.*, **2013**, *6*, 2156-2165.
- [61] P. Du, P. Jing, D. Li, Y. Cao, Z. Liu, Z. Sun, *Small*, **2015**, *11*, 2454-2462.
- [62] G. M. Kim, T. Tatsuma, *J. Phys. Chem. C*, **2017**, *121*, 11693-11699.
- [63] P. K. Jain, K. S. Lee, I. H. El-Sayed, M.A. El-Sayed, *J. Phys. Chem. B*, **2006**, *110*, 7238-7248.
- [64] S. W. Wang, W. Xi, F. H. Cai, X. Y. Zhao, Z. P. Xu, J. Qian, S. L. He, *Theranostics*, **2015**, *5*, 251-266.
- [65] C. Sönnichsen, T. Franzl, T. Wilk, G. von Plessen, J. Feldmann, O. Wilson, P. Mulvaney, *Phys. Rev. Lett.*, **2002**, *88*, 077402.
- [66] K. M. Mayer, J. H. Hafner, *Chem. Rev.*, **2011**, *111*, 3828-3857.
- [67] K. Ueno, T. Oshikiri, Q. Sun, X. Shi, H. Misawa, *Chem. Rev.*, **2018**, *118*, 2955-2993.
- [68] J. Reguera, J. Langer, D. J. Aberasturi, L. M. Liz-Marzán, *Chem. Soc. Rev.*, **2017**, *46*, 3866-3885.
- [69] M. A. Mahmoud, M. A. El-Sayed, *Phys. Chem. Lett.*, **2013**, *4* (9), 1541-1545.
- [70] W. Wang, S. Wu, K. Reinhardt, Y. Lu, S. Chen, *Nano Lett.*, **2010**, *10*, 2012-2018.
- [71] J. Qi, X. Dang, P. T. Hammond, A. M. Belcher, *ACS Nano*, **2011**, *5*, 7108-7116.
- [72] N. Yeh, P. Yeh, *Renewable Sustainable Energy Rev.*, **2013**, *21*, 421-431.
- [73] D. W. Zhao, M. Y. Yu, L. L. Zheng, M. Li, S. J. Dai, D. C. Chen, T. C. Lee, D. Q. Yun, *ACS Appl. Energy Mater.*, **2020**, *3*, 9568-9575.
- [74] M. Pelton, J. Aizpurua, G. Bryant, *Laser & Photon. Rev.*, **2008**, *2*, 136-159.
- [75] H. Yu, Q. Sun, J. H. Yang, K. Ueno, T. Oshikiri, A. Kubo, Y. Matsuo, Q. H. Gong, H. Misawa, *Optics Express*, **2017**, *25*, 6883-6894.
- [76] H. Yu, Q. Sun, K. Ueno, T. Oshikiri, A. Kubo, Y. Matsuo, H. Misawa, *ACS Nano*, **2016**, *10*, 10373-10381.
- [77] S. Gwo, H. Y. Chen, M. H. Lin, L. Y. Sun, X. Q. Li, *Chem. Soc. Rev.*, **2016**, *45*, 5672-5716.
- [78] H. J. Chen, L. Shao, Q. Lia, J. F. Wang, *Chem. Soc. Rev.*, **2013**, *42*, 2679-2724.
- [79] Y. Q. Sun, L. F. Hang, D. D. Men, H. L. Li, D. L. Liu, X. Y. Li, L. L. Wen, Y. Li, *J. Mater. Chem. C*, **2016**, *4*,

9864-9871.

- [80] A. Gole, C. J. Murphy, *Chem. Mater.*, **2004**, *16*, 3633-3640.
- [81] S. Hong, K. L. Shuford, S. Park, *Chem. Mater.*, **2011**, *23*, 2011-2013.
- [82] M. Rycenga, J. M. McLellan, Y. Xia, *Adv. Mater.*, **2008**, *20*, 2416-2420.
- [83] A. Tao, P. Sinsersuksakul, P. Yang, *Angew. Chem., Int. Ed.*, **2006**, *45*, 4597-4601.
- [84] B. J. Wiley, Y. Xiong, Z. Y. Li, Y. Yin, Y. Xia, *Nano Lett.*, **2006**, *6*, 765-768.
- [85] C. J. Murphy, T. K. Sau, A. M. Gole, C. J. Orendorff, J. Gao, L. Gou, S. E. Hunyadi, T. Li, *J. Phys. Chem. B*, **2005**, *109*, 13857-13870.
- [86] C. Xue, J. E. Millstone, S. Li, C. A. Mirkin, *Angew. Chem., Int. Ed.*, **2007**, *46*, 8436-8439.
- [87] C. Kan, X. Zhu, G. Wang, *J. Phys. Chem. B*, **2006**, *110*, 4651-4656.
- [88] R. Jin, Y. C. Cao, E. Hao, G. S. Me'traux, G. C. Schatz, C. A. Mirkin, *Nature*, **2003**, *425*, 487-490.
- [89] S. Link, M. B. Mohamed, M. A. El-Sayed, *J. Phys. Chem. B*, **1999**, *103*, 3073-3077.
- [90] F. Dumestre, B. Chaudret, C. Amiens, M. Respaud, P. Fejes, P. Renaud, P. Zurcher, *Angew. Chem., Int. Ed.*, **2003**, *42*, 5213-5216.
- [91] A. A. Tseng, *J. Micromech. Eng.*, **2004**, *14*, R15-R34.
- [92] X. Shi, K. Ueno, T. Oshikiri, H. Misawa, *J. Phys. Chem. C*, **2013**, *117*, 24733-24739.
- [93] X. Shi, K. Ueno, N. Takabayashi, H. Misawa, *J. Phys. Chem. C*, **2013**, *117*, 2494-2499.
- [94] Y. Tian, T. Tatsuma, *Chem. Commun.*, **2004**, *16*, 1810-1811.
- [95] Y. Tian, T. Tatsuma, *J. Am. Chem. Soc.*, **2005**, *127*, 7632-7637.
- [96] Z. Zhang, J. T. Yates, Jr, *Chem. Rev.*, **2012**, *112*, 5520-5551.
- [97] K. Wu, J. Chen, J. R. McBride, T. Lian, *Science*, **2015**, *349* (6248), 632-635.
- [98] Y. Zhang, C. Yam, G. C. Schatz, *J. Phys. Chem. Lett.*, **2016**, *7*, 1852-1858.
- [99] D. M. Kolb, M. Przasnyski, H. Gerischer, *Phys. Chem.*, **1974**, *93*, 1-14.
- [100] Y. H. Jang, Y. J. Jang, S. Kim, L. N. Quan, K. Chung, D. H. Kim, *Chem. Rev.*, **2016**, *116*, 14982-15034.
- [101] S. Linic, P. Christopher, D. B. Ingram, *Nat. Mater.*, **2011**, *10*, 911-921.
- [102] A. Agrawal, S. H. Cho, O. Zandi, S. Ghosh, R. W. Johns, D. J. Milliron, *Chem. Rev.*, **2018**, *118*, 3121-3207.
- [103] M. Murdoch, G. I. N. Waterhouse, M. A. Nadeem, J. B. Metson, M. A. Keane, R. F. Howe, J. Llorca, H. Idriss, *Nat. Chem.*, **2011**, *3*, 489-492.
- [104] J. Lee, T. Javed, T. Skeini, A. O. Govorov, G. W. Bryant, N. A. Kotov, *Angew. Chem. Int. Ed.*, **2006**, *45*, 4819-4823.
- [105] P. Anger, P. Bharadwaj, L. Novotny, *Phys. Rev. Lett.*, **2006**, *96*, 113002.
- [106] K. Saito, I. Tanabe, T. Tatsuma, *J. Phys. Chem. Lett.*, **2016**, *7*, 4363-4368.
- [107] T. Ishida, Tetsu Tatsuma, *J. Phys. Chem. C*, **2018**, *122*, 26153-26159.
- [108] P. Sangpour, F. Hashemi, A. Z. Moshfegh, *J. Phys. Chem. C*, **2010**, *114*, 13955-13961.
- [109] S. Y. Zhu, S. J. Liang, Q. Gu, L. Y. Xie, J. X. Wang, Z. X. Ding, P. Liu, *Appl. Catal. B: Environ.*, **2012**, *119-120*, 146-155.
- [110] Y. Q. Zhong, K. Ueno, Y. Mori, X. Shi, T. Oshikiri, K. Murakoshi, H. Inoue, H. Misawa, *Angew. Chem. Int. Ed.*, **2014**, *53*, 10350-10354.
- [111] H. L. Zhao, X. Zheng, X. H. Feng, Y. Li, *J. Phys. Chem. C*, **2018**, *122*, 18949-18956.
- [112] J. S. DuChene, G. Tagliabue, A. J. Welch, W. H. Cheng, H. A. Atwater, *Nano Lett.*, **2018**, *18*, 2545-2550.
- [113] K. L. Wustholz, A. I. Henry, J. M. McMahon, R. G. Freeman, N. Valley, M. E. Piotti, M. J. Natan, G. C. Schatz, R. P. Van Duyne, *J. Am. Chem. Soc.*, **2010**, *132*, 10903-10910.
- [114] B. Metzger, M. Hentschel, T. Schumacher, M. Lippitz, X. Ye, C. B. Murray, B. Knabe, K. Buse, H. Giessen, *Nano Lett.*, **2014**, *14*, 2867-2872.

- [115] N. Verellen, Y. Sonnefraud, H. Sobhani, F. Hao, V. V. Moshchalkov, P. Van Dorpe, P. Nordlander, S. A. Maier, *Nano Lett.*, **2009**, *9*, 1663-1667.
- [116] B. Luk'yanchuk, N. I. Zheludev, S. A. Maier, N. J. Halas, P. Nordlander, H. Giessen, C. T. Chong, *Nat. Mater.*, **2010**, *9*, 707-715.
- [117] N. J. Halas, S. Lal, W. S. Chang, S. Link, P. Nordlander, *Chem. Rev.*, **2011**, *111*, 3913-3961.
- [118] M. Hentschel, M. Saliba, R. Vogelgesang, H. Giessen, A. P. Alivisatos, N. Liu, *Nano Lett.*, **2010**, *10*, 2721-2726.
- [119] A. Christ, S. G. Tikhodeev, N. A. Gippius, J. Kuhl, H. Giessen, *Phys. Rev. Lett.*, **2003**, *91*, 183901.
- [120] K. T. Lin, H. L. Chen, Y. S. Lai, C. C. Yu, *Nat. Commun.*, **2014**, *5*, 3288-3288.
- [121] Y. H. Lu, W. Dong, Z. Chen, A. Pors, Z. L. Wang, S. I. Bozhevolnyi, *Scientific Reports*, **2016**, *6*, 30650.
- [122] X. Shi, K. Ueno, T. Oshikiri, Q. Sun, K. Sasaki, H. Misawa, *Nat. Nanotechnol.*, **2018**, *13*, 953-958.
- [123] C. Ng, J. J. Cadusch, S. Dligatch, A. Roberts, T. J. Davis, P. Mulvaney, D. E. Gómez, *ACS Nano*, **2016**, *10*, 4704-4711.
- [124] C. Hägglund, G. Zeltzer, R. Ruiz, A. Wangperawong, K. E. Roelofs, S. F. Bent, *ACS Photonics*, **2016**, *3*, 456-463.
- [125] Hägglund, C. Apell, S. P. *Opt. Express*, **2010**, *18*, A343-A356.
- [126] H. Song, L. Guo, Z. Liu, K. Liu, X. Zeng, D. Ji, N. Zhang, H. Hu, S. Jiang, Q. Gan, *Adv. Mater.*, **2014**, *26*, 2737-2743.
- [127] M. A. Kats, R. Blanchard, P. Genevet, F. Capasso, *Nat. Mater.*, **2013**, *12*, 20-24.

Chapter 2 Size effect on the Modal Strong Coupling Conditions

2.1 Introduction

Numerous types of gold nanoparticles (Au-NPs)/TiO₂ nanocomposites have been widely investigated due to the plasmon-enhanced light absorption ability of TiO₂ in visible and sometimes even in near infrared region.¹⁻⁹ It is very easy to tune the optical responses by changing the size, shape and composition of Au-NPs.¹⁰ However, it is relatively difficult for the single-layered Au-NPs to effectively harvest light because of the narrow-band localized surface plasmon resonance (LSPR). Therefore, for the sake of improving the light absorption, photoelectrodes with three-layered metal-dielectric-metal architectures have been developed.¹¹⁻¹⁵ This kind of nanostructure can support gap plasmon resonance. As a result, magnetic surface currents can be effectively induced as well as electric can be equivalently caused to happen. Therefore, destructive and interferential reflected waves are produced under this condition.¹⁶ Based on this mechanism, this three-dimensional structure is insensitive to the irradiation angle and polarization, and especially inert to the periodicity.¹⁶ Additionally, it has been investigated that these three-dimensional structures can achieve intensive broadband absorption with the utilization of feasibly produced differently-sized and randomly arrayed metallic nanoparticles.^{17,13-15} Furthermore, these efficient aforementioned plasmonic nanostructures have been recently investigated the promising application in water splitting as well as photocurrent increment.^{13,14}

Based on our previous results about strong coupling,¹⁸ in this chapter, Au-NPs/TiO₂/Au-film (ATA) structure with intensified and broadband visible light absorption capacity is developed. The size effect of Au-NPs on the modal strong coupling conditions, the optical properties, and the plasmon-induced photoelectrochemical performances are researched.

2.2 Experimental section

2.2.1 Fabrication of Au-NPs/TiO₂/Au-film photoelectrodes

As shown in Figure 2.1, a $10 \times 10 \times 1.0 \text{ mm}^3$ silica (SiO₂) glass was used as the substrate. It was cleaned by ultrasonic for 5 min each sequentially in acetone, methanol, and ultrapure water. Then, a pure nitrogen flow was used to dry the clean substrate. By using a Helicon sputtering system (ULVAC, MPS-4000C1/HC1), 100 nm Au film and a 2 nm titanium film were deposited sequentially on the surface of SiO₂. After that, a commercial hot-wall flow-type atomic layer deposition (ALD) reactor (SUNALETM R series (Picosun)) was used to deposit a thin layer of 28 nm titanium dioxide (TiO₂). Titanium tetrachloride (TiCl₄) and H₂O were used as TiO₂ precursors. The deposition temperature maintained in 300 °C. To prepare the dispersed Au-NPs, 3 nm discontinuous Au thin film was firstly thermal evaporated on TiO₂ surface with a rate of $0.1 \text{ \AA} \cdot \text{s}^{-1}$, and then annealed in air at 300 °C for 2 h. The size of Au-NPs could be regulated by controlling the thickness of the evaporated Au thin film. In order to obtain partially embedded Au-NPs, an additional thin layer of TiO₂ was deposited by ALD, and the sample was subsequently annealed in air at 300 °C for 2 h. The inlaid depth of the Au-NPs could be manipulated by changing the thickness of the additionally deposited TiO₂.

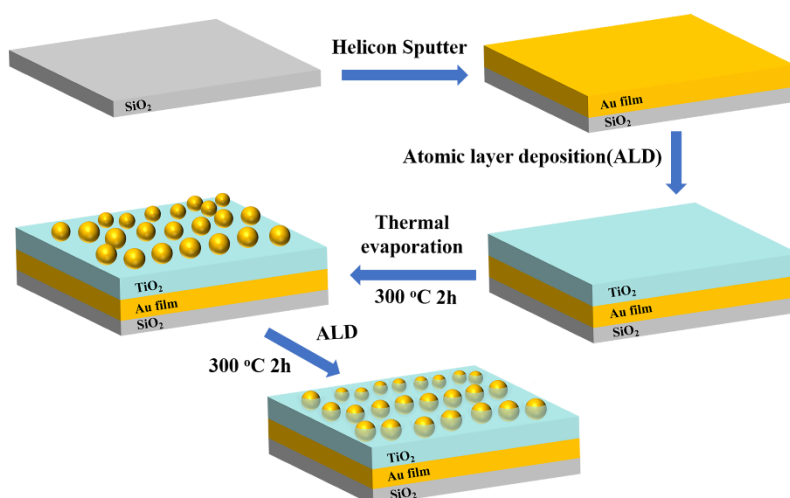


Figure 2.1 Schematic preparation of Au-NPs/TiO₂/Au-film (ATA) structure.

2.2.2 Characterizations

Photonic multichannel analyzer (PMA-11 (Hamamatsu Photonics)), which is equipped with an optical microscope (BX-51 (Olympus)), could measure the reflection (R) and transmission (T) spectra of the as-prepared structures. For the measurements, the numerical aperture of the objective lens was 0.5.

The surface morphology was observed by ultra-high-resolution scanning electron microscope (SU8230 (HITACHI)) with a maximum resolution of 0.8 nm at an electron accelerating voltage of 15 kV.

The cross-section was analyzed by high-resolution transmission electron microscopy (JEOL ARM (200 F) 200 kV FEG-STEM/TEM) with a resolution of 75 pm at an electron accelerating voltage of 200 kV.

2.2.3 Photoelectrochemical measurement

A three-electrode system was used to measure the photoelectrochemical performance of the as-prepared photoelectrodes (Figure 2.2). The obtained structure was used as the working electrode (WE.). Saturated calomel electrode (SCE) was used as the reference electrode (RE). Platinum (Pt) wire was used as the counter electrode (CE).

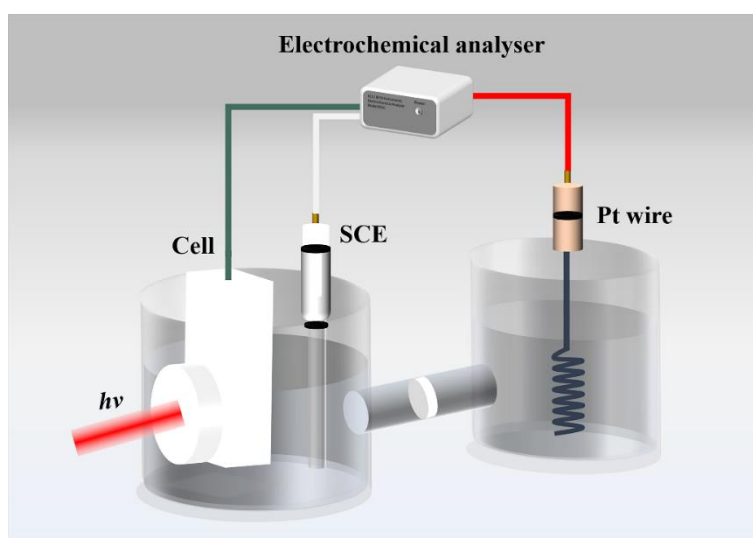


Figure 2.2 Experiment setups for photoelectrochemical measurements.

For the preparation of the WE, shown in Figure 2.3, In-Ga alloy (4 :1 weight ratio) film was firstly pasted onto the back of the as-prepared structure. Then, the structure was connected to the electrochemical analyser (ALS/CH Instruments Model 852C) with a copper lead wire. 100 mL 0.1 mol•dm⁻³ KOH aqueous solution was used as electrolyte. The light source was 800 W xenon lamp.

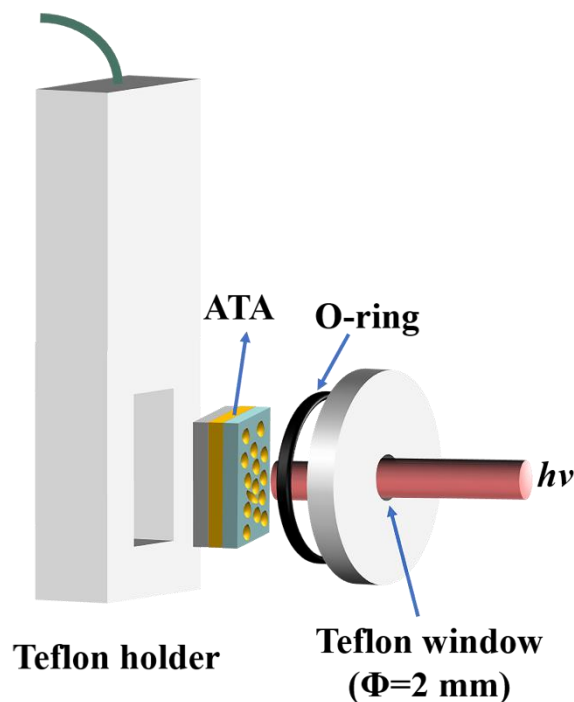


Figure 2.3 Schematic illustration of working electrode cell.

For the IPCE calculation, a bias with +0.3 V vs. SCE was applied to measure *i-t* curves to calculate the photocurrent. Then, the IPCE is obtained by applying the following equation:

$$IPCE(\lambda) = \frac{1240 \times I (A/cm^2)}{\lambda(nm) \times P (W/cm^2)} \quad (2.1)$$

where *I* is the photocurrent density under the irradiation of monochromatic light, λ is the wavelength of the monochromatic incident light, and *P* is the light intensity.

2.3 Results and discussions

2.3.1 Dependence on the size of Au-NPs

(1) Morphologies of Au-NPs

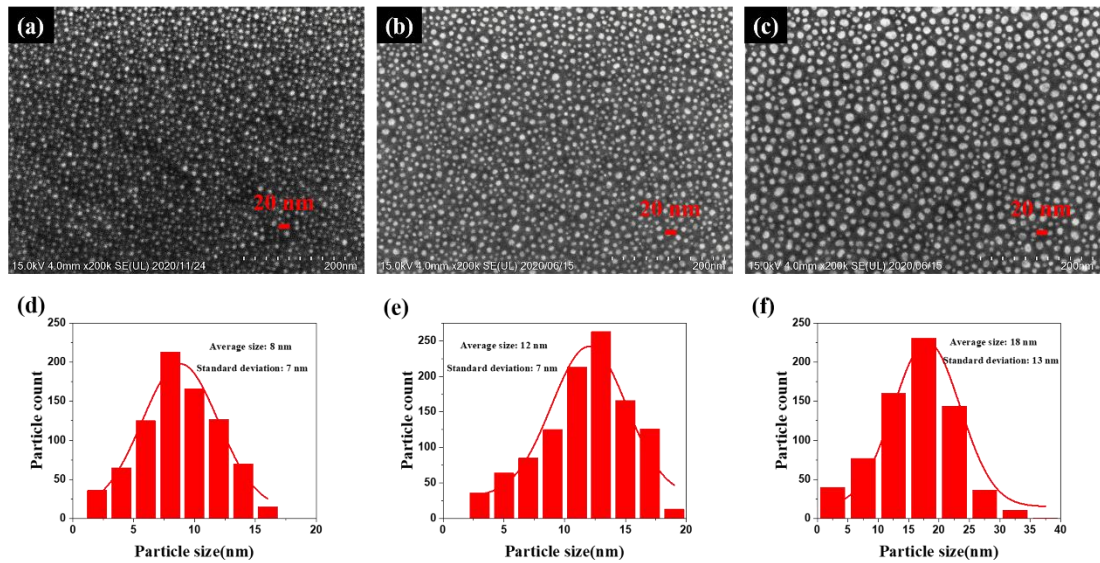


Figure 2.4 SEM images and size distributions of ATA structures with different Au-NP size. (a) and (d) 8 nm, (b) and (e) 12 nm, (c) and (f) 18 nm.

Figure 2.4 is the surface morphologies and size distributions of Au-NPs/TiO₂/Au-film (ATA) structures with different Au-NPs size prepared by thermal evaporation. It is clearly observed that a monolayer of Au-NPs with a relatively large size distribution is dispersed on the surface of TiO₂. As shown in Figure 2.4, 8 nm, 12 nm and 18 nm Au-NP size is corresponding to the Au film thickness 2 nm, 3 nm, 4 nm, respectively. The size of Au-NPs can be regulated vis changing the thickness of the initial thermal evaporated Au film. For example, by analyzing Figure 2.4b, the surface coverage of Au-NPs generated from 3 nm Au film is estimated at about 30%. The corresponding size distribution is well fitted with the Gaussian fitting. The average size is 12 nm and the standard deviation is 7 nm (Figure 2.4e).

(2) Optical properties

According to the previous reports,¹³ either the Au-NPs size or the thickness of TiO₂ can manipulate the optical properties of ATA structures. Therefore, the most intense and widest absorption spectrum of the ATA structure can be achieved under the optimal values of these two parameters.

Figure 2.5 is photographs of the structures with only 100 nm Au-film, TiO₂/Au-film, ATA with Au-NP size of 8 nm, 12 nm, 18 nm (left panel). The surface color of a thick

layer of Au-film is yellow. Also, the color of TiO₂/Au-film without Au-NPs is orange. However, the surface colors of ATA structures with different Au-NPs size appear dark blue, indicating intensified light absorption. The right panel of Figure 2.5 is photographs of ATA structures with inlaid depths of 3.5 nm, 7 nm, 14 nm, Au-NPs/TiO₂ and Au-NPs/TiO₂ with 7 nm inlaid depth. For comparison, the surface color of Au-NPs/TiO₂ obviously proves that the structure is translucent because of the insufficient absorption ability of the single layer of Au-NPs, which is further verified through the absorption spectra (Figure 2.9).

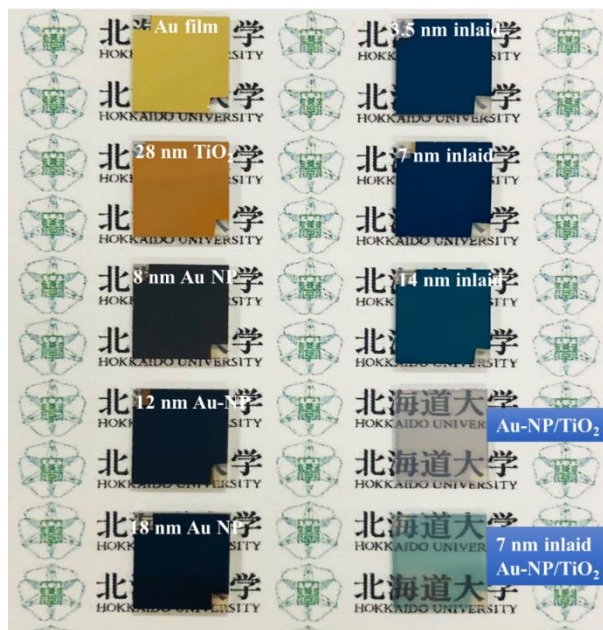


Figure 2.5 Photographs of different structures.

In order to detect the optical properties of the fabricated ATA structures with different Au-NP size, the reflection (R) and transmission (T) are measured by PMA. The corresponding absorption is calculated as $I-T-R$. The absorption spectra of ATA structures with different Au-NP size are shown in Figure 2.6. The absorption spectra of Au-NPs/TiO₂ and TiO₂/Au-film are also plotted together into Figure 2.6. The black line illustrates the absorption spectrum of TiO₂/Au-film. The absorption shorter than 500 nm is attribute to the interband transition of Au. As expected, Au-NPs/TiO₂ exhibits a single-band absorption at around 590 nm. The highest absorption value is about 13 %. This absorption peak is characteristic LSPR band when Au-NPs decorated on high

refractive materials.⁶ However, ATA structures with different sized Au-NPs exhibit relatively increased and wide absorption ability at wavelength longer than 550 nm with a remarkably high absorption value of up to 93%. When compared to the highest absorption value of Au-NPs/TiO₂ without the reflecting layer (no Au film), there is about 7-fold increase in that of ATA structures. In addition, the absorption spectra of ATA structures become wider by increasing the size of Au-NPs since the particle size is one of the crucial factors on the optical properties of Au-NPs.¹⁹

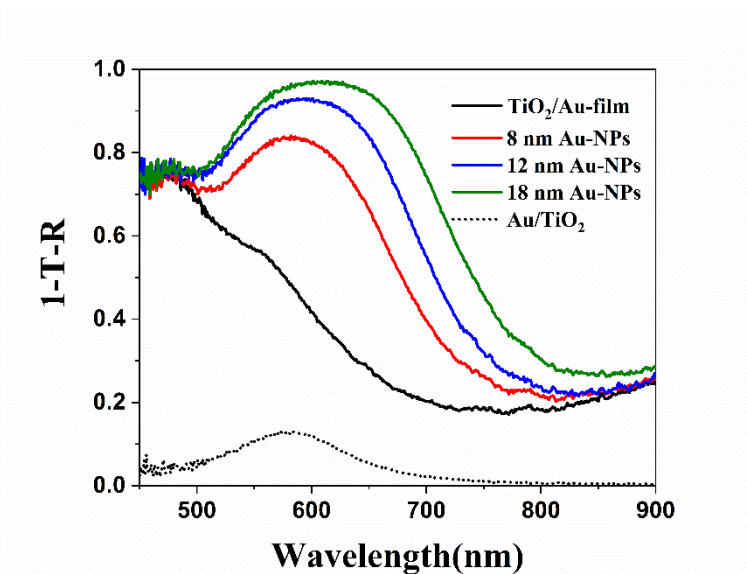


Figure 2.6 Absorption spectra of ATA structures with different Au-NPs size.

(3) Dependence of photoelectrochemical properties on Au-NPs

Photoelectrochemical measurements are carried out in a three-electrode system to assess the monochromatic incident photon-to-electron conversion efficiency (IPCE) of the photoelectrodes (Figure 2.2). Notably, there is no sacrificial electron donor in the KOH electrolyte, and therefore water oxidation will occur. Figure 2.7a shows the IPCE spectra of ATA structures with different Au-NPs size. The IPCE spectra correspond to the absorption spectra (Figure 2.6) and the highest IPCE values locate at around 600 nm. As reported, for the wavelength shorter than 500 nm, the photocurrent generation is likely determined by the intrinsic light absorption of Au, which is on the basis of the interband transition from d-band to the conduction band.² While the IPCE values correspond well to the absorption spectra at a wavelength longer than 600 nm,

indicating that LSPR can induce the photocurrent enhancement. However, the IPCE values decrease when the wavelength is longer than 700 nm (out of LSPR band). The reason is that it is difficult for the structures to utilize the absorbed light 100 % and the IPCE values cannot completely correspond to the absorption spectra because there are three factors to determine the IPCE values of the structures: the intensity of light absorption, the efficiency of surface charge separation, and the efficiency of charge transfer to the surface. Additionally, the IPCE values relate to the energy of incident photons. For example, with 700 nm illumination, the energy of the incident photons is relatively low, thereby most of the electrons cannot overcome the Schottky barrier to transfer to the conduction band of TiO₂ and participate reactions. Furthermore, as shown in Figure 2.7b, the average IPCE values at 500 nm ~ 900 nm increase with larger Au-NPs. Nevertheless, considering the economical reason, 12 nm Au-NPs size is preferable since the average IPCE value is almost the same as that of the 18 nm Au-NPs. Therefore, 12 nm Au-NP size is selected in the future studies.

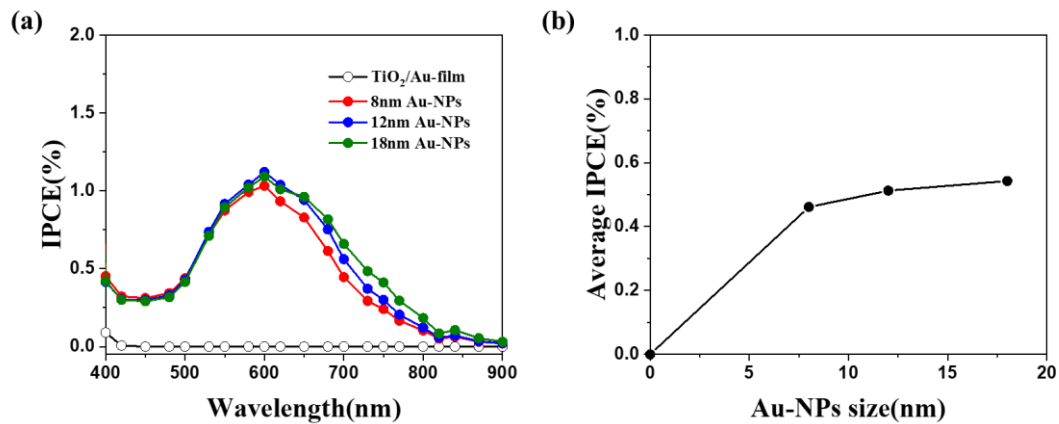


Figure 2.7 (a) IPCE spectra of ATA photoelectrodes with different Au-NP size. (b) The corresponding average IPCE obtained from 500 nm to 900 nm.

2.3.2 Dependence on inlaid depth of Au-NPs

(1) Morphologies of Au-NPs with 7 nm inlaid depth

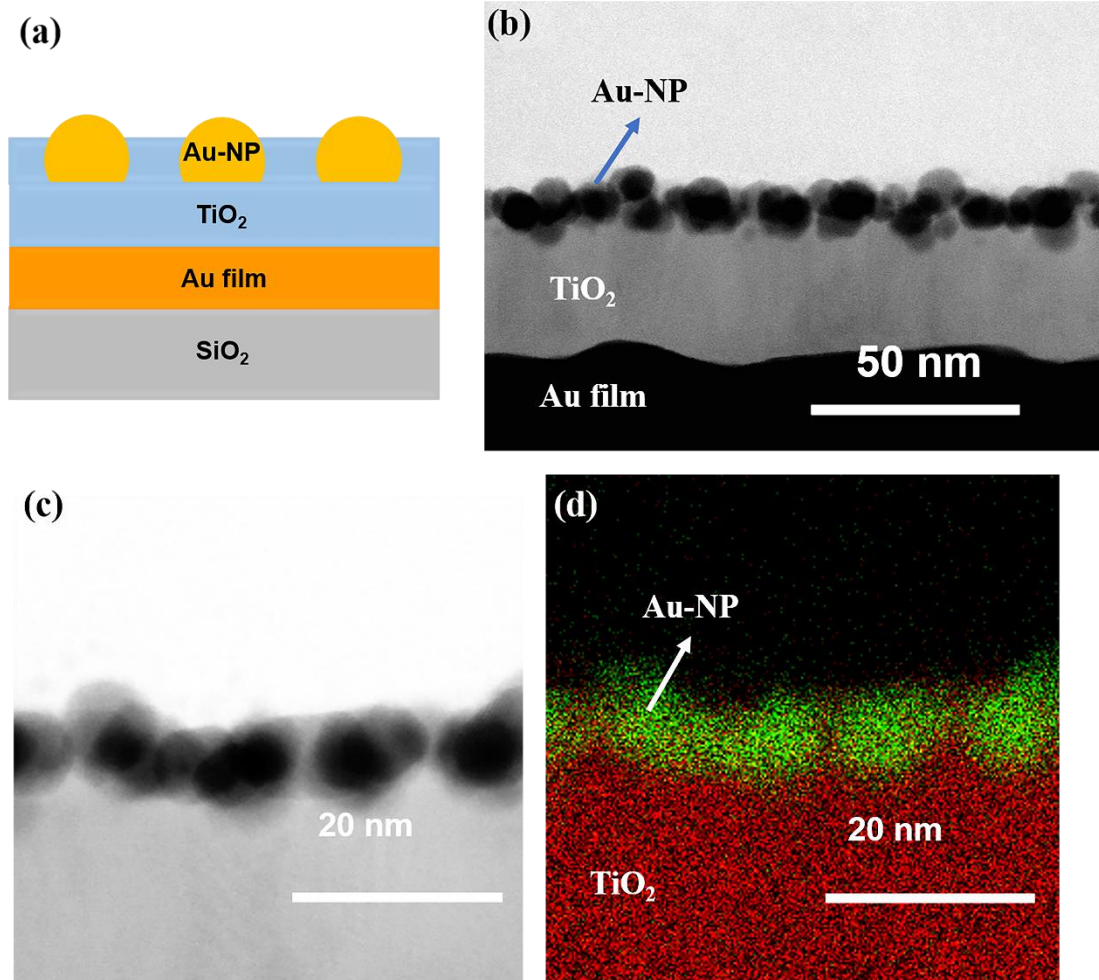


Figure 2.8 (a) Schematic and (b) side-view STEM image of partially inlaid ATA structure. (c) STEM image with high magnification corresponding to (b). (d) EDX mapping corresponding to (c).

Figure 2.8a displays the schematic of the ATA structure with partially embedded Au-NPs. At the bottom of the structure is 100 nm Au thick film. 28 nm TiO₂ thin film is on the top of the Au film. A layer of well dispersed Au-NPs is partially embedded in the TiO₂ film. This three-layered plasmonic strong coupling structure can be utilized as optical elements to collect light and/or photoelectrodes to convert light to energy. To observe the presence of partially embedded Au-NPs, a typical scanning transmission electron microscope (STEM) is used to scan the cross-sectional morphology of Au-NPs (Figure 2.8b and 2.8c). Figure 2.8d is the energy-dispersive X-ray spectroscopy (EDX) mapping corresponding to Figure 2.8c. It is clearly observed that Au-NPs are partially

embedded into TiO₂. The embedding depth is about 7 nm.

(2) Optical properties

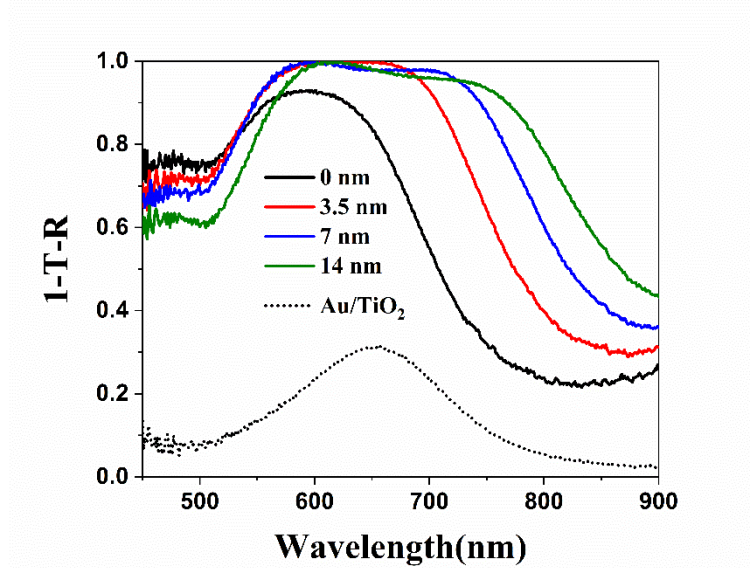


Figure 2.8 Absorption spectra, calculated by $1-T-R$, of the ATA structures with different Au-NPs embedded depth.

For the sake of elucidating the effect of partially embedded Au-NPs on the strong coupling, absorption spectra of ATA structures with different embedded depths are measured and plotted into Figure 2.8. The LSPR band of 7 nm partially embedded Au-NPs obtained from Au-NPs/TiO₂/ITO. As shown in Figure 2.8, the LSPR bands tend to separate into two peaks with increasing the embedded depth of Au-NPs. With increasing the partially embedded depth of Au-NPs, interestingly, the absorption bandwidth of the ATA structure augmented. Dual-band absorption spectra obviously appear with the embedded depth larger than 7 nm. Moreover, as illustrated for the ATA structure with 7 nm embedded Au-NPs, more than 99% of the light are absorbed in the visible light region.

2.3.3 Charge separation under modal strong coupling condition

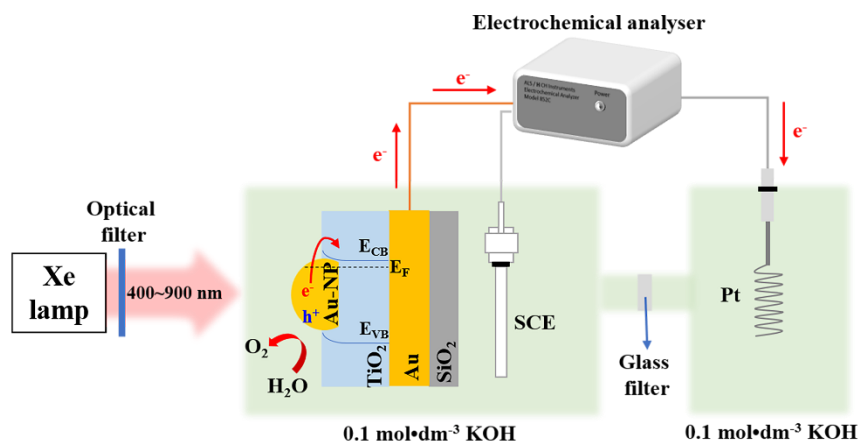


Figure 2.9 Schematic of energy level diagrams of ATA photoelectrode and the redox potential of water oxidation. E_{CB} and E_{VB} refer to conduction band and valence band energy of TiO_2 . E_F is the Fermi level of Au and TiO_2 .

Figure 2.9 illustrates the possible electron-hole pairs separation and transfer mechanism of ATA structure under the modal strong coupling condition. Under illumination, hot electron-hole pairs are generated at the bottom of Au-NPs which is 7 nm partially inlaid by TiO_2 thin film. The hot-electrons transfer from the Au-NPs to the conduction band of the TiO_2 and collected by Au film, and then go to the counter electrode (Pt) through outer circuit to participate reduction reactions, while the holes in the Au-NPs transfer to the surface of TiO_2 and used for oxidation of water. The overall process contributes to generating the measurable photocurrents.

2.4 Conclusions

In summary, the strong-coupling-enhanced absorption ability in ATA structures with only a monolayer of Au-NPs are developed and their charge separation mechanism are investigated. In these three-dimensional ATA structures, all the electrodes exhibit broad and intensive light absorption capacity under visible light irradiation. The photocurrent enhancement with various sizes of Au-NPs is examined. The experimental results demonstrate that Au-NPs with a size of about 12 nm possess superior properties not

only in photoelectrochemical performance but also this size is economically friendly. The investigated ATA structures can be fabricated easily. Therefore, it can be anticipated that the structures can be applied in the practical thin-film-based solar-to-energy devices.

2.5 References

- [1] L. Wu, F. Li, Y. Y. Xu, J. W. Zhang, D. Q. Zhang, G. S. Li, H. X. Li, *Appl. Catal. B: Environ.*, **2015**, *164*, 217-224.
- [2] Y. Nishijima, K. Ueno, Y. Yokota, K. Murakoshi, H. Misawa, *J. Phys. Chem. Lett.*, **2010**, *1*, 2031-2036.
- [3] K. Ueno, T. Oshikiri, Q. Sun, X. Shi, H. Misawa, *Chem. Rev.*, **2018**, *118*, 2955-2993.
- [4] X. M. Zhang, Y. L. Chen, R.-S. Liu, D. P. Tsai, *Rep. Prog. Phys.*, **2013**, *76*, 046401 (41pp).
- [5] C. Clavero, *Nat. Photonics*, **2014**, *8*, 95-103.
- [6] Y. Tian, T. Tatsuma, *J. Am. Chem. Soc.*, **2005**, *127*, 7632-7637.
- [7] X. Shi, K. Ueno, T. Oshikiri, H. Misawa, *J. Phys. Chem. C*, **2013**, *117*, 24733-24739.
- [8] S. Mubeen, J. Lee, N. Singh, S. Krämer, G. D. Stucky, M. Moskovits, *Nat. Nanotechnol.*, **2013**, *8*, 247-251.
- [9] S. Mubeen, G. Hernandez-Sosa, D. Moses, J. Lee, M. Moskovits, *Nano Lett.*, **2011**, *11*, 5548-5552.
- [10] K. L. Kelly, E. Coronado, L. L. Zhao, G. C. Schatz, *J. Phys. Chem. B*, **2003**, *107*, 668-677.
- [11] R. Takakura, T. Oshikiri, K. Ueno, X. Shi, T. Kondo, H. Masuda, H. Misawa, *Green Chem.*, **2017**, *19*, 2398-2405.
- [12] Z. Zhang, L. Zhang, M. N. Hedhili, H. Zhang, P. Wang, *Nano Lett.*, **2012**, *13*, 14-20.
- [13] Y. H. Lu, W. Dong, Z. Chen, A. Pors, Z. L. Wang, S. I. Bozhevolnyi, *Sci. Rep.*, **2016**, *6*, 30650.
- [14] C. Ng, J. J. Cadusch, S. Dligatch, A. Roberts, T. J. Davis, P. Mulvaney, D. E. Gómez, *ACS Nano*, **2016**, *10*, 4704-4711.
- [15] M. K. Hedayati, M. Javaherirahim, B. Mozooni, R. Abdelaziz, A. Tavassolizadeh, V. S. K. Chakravadhanula, V. Zaporotchenko, T. Strunkus, F. Faupel, M. Elbahri, *Adv. Mater.*, **2011**, *23*, 5410-5414.
- [16] A. Moreau, C. Ciraci, J. J. Mock, R. T. Hill, Q. Wang, B. J. Wiley, A. Chilkoti, D. R. Smith, *Nature*, **2012**, *492*, 86-89.
- [17] M. G. Nielsen, A. Pors, O. Albrechtsen, S. I. Bozhevolnyi, *Opt. Express*, **2012**, *20*, 13311-13319.
- [18] X. Shi, K. Ueno, T. Oshikiri, Q. Sun, K. Sasaki, H. Misawa, *Nat. Nanotechnol.*, **2018**, *13*, 953-958.
- [19] P. K. Jain, K. S. Lee, I. H. El-Sayed, M. A. El-Sayed, *J. Phys. Chem. B*, **2006**, *110*, 7238-7248.

Chapter 3 Efficient Hot-Electron Transfer under Modal Strong Coupling Conditions with Sacrificial Electron Donors

3.1 Introduction

According to the studies in Chapter 2, when the Fabry–Pérot nanocavity (FP-nanocavity) mode interacts with the localized surface plasmon resonance (LSPR) of Au-NPs, strong coupling brings about. Under this condition, the absorption capacities of the plasmonic nanostructures can be evidently intensified and broadened in the visible light wavelength. The generated hot-electrons can be transferred to the conduction band of the contacted semiconductor much more efficiently. Therefore, the photoelectrochemical properties such as photocurrent generation efficiency can be significantly augmented.¹ Particularly, except for the enhanced absorption capacity, the internal quantum efficiency (IQE) is also improved by the strong coupling conditions. The improvement of IQE means that the hot-electrons generated by light irradiation can be effectively utilized, which indicates that strong coupling structure can provide a novel method to conquer the drawbacks of traditional plasmonic nanocomposites. Therefore, thorough comprehension on the separation and transfer mechanism of electron-hole pairs is indispensable and challenging. However, it is very difficult to verify the separation efficiency of the net charges. Take water splitting as an example, water oxidation is occurred on the plasmonic photoanode and it is supposed to be the rate-determining step.

In this chapter, the hot-electron transfer efficiency of the strong coupling Au-NPs/TiO₂/Au-film (ATA) photoanode is investigated. The efficiency can be obtained from the calculation of the generated photocurrent by the ATA structures. In order to speed up the surface reaction, triethanolamine (TEOA) is used as sacrificial electron donor. The influence of strong coupling on the IQE when TEOA is used as electron donor is explored. The effect of the generation and consumption of hot-carriers on the Fermi level is also investigated by *in situ* spectro-electrochemical method with and

without TEOA.

3.2 Experimental section

3.2.1 Fabrication of Au-NPs/TiO₂/Au-film photoelectrodes

The fabrication procedure of Au-NPs/TiO₂/Au-film photoelectrodes is same to that of Chapter 2.

3.2.2 Characterizations

Photonic multichannel analyzer (PMA-11 (Hamamatsu Photonics)), which is equipped with an optical microscope (BX-51 (Olympus)), can measure the reflection (R) and transmission (T) spectra of the as-prepared structures. For the measurements, the numerical aperture of the objective lens was 0.5.

The surface morphology was observed by field-emission scanning electron microscopy (JSM-6700FT (JEOL)) with a maximum resolution of 1 nm at an electron accelerating voltage of 15 kV.

3.2.3 Photoelectrochemical measurement

The basic set-up for the three-electrode system is same to that of Chapter 2.

The applied potential was +0.3 V vs. SCE to scan the i-t curves. After finishing each scan of the monochromatic light, the applied potential was changed to -0.3 V vs. SCE to scan the i-t curves in dark for 10 s. The equation applied to calculate IPCE values at each wavelength was same to Eq. 2.1.

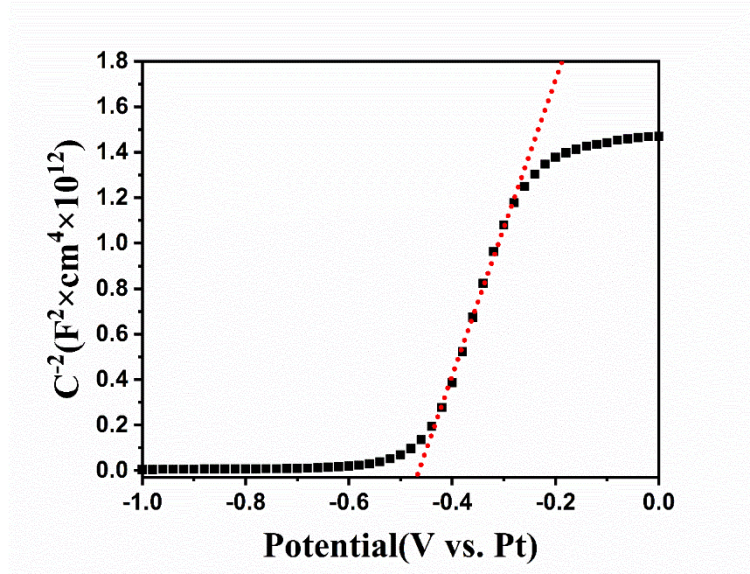


Figure 3.1 The Mott-Schottky plot of the ATA photoanode in 0.1 mol $\cdot\text{dm}^{-3}$ KOH solution with 1vol% TEOA. Frequency is 1000 Hz.

The Mott-Schottky plot was scanned by using the same three-electrode system except for the reference electrode changed to Pt. Because the capacitance C was described as Eq. (3.1), the flat-band potential was obtained from the x-intercept of the Mott-Schottky plot.¹

$$C^{-2} = \frac{2(U - U_{fb} - \frac{kT}{e})}{e\epsilon_0\epsilon_r N} \quad (3.1)$$

where U was the electrode potential, U_{fb} was the flat-band potential, k was the Boltzmann constant, T was the absolute temperature, e was the electron charge, ϵ_0 was the permittivity of the vacuum, ϵ_r was the dielectric constant, and N was the donor density).

The flat-band potential of the ATA photoanode was estimated at 298 K as -0.43 V vs. Pt from Figure 3.1 and Eq. (3.1).

3.2.4 Transient absorption decay of Au nanodisks/TiO₂

100 nm TiO₂ film was deposited on the quartz substrate by ALD. Au nanodisks were decorated on TiO₂ using the electron beam lithography (Elionix, ELS-F125) and the

lift-off methods. The thickness of Au nanodisks was 20 nm with an adhesion layer of 2 nm Ti. After the fabrication of Au nanodisks, a TEOA aqueous solution (9.1 vol%) was dropped on the Au nanodisks/TiO₂ and dried in air.

The femtosecond transient absorption spectroscopy was done by using a home-built pump-probe setup. The fundamental output from a regenerative amplified Ti:sapphire laser (Coherent, Legend Elite, λ_p : 800 nm, τ_p : 25 fs, f : 500 Hz) was split into pump and probe pulses by a 90/10 beam splitter. As a pump pulse, a collinear optical parametric amplifier (Light Conversion, TOPAS-C) was used to provide a 565 nm excitation pulse with a fluence of 30 $\mu\text{J}/\text{cm}^2$. The minor portion was focused onto a sapphire crystal to generate a white light probe pulse. Signal beams were detected on a fiber-coupled dual-channel spectrometer (Avantes, AvaSpec-ULS 2048). The Δ absorbance values of the transient absorption was obtained by the signals with and without the pump pulse.

3.2.5 *In situ* spectroelectrochemical measurement

As shown in Figure 3.2, the reflection spectra with bias voltage were obtained by utilizing the three-electrode system. The working electrode (WE) was the as-prepared ATA structure. Both the reference electrode (RE) and counter electrode (CE) were Pt sticks. The WE was prepared by pasting a layer of In-Ga alloy (4:1 weight ratio) film onto the back side of the ATA structure. Then the WE was connected to the electrochemical analyser (ALS/CH Instruments Model 760 DH) with a conductive copper wire. The electrolytes were 0.1 mol \cdot dm⁻³ KOH solutions with different concentrations of TEOA. Then, the absorption spectra with both illumination and potential were realized under 580 nm and 700 nm monochromatic light in this system.

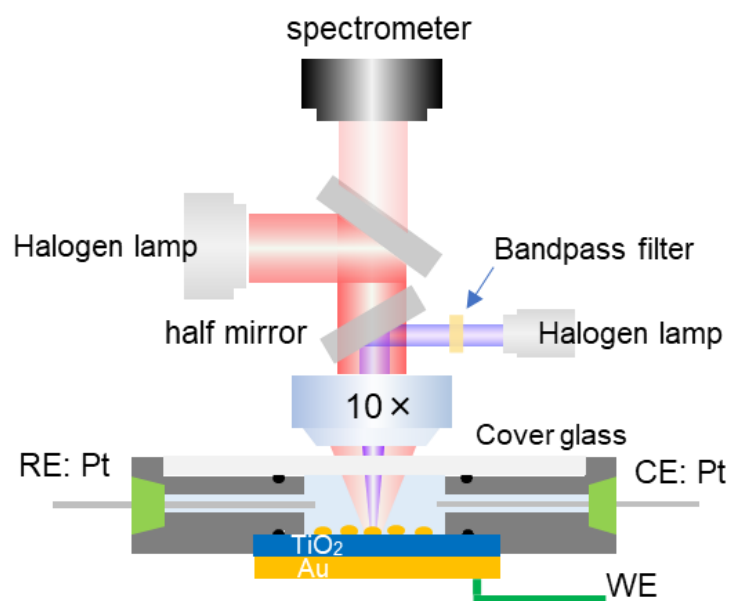


Figure 3.2 Schematic of the *in situ* spectroelectrochemical measurement.

3.3 Results and discussions

3.3.1 Dependence on concentration of electron donors

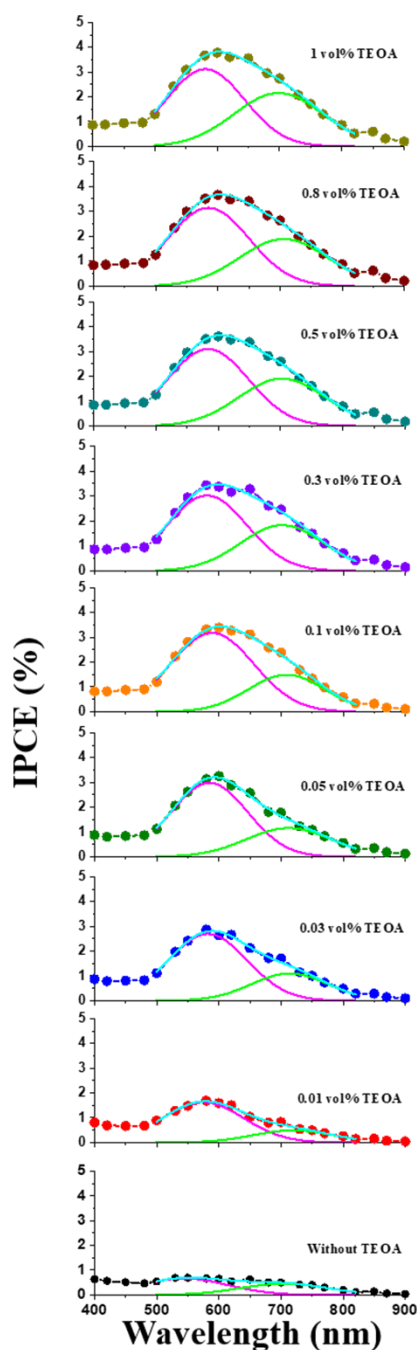


Figure 3.3 IPCE action spectra of the ATA photoanode with various TEOA concentrations: 0, 0.01 %, 0.03 %, 0.05 %, 0.1 %, 0.3 %, 0.5 %, 0.8 %, 1 vol%, respectively. The magenta and green curves are the fitting plots of the dual-bands, and the cyan curve is the sum of the dual-bands.

In order to assess the light-to-energy conversion efficiency of ATA photoanode, the three-electrode system is employed to perform the photoelectrochemical measurements. Water will act as electron donor and water oxidation occurs under the condition of the electrolyte is without any electron donor.^{2,3} TEOA is mixed in KOH electrolyte for the exploration in the effect of electron donor to the photocurrent generation of ATA structures. It is reported that the reduction ability of TEOA is relatively high and the redox potential is positive.^{4,5} Figure 3.3 is the monochromatic incident photon-to-current conversion efficiency (IPCE) of the ATA photoelectrodes with various TEOA concentrations. When the electrolyte is only KOH, the IPCE spectrum shows a wide responsivity in 500~900 nm region, which is in accordance with the wide-band absorption studied in Chapter 2. With increasing the concentration of TEOA, the IPCE values of ATA structures are improved obviously. The maximum IPCE value is about 4 %, which is about two times higher than the IPCE value of ATA without partially embedded Au-NPs due to the weak coupling intensity (Figure 3.4). Therefore, the strong coupling condition can significantly control the transfer efficiency of the hot-electrons. As the investigation in Chapter 2, the modal strong coupling condition between LSPR and FP-nanocavity can generate two hybrid modes: upper branch and lower branch. In addition, the IPCE spectra can be divided into two peaks with different TEOA concentrations. Therefore, the two hybrid branches are conducive to the transfer of hot-electrons as well as the photocurrent enhancement. The separated IPCE spectra are all plotted together with the experimental ones in Figure 3.3.

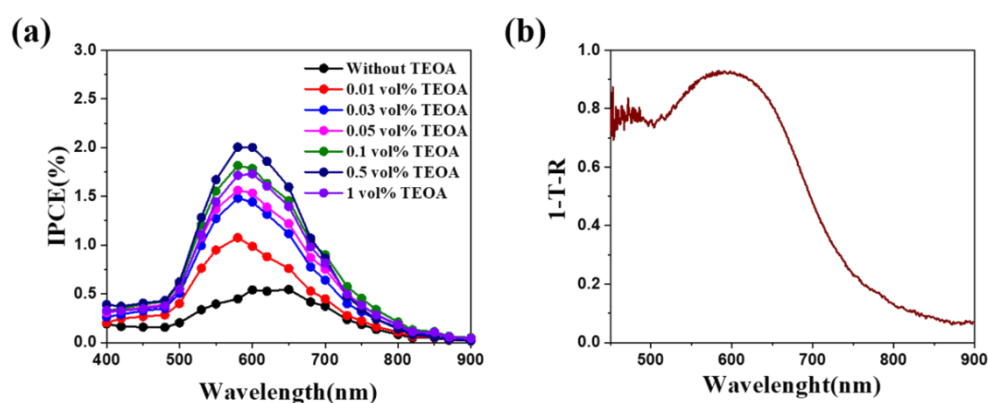


Figure 3.4 (a) IPCE spectra of ATA without partially embedded Au-NPs with different concentration of TEOA in $0.1 \text{ mol}\cdot\text{dm}^{-3}$ KOH. (b) Absorption spectrum of ATA without partially embedded Au-NPs in air.

Figure 3.5 is the IPCE increment factors for upper branch and lower branch with different concentration of TEOA. The factors are calculated by dividing the corresponded IPCE values of without TEOA. When the concentration of TEOA is lower than 0.3 vol%, both the increment factors of lower branch and upper branch are obviously determined by the concentration of TEOA. When the concentration of TEOA is higher than 0.3 vol%, the increment factors of the two branches are in equilibrium, which are not increase significantly. The value of the increment factors for the lower branch is about 4.0 and that for the upper branch is almost 4.5. What calls for special attention is that, when the concentration of TEOA is in low region, the improvement for the increment factor of upper branch is remarkably higher than that of lower branch.

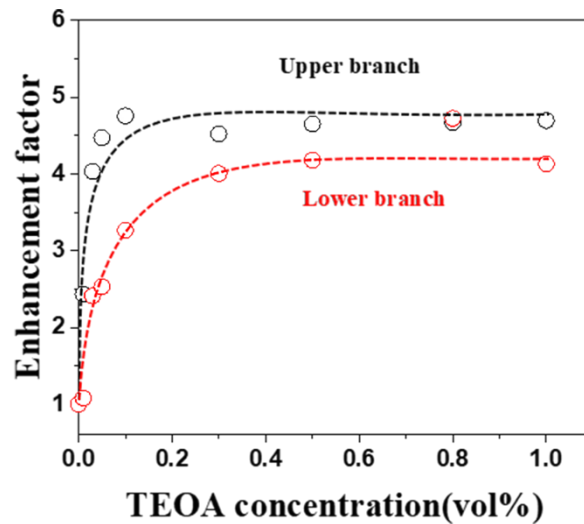


Figure 3.5 Enhancement factors obtained by dividing the IPCE peak intensity of upper branch and lower branch with TEOA by that without TEOA.

3.3.2 *In situ* optical measurement of photoelectrodes

The strong coupling condition is largely determined by the overlap among the

energy levels in each original state. In the light of the dispersion curve, when the energy of LSPR aggrandizes from the tuning condition, the energy states for both lower branch and upper branch augment, and vice versa.⁶ Besides, as is well known that the energy of LSPR is determined by refractive index. Because the refractive index strongly depends on the surrounding environment as well as the density of electrons.⁷ It is given by the following equations:

$$\lambda = \lambda_p \sqrt{\varepsilon_\infty + \left(\frac{1-L}{L}\right)\varepsilon_m} \quad (3.3)$$

$$\lambda_p = \frac{2\pi c}{\omega_p} = \sqrt{\frac{4\pi^2 c^2 m \varepsilon_0}{N e^2}} \quad (3.4)$$

where λ_p is the frequency for bulk plasma, ε_∞ is the dielectric constant of high frequency contribution, L is the particle size shape parameter, ε_m is the dielectric constant of the surrounding environment, m is the effective mass of the electron, e is the charge of the electron, N is the density of electrons, and ε_0 is the dielectric constant of vacuum. Therefore, when the density of the electrons of the metal nanoparticles reduces or ε_m increases, it tends to redshift for the absorption spectrum. For comparison, when the density of electrons become larger or ε_m become smaller, the spectrum tends to be blue-shifted.

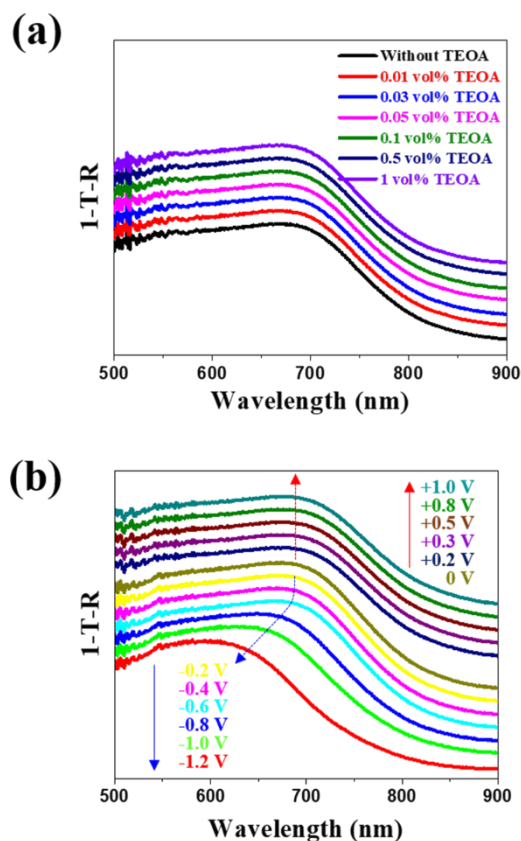


Figure 3.6 (a) Absorption spectra of ATA structures with various TEOA concentrations. The applied voltage is 0.3 V vs Pt. (b) Absorption spectra of ATA structures with different applied voltage. The concentration of TEOA is 1 vol%.

For the sake of observing differences in the absorption spectra, *in situ* spectroelectrochemical measurements are performed. Figure 3.6a is the absorption spectra of ATA structures measured in KOH solutions with different TEOA concentration. It shows that all the absorption spectra of ATA structures measured in KOH solution are similar to each other. Therefore, the concentrations of TEOA do not affect the absorption spectra of ATA structures in KOH solution. Moreover, the absorption spectra are still broad in the visible light region despite of the indistinct dual-bands, signifying the strong coupling condition is almost kept.

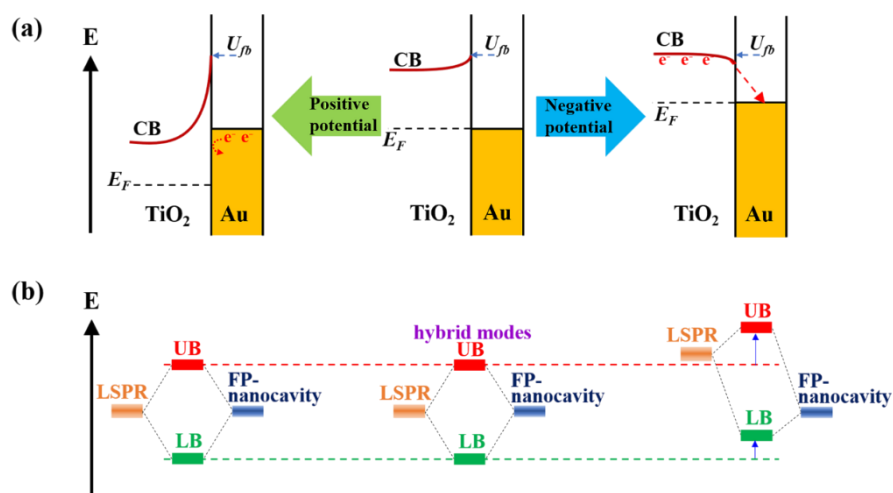


Figure 3.7 (a) Energy diagrams at the interface of Au-NPs/TiO₂. (b) Strong coupling between FP-nanocavity and LSPR with applied potential. U_{fb} is the flat-band potential.

Figure 3.6b shows the absorption dependence on the applied voltage. The absorption spectra of ATA photoanodes are almost the same even the applied potential is up to +1.0 V vs Pt. Therefore, the electron density of Au-NPs will not be changed by positive bias because the Schottky barrier at the interface prevents the electron transfer from Au-NPs to TiO₂ (Figure 3.7a). However, as shown in Figure 3.6b, the absorption spectra of ATA structure change evidently when negative bias is applied. When the applied bias is smaller than -0.4 V vs. Pt, the absorption spectra tend to shift to the smaller wavelength. This potential threshold is in accordance with the flat-band potential of the electrode shown in Figure 3.1, the value is -0.43 V vs. Pt. The reason is that when the electrons transfer from TiO₂ to Au-NPs beyond the flat-band potential, the LSPR band shifts to the blue light wavelength. Under the condition of the blue shift of LSPR, the energy states of both the upper branch and the lower branch simultaneously shift to blue due to the detuning condition between FP-nanocavity and LSPR (Figure 3.7). Moreover, it is possible that the refractive index of Au-NPs' surface changes due to the hydrogen absorption generated from water reduction. In this case, the LSPR band changes. The carriers can be transported with the applied bias and, therefore, the strong coupling condition can be tuned, which is similar to the ensemble coupling between molecular excitation and the optical mode.⁸

Moreover, the density of electrons in Au-NPs can be determined by plasmon-induced hot electron-hole pairs generation and transfer. The change of LSPR spectra with various TEOA concentrations was explored under monochromatic illumination, which can excite both the lower branch and the upper branch (Figure 3.8). The upper branch can be excited at 580 nm monochromatic light, while the lower branch can be excited under illumination of 730 nm light. As shown in Figure 3.8a, without TEOA, the absorption spectrum shifts to longer wavelength under illumination, in which the upper branch exhibits larger shift than the lower branch. The reason for the redshift of the spectrum is that the density of electrons reduces or the holes increase. Some hot-holes can participate in water oxidation reaction; however, some might lose their energy resulting in the positively shift of the Fermi level of Au-NPs. In addition, under excitation of 580 nm monochromatic light, more hot-holes are generated thereby resulting in a larger positive shift of Fermi level. The potential for water oxidation reaction is still positive compared to the energy of the Fermi level in Au-NPs obtained from the spectrum shift. As shown in Figure 3.8b, after adding 0.01 vol% of TEOA in KOH, there is no redshift for the spectrum under the illumination of 580 nm. The reason is that most of the hot-holes originated from the excitation of upper branch participate the oxidation. As shown in Figure 3.8c, when the concentration of TEOA increased to 1 vol%, there was no any shift in the absorption spectra. In this case, both the excitation of upper branch and lower branch cannot affect the Fermi level.

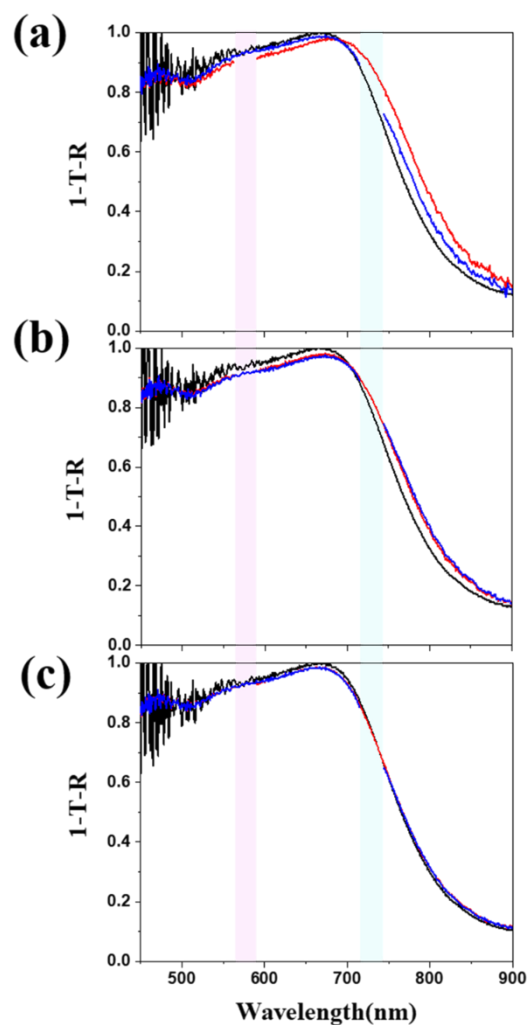


Figure 3.8 Absorption spectra of ATA structures with different concentration of TEOA: (a) 0 vol%, (b) 0.01 vol%, and (c) 1 vol%. The applied voltage is +0.3 V vs Pt. Black curves are absorption spectra without monochromatic light. Red curves are absorption spectra under 580 nm light irradiation. Blue curves are absorption spectra under 730 nm light irradiation. The unconnected parts of red and blue spectra are in accordance with the illumination light, and the wavelength of 580 nm and 730 nm are displayed in pink and cyan.

3.3.3 Plasmon-induced hot-electron transfer

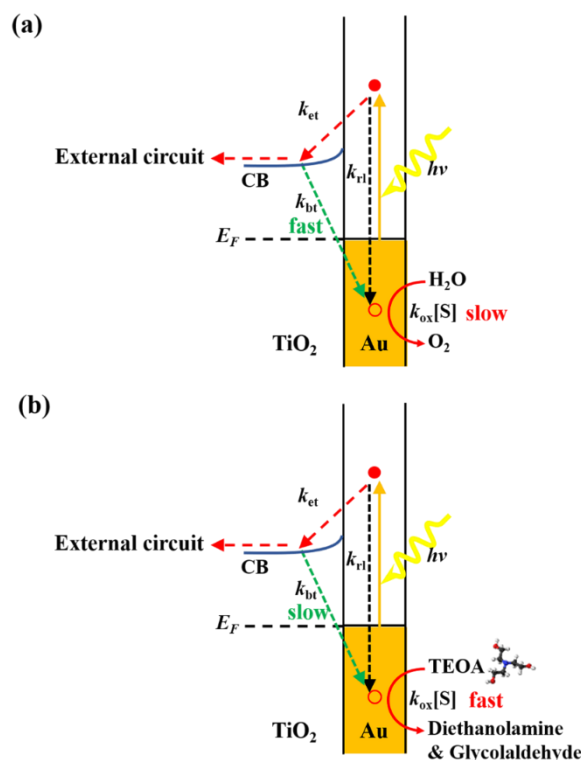


Figure 3.9 Schematic illustrations of plasmon-induced hot-electron transfer and oxidation reaction (a) without and (b) with TEOA in electrolyte. k_{et} is the constant of hot-electron transfer. k_{bt} is the constant of back-electron transfer. k_{rl} is the constant of hot-electron relaxation. and k_{ox} is the constant of oxidation reaction. $[S]$ is the concentration of the substance. CB is the conduction band of TiO₂. E_F is the energy of the Fermi level.

The mechanism of plasmon-induced hot-electron transfer and the water oxidation reaction are illustrated in Figure 3.9.² Under excitation, the plasmonic Au-NPs generate hot electron-hole pairs. The hot-electrons are injected into the conduction band of the TiO₂; while the highly reacted holes transfer to the surface states of TiO₂ near Au-NPs and then participate in the oxidation of substances. The transfer efficiency of plasmon-induced hot-electrons is determined by several parameters. After excitation, the hot-electrons can be relaxed via electron-electron scattering.⁹ Besides, the hot-electrons which have already been injected into the conduction band of TiO₂ may return to Au-

NPs and recombine with the holes. Since the oxidation reaction is much slower than the recombination of electron-hole pairs, it is difficult to suppress this relaxation process through the consumption of holes. However, it is relatively slow for the transfer of the back-electrons, and this transfer efficiency can be significantly reduced by speeding up the reaction of holes. Thus, it is necessary to smoothly supply electrons from the reactants to diminish the effect of back-electron transfer as well as to evaluate the efficiency of hot-electron transfer. Actually, the transient absorption results of Au-NPs/TiO₂ demonstrates that the decay of the transferred hot-electrons can be prolonged via the addition of TEOA (Figure 3.10).

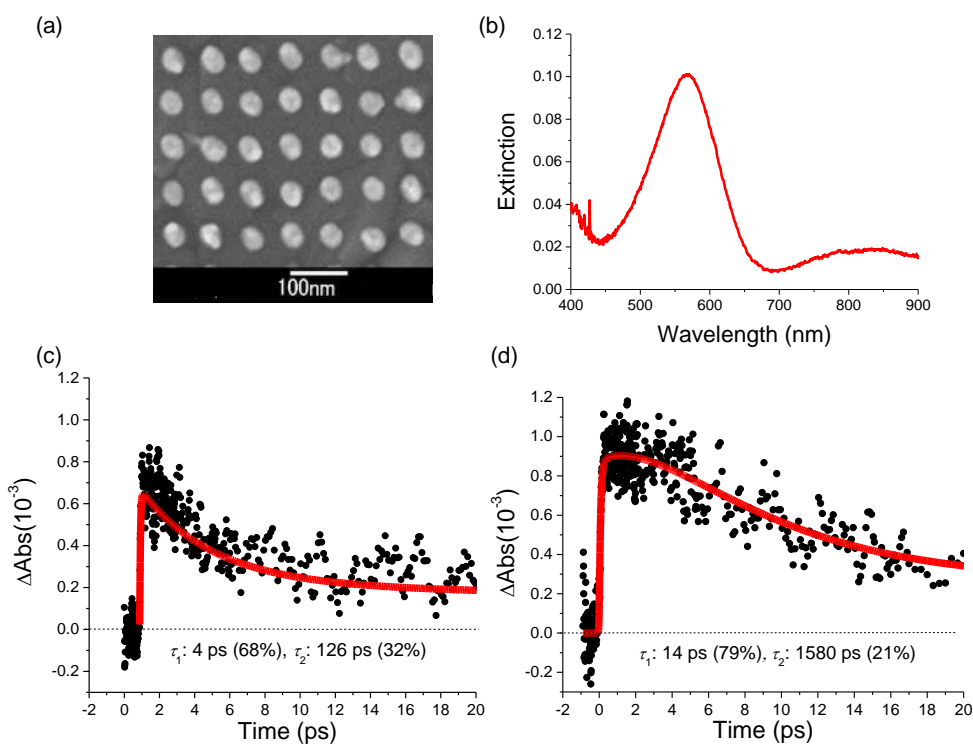


Figure 3.10 (a) SEM image of Au nanodisks on TiO₂. (b) Extinction spectrum of Au nanodisks on TiO₂. (c,d) Decay curves of Δ absorbance at a 950 nm wavelength measured on the Au-nanodisks/TiO₂ without (c) and with (d) TEOA. The excitation wavelength (pump pulse) is a 565 nm wavelength.

It is speculated that the oxidation rate ($k_{ox}[S]$) relating to the consumption of holes is crucial to these phenomena. Generally, hot-holes with excessive energy can enhance the constant of surface oxidation rate (k_{ox}). In addition, it has been calculated that the

energy distribution of plasmon-induced hot electron-hole pairs can be decided by the excitation energy of LSPR.¹⁰ Under the condition of no electron donor, the hot-holes might be trapped at the surface state of TiO₂ before taking part in water oxidation. Therefore, the differentiate of the energy in upper branch and lower branch cannot principally determine the reaction rate of water oxidation. The oxidation process of TEOA is a one-electron reaction.¹¹ Therefore, highly energetic hot-holes from the upper branch excitation can oxidize TEOA efficiently. Under the circumstance of low TEOA concentration, the oxidation rate is mainly determined by the rate constants based on the excitation of upper branch and lower branch. However, when the TEOA concentration is relatively high, the oxidation rate is high enough for both hybrid modes. Because the excitation energy can also affect the energy distribution of plasmon-induced hot-electrons, when the concentration of TEOA is high, the difference of the electron transfer efficiency between the upper branch and the lower branch can be determined by the small differentiation of enhancement factors.

3.3.4 Hot-electron transfer efficiency

The effect of plasmon-induced hot-electrons produced by ATA photoelectrodes to electron transfer is investigated. The IQE values are calculated from IPCE/absorption. Figure 3.11a shows the IQE of ATA photoelectrodes with different TEOA concentration. With increasing the concentration of TEOA, the IQE values are improved. For lower TEOA concentration, the increments of IQE for both upper branch and lower branch are more obvious than the corresponded IPCE values. Under the high TEOA concentration, the IQE value at 600 nm is 3.8 %, and the value at 770 nm is 2.7 %. It is because the two branches can facilitate the generation and transfer of the plasmon-induced hot-electrons.

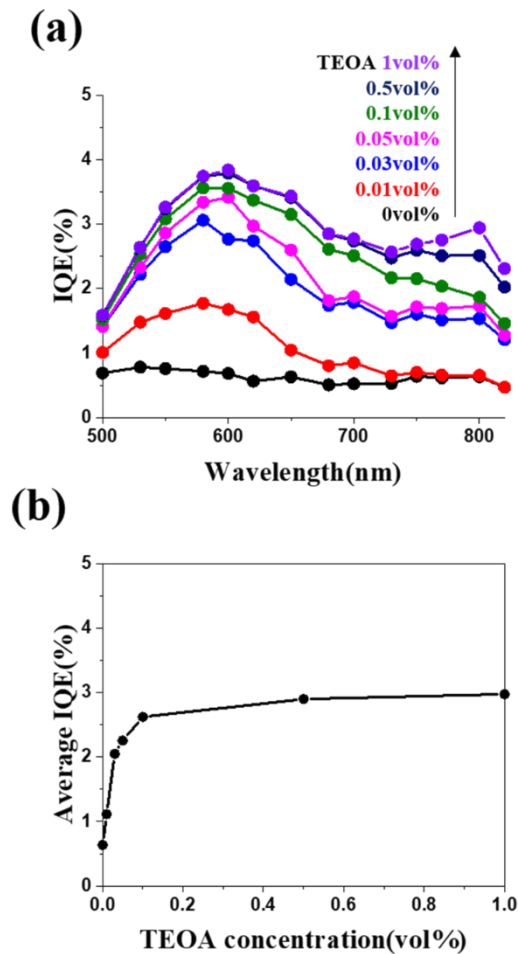


Figure 3.11 IQE spectra of ATA photoelectrode with various TEOA concentrations in 100 mL $0.1 \text{ mol} \cdot \text{dm}^{-3}$ KOH. (b) Average IQE from 500 nm to 800 nm corresponding to (a).

Figure 3.11b displays the average IQE from 500 to 800 nm. When the TEOA concentration is up to 1 vol%, the average of IQE is about 5 times higher than that in the plain KOH electrolyte. The value is about 3%. Since about 40 % solar energy is in 500~800 nm, this high IQE values are promising for the utilization in solar-to-energy conversion devices.

3.4 Conclusions

In conclusion, via observing and calculating the photocurrent generated by the ATA photoelectrode with electron donors, the transfer efficiency of plasmon-induced hot-

electrons under the strong coupling between nanocavity and LSPR is studied. With the addition of TEOA, back-electron transfer can be effectively suppressed and the consumption of hot-holes is significantly accelerated. The highest PCE value of the upper branch is improved about 4.5 times, and the highest IPCE value of the lower branch increases about 4.0 times. Moreover, with the addition of TEOA, the average IQE in 500~800 nm region is about 3 %. It is proved that both the upper branch and the lower branch devote to the generation and transfer of the hot-electrons.

3.5 References

- [1] L. Kavan, M. Grätzel, S. E. Gilbert, C. Klemenz, H. J. Scheel, *J. Am. Chem. Soc.*, **1996**, *118*, 6716-6723.
- [2] Y. Nishijima, K. Ueno, Y. Kotake, K. Murakoshi, H. Inoue, H. Misawa, *J. Phys. Chem. Lett.*, **2012**, *3*, 1248-1252.
- [3] X. Shi, K. Ueno, N. Takabayashi, H. Misawa, *J. Phys. Chem. C*, **2013**, *117*, 2494-2499.
- [4] Y. Yamazaki, H. Takeda, O. Ishitani, *J. Photochem. Photobiol. C: Photochem. Rev.*, **2015**, *25*, 106-137.
- [5] K. Kalyanasundaram, *J. Chem. Soc. Faraday Trans. 2*, **1986**, *82*, 2401-2415.
- [6] X. Shi, K. Ueno, T. Oshikiri, Q. Sun, K. Sasaki, H. Misawa, *Nat. Nanotechnol.*, **2018**, *13*, 953-958.
- [7] C. Novo, A. M. Funston, A. K. Gooding, P. Mulvaney, *J. Am. Chem. Soc.*, **2009**, *131*(41), 14664-14666.
- [8] F. Kato, H. Minamimoto, F. Nagasawa, Y. S. Yamamoto, T. Itoh, K. Murakoshi, *ACS Photonics*, **2018**, *5*, 788-796.
- [9] D. C. Ratchford, A. D. Dunkelberger, I. Vurgaftman, J. C. Owrutsky, P. E. Pehrsson, *Nano Lett.*, **2017**, *17*, 6047-6055.
- [10] R. Sundararaman, P. Narang, A. S. Jermyn, W. A. Goddard Iii, H. A. Atwater, *Nat. Commun.*, **2014**, *5*, 5788.
- [11] C. Kotal, M. A. Weber, G. Ferraudi, D. Geiger, *Organometallics*, **1985**, *4*(12), 2161-2166.

Chapter 4 Near-Field Engineering for Boosting the Photoelectrochemical Activity to a Modal Strong Coupling Structure

4.1 Introduction

Intensified near-field is considered as one of the most significant features in noble metal nanostructures via the excitation of localized surface plasmon resonance (LSPR).¹⁻⁵ The strong near-field has been extensively verified to play an important part in plasmon-induced chemical reactions.⁶⁻¹⁰ It is well known that the plasmon-induced hot-electron transfer can improve the visible light absorption and utilization of metal/n-type semiconductor nanocomposites.¹¹⁻¹⁵ Via the excitation of LSPR, hot-electrons are generated and subsequently transfer to the conduction band of the contacted semiconductor; while the holes are trapped in the surface state of the semiconductor and then take part in the oxidizing reaction.^{16,17} Since the localized electric field of the plasmonic metal nanostructure can prominently determine the generation of the plasmon-induced hot-electrons,^{18,19} it is considerably meaningful to selectively modulate the localized electrical field around the noble metal nanostructures for photocatalytic application because of the critical role of hot-electrons.^{20,21}

Till now, numerous researches have focalized in assessing the optical performances of Au-NP/TiO₂ systems ascribing to their distinct advantages, for example, plasmon-induced photocurrent increment as well as the enhanced photocatalytic efficiencies under visible light irradiation.²²⁻²⁴ According to the investigation of the former Chapters and the published results, the strong coupling structure of Au-NPs/TiO₂/Au-film (ATA) possesses improved solar-to-energy conversion efficiency and water oxidation rate.²⁵ For the ATA structure, about 7 nm Au-NPs are embedded into the TiO₂ film in order to improve the interaction of Au-NPs (LSPR mode) and TiO₂ (nanocavity mode). From the simulation results by finite element method (FEM), the strong near-field is generated at the bottom of the partially embedded Au-NPs, which indicates that the plasmon-induced hot electron-hole pairs are generated and separated at the bottom of

the embedded Au-NPs located in the TiO₂. However, the hot-holes need to transfer to the surface of TiO₂ to participate in the water oxidation. In this configuration, the transfer of holes has negative influence in photochemical reactions due to the unavoidable recombination with hot-electrons. Therefore, in order to improve the water oxidation efficiency of ATA structure, a near-field engineering technique is urgently needed to establish an intensified near-field close to the interface of the three-phase boundary in solution, TiO₂ and Au-NPs.

Morphology regulation is supposed to be an effective direction to manipulate the spatial distribution of the near-field in plasmonic noble metal nanostructures.^{26,27} Therefore, in this chapter, an engineered ATA structure, denoted as Au@ATA is investigated. In Au@ATA structure, Au is electrochemically postdeposited on the original Au-NPs of ATA structure. It is considered that the postdeposited Au generated via the electrochemical method will create a new interface between TiO₂ and the postdeposited Au. This brand-new interface is deemed to indispensable for improving the photoelectrochemical activities. The influence of reaction time of electrochemically postdeposited Au on the morphologies of Au-NPs, the light absorption properties, the strong coupling condition of ATA structure, as well as the photoelectrochemical performances are investigated.

4.2 Experimental section

4.2.1 Fabrication of Au@Au-NPs/TiO₂/Au-film photoelectrodes

The preparation process of Au@Au-NPs/TiO₂/Au-film structures is described in section 2.2.1 of Chapter 2.

Au was electrochemically postdeposited on ATA using a three-electrode system, with the ATA structure as the working electrode (WE), a platinum wire as the counter electrode (CE) and a saturated calomel electrode (SCE) as the reference electrode (RE). For the preparation of the WE, an In-Ga alloy (4:1 weight ratio) film was pasted onto the back and side of the structure, which was then connected to an electrochemical

analyser (ALS/CH Instruments Model 852C) with a copper lead wire. The $0.25 \text{ mmol}\cdot\text{dm}^{-3}$ HAuCl_4 with $0.1 \text{ mol}\cdot\text{dm}^{-3}$ Na_2SO_4 was used as the Au precursor, in which Na_2SO_4 worked as a stabilizer and electrolyte. A +0.3 V bias was applied during the electrochemical deposition. The electrochemical reaction was performed for 1, 3 and 8 min. Finally, the as-prepared structure was rinsed with deionized water and dried with a pure nitrogen flow.

4.2.2 Characterizations

The reflection and transmission spectra were obtained by a photonic multichannel analyzer (PMA-11 (Hamamatsu Photonics)) equipped with an optical microscope (BX-51 (Olympus)). The numerical aperture of the objective lens used for the measurements was 0.5.

The surface morphology was observed by ultra-high-resolution scanning electron microscope (SU8230 (HITACHI)) with a maximum resolution of 0.8 nm at an electron accelerating voltage of 15 kV.

The cross-section was analyzed by high-resolution transmission electron microscopy (JEOL ARM (200 F) 200 kV FEG-STEM/TEM) with a resolution of 75 pm at an electron accelerating voltage of 200 kV.

4.2.3 Numerical simulations

Full-field electromagnetic wave simulations were performed by using the finite-element method (FEM) (COMSOL Multiphysics[®]) for the Au-NP/TiO₂/Au-film (ATA) structure and Au@Au-NP/TiO₂/Au-film (Au@ATA) structure. The refractive index of gold was based on the data from Johnson and Christy.²⁸ The TiO₂ thin film was assumed to behave as a dielectric with an effective refractive index of $n = 2.4$. The background was water with the refractive index of $n = 1.33$. A unit cell of investigated structures was simulated using periodic boundary conditions in x- and y-directions and perfectly matched layers in z-direction. Circularly polarized plane waves with the wavelength of 650 nm were used to excite the structure along the z direction. The finest mesh size was

0.2 nm. An ellipsoid sphere with a diameter of 12 nm in the x and y directions and 10 nm in the z direction was used to model the Au-NP. The size of post-deposited Au-cap was 1.3 times of Au-NP. The period was 20 nm. The Au-NP/TiO₂ interface was formed by truncating Au NPs by TiO₂.

4.2.4 Photoelectrochemical measurement

The setup for photoelectrochemical measurement and the equation for the calculation of monochromatic incident photon-to-electron conversion efficiency (IPCE) are described in section 2.2.3 of Chapter 2.

4.3 Results and discussions

4.3.1 Finite element method (FEM) simulation

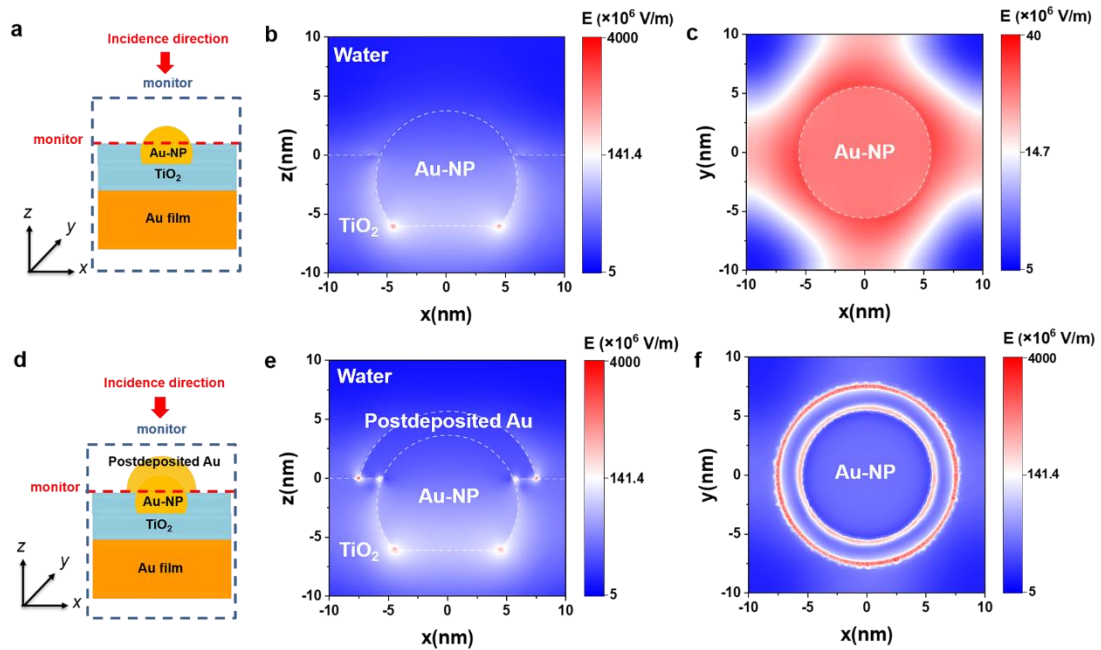


Figure 4.1 Near-field distribution under 650 nm irradiation calculated using an FEM simulation. Two near-field profile monitors were set in the xz - and xy -planes to visualize the near-field intensity, as shown by the blue and red dashed lines. (a) Simulation model, (b) side view (xz -plane), obtained by magnifying part of (a), (c) top view (xy -plane) of ATA structures; (d) simulation model, (e) side view (xz -plane), obtained by magnifying

part of (d), (f) top view (xy -plane) of Au@ATA. The simulations were performed with a circularly polarized plane-wave light source in water.

Firstly, FEM simulations for ATA structure and the ideal configurations of Au@ATA structure are executed to realize the design of the intensified near-field distributions on ATA structure. Figure 4.1 displays the near-field distributions at 650 nm in xz -plane and xy -plane of ATA structure and Au@ATA structure. The simulations are carried out via the commercial finite element solver (COMSOL Multiphysics[®]). E is the amplitude of the electric field amplitude. For the electric field distribution of ATA structure as illustrated in Figures 4.1b and 4.1c, the relatively intensified near-fields only locate in the bottom part of Au-NPs, namely the interface of Au-NP/TiO₂ embedded in TiO₂ film. For the Au@ATA structure, however, except for the intensified near-field at the bottom of Au-NPs, a significant strong near-field locating in the boundary of postdeposited Au/TiO₂ is generated, as shown in Figure 4.1e. In addition, Figure 4.1f further proves the distinct strong near-field at the interface of postdeposited Au and TiO₂. It should be noted that the maximum scale bar of Figure 4.1f is two orders of magnitude larger than that of Figure 4.1c in order to get a better comparison.

In addition to the ideal simulation model of Au@ATA, the simulations for the near-field distributions for other configurations of postdeposited Au are also carried out. The simulation models and results are summarized in Figure 4.2. According to the simulation results as shown in Figure 4.2b, 4.2c, 4.2e, 4.2f, when the new interfaces are generated between the postdeposited Au and TiO₂, the near-field close to the three-phase boundary in postdeposited Au, TiO₂ and water can be adjusted effectively. However, when the postdeposited Au locates on the top of the original Au-NPs and is not in contact with TiO₂, there is no obvious change in the near-field distribution (Figure 4.2h and 4.2i). Therefore, it can be expected that the intensified near-field at the interface of the postdeposited Au and TiO₂ can contribute to the increment of the photochemical reaction efficiency.

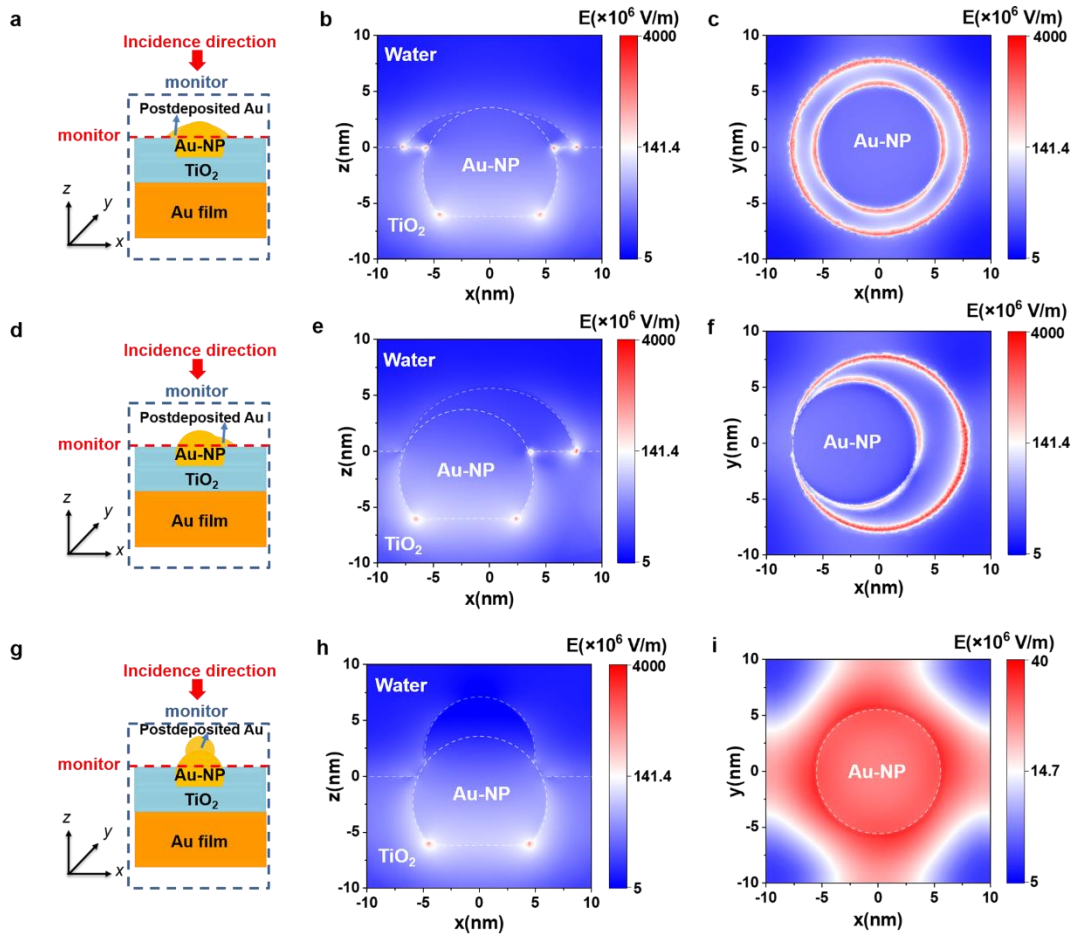


Figure 4.2 Near-field distribution under 650 nm irradiation calculated using an FEM simulation. Two near-field profile monitors were set in the xz - and xy -planes to visualize the near-field intensity, as shown by the blue and red dashed lines. (a) simulation model, (b) side view (xz -plane), obtained by magnifying part of (a), (c) top view (xy -plane) of Au@ATA with the postdeposited Au locating around the original Au-NP; (d) simulation model, (e) side view (xz -plane), obtained by magnifying part of (d), (f) top view (xy -plane) of Au@ATA with the postdeposited Au locating at one side of the original Au-NP; (h) simulation model, (i) side view (xz -plane), obtained by magnifying part of (h), (i) top view (xy -plane) of Au@ATA with the postdeposited Au locating at the top of the original Au-NP. The simulations were performed with a circularly polarized plane-wave light source in water.

4.3.2 Constant potential electrolysis (CPE) process

Based on the aforementioned simulation results, a facile constant potential electrolysis (CPE) method is applied to realize the postdeposition of Au on the original Au-NPs of ATA electrode (Figure 4.3).²⁹ Au is electrochemically postdeposited in a typical three-electrode system. The reaction setup is same to Figure 2.2 in Chapter 2. The electrolyte is $0.1 \text{ mol}\cdot\text{dm}^{-3}$ Na_2SO_4 aqueous solution containing $0.25 \text{ mmol}\cdot\text{dm}^{-3}$ HAuCl_4 (hydrogen tetrachloroaurate (III) tetrahydrate).

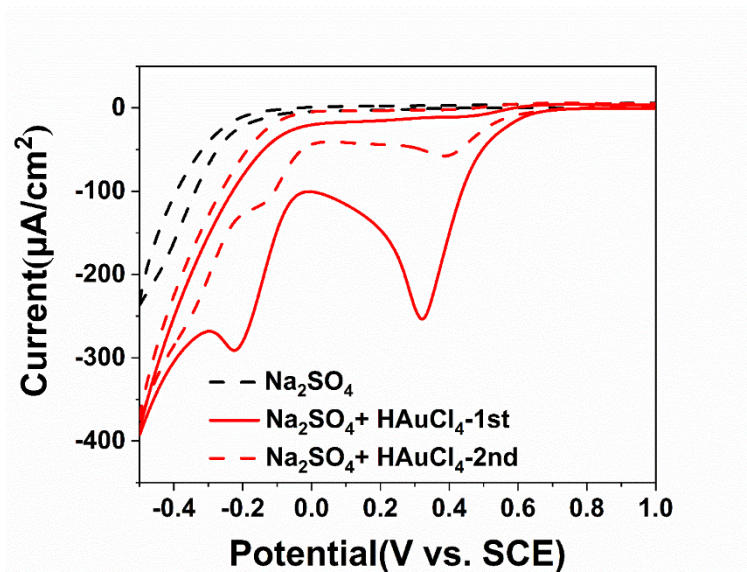


Figure 4.3 Cyclic voltammogram (CV) curves recorded on ATA electrode in $0.1 \text{ mol}\cdot\text{dm}^{-3}$ Na_2SO_4 solution containing $0.25 \text{ mmol}\cdot\text{dm}^{-3}$ HAuCl_4 , red solid and red dash line are first and second scan, respectively; black dash line is CV recorded under the same conditions in the absence of HAuCl_4 . Scan direction: from positive potential to negative potential. Scan rate: $0.01 \text{ mV}\cdot\text{s}^{-1}$.

Cyclic voltammogram (CV) curves are scanned from 1.0 V to -0.5 V to determine the reaction potential of AuCl_4^- reduced to postdeposited Au particle, as shown in Figure 4.3. In the precursor solution of $0.25 \text{ mmol}\cdot\text{dm}^{-3}$ HAuCl_4 and $0.1 \text{ mol}\cdot\text{dm}^{-3}$ Na_2SO_4 , Na_2SO_4 is considered as a supporting electrolyte in order to improve the conductivity of the aqueous solution as well as avoid aggregation of electrochemical reduced Au. The CV curves are scanned firstly from positive potential to the negative potential. As

displayed in Figure 4.3, the red solid line is the first positive to negative forward scan. The reduction peak locates at +0.32 V vs SCE. In contrast, there is no peak +0.32 V vs SCE when the scan is performed in the electrolyte with only $0.1 \text{ mol}\cdot\text{dm}^{-3} \text{ Na}_2\text{SO}_4$. This potential is considered as the electrochemically reduction of Au^{3+} onto the ATA electrode. As is well-known that the formation of Au metal on the surface of the electrode relates to a three-electron reduction process of Au^{3+} .²⁹ The related equation can be expressed as following:



However, this reduction peak shifts to more positive potential for the second positive to negative scan process, the red dash line as shown in Figure 4.3. The reason is that it is much easier for the newly generated Au depositing on the already formed Au than the nucleation of new Au cores on the ATA structure. According to the previous reports, high over-potential is supposed to improve the nucleation rate via improving the Gibbs free energy for generation of the new nuclei.²⁹ Therefore, the surface morphology of the structure can largely depend on the applied potential in the electrodeposition process. Consequently, in this study, +0.3 V vs. SCE is used as the applied potential for electrochemically postdepositing Au on ATA structure.

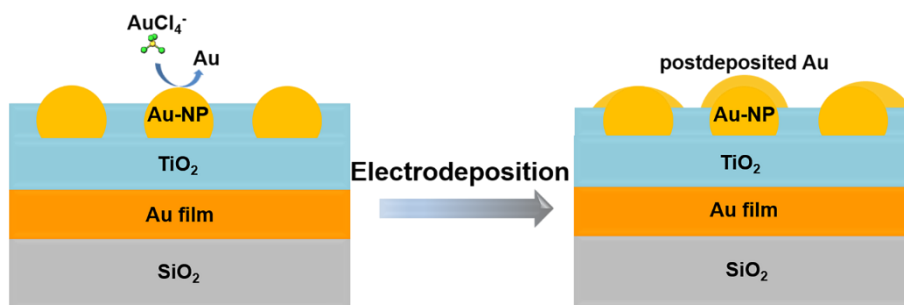


Figure 4.4 Schematic process for electrochemically postdepositing Au on ATA electrode (Au@ATA).

According to heterogeneous nucleation theory, the original Au-NPs on ATA structure can work as active centres to decrease the free energy of Au nucleating from the precursor solution,³⁰ and Au prefers to postdeposit on the original Au-NPs. As illustrated in Figure 4.4, Au is postdeposited on ATA electrode via the CPE technique.

During the Au electrodeposition process, the concentration of AuCl_4^- shows a difference in the reaction solution. In other words, the concentration of AuCl_4^- near the charged Au-NPs surface of ATA electrode is lower than that away from Au-NPs.³¹

4.3.3 Morphologies of the prepared photoelectrodes

Figure 4.5a and 4.5b are the SEM images of the surface morphologies of ATA before and after partially embedding Au-NPs. As shown in Figure 4.5a and 4.5c, before partially embedding the Au-NPs, the average size of Au-NPs is about 10 ± 6.7 nm. Figure 4.5b shows the surface morphology of ATA structure with 7 nm embedded Au-NPs.

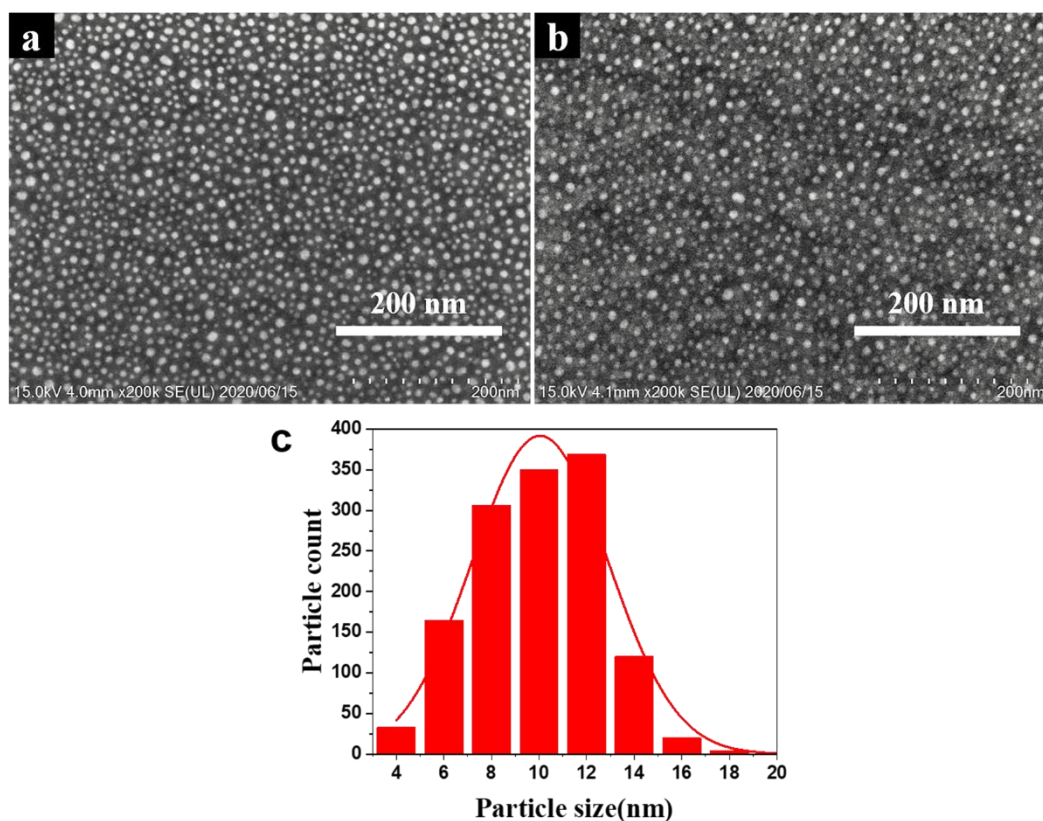


Figure 4.5 (a) SEM image of ATA structures without partially embedding Au-NPs. (b) SEM image of ATA with 7 nm embedded Au-NPs. (c) Size distribution of the Au-NPs by analyzing (a). The red line is plotted by Gaussian fitting.

The surface morphologies and Au-NPs size distributions with different

electrochemically deposition time are summarized in Figure 4.6. With prolonging the deposition time, the Au-NPs become larger, which indicates that Au is successfully postdeposited on the original Au-NPs of ATA structure via the CPE method. To further analyze the influence of the postdeposited Au on the total particle number of Au-NPs, SEM images with same area are selected. The selected area of the SEM images is 639 nm × 479 nm (Figure 4.5a, 4.6a, 4.6c, 4.6e). As a result, there are 1367 Au-NPs for ATA (Figure 4.5a) in the selected SEM image and 1023, 951, 618 Au-NPs for Au@ATA with the electrochemical deposition time of 1 min, 3 min and 8 min (Figure 4.6a, 4.6c and 4.6e).

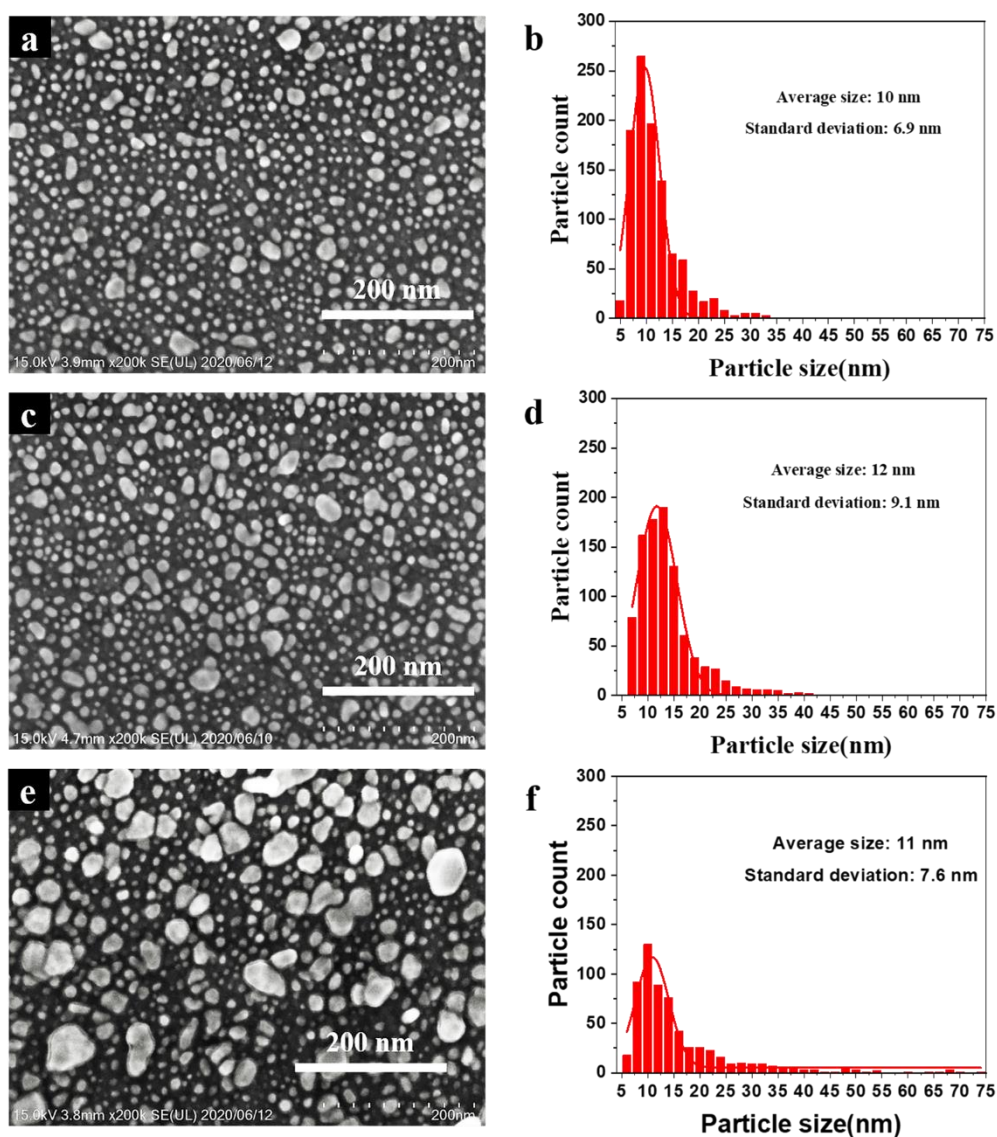


Figure 4.6 Surface morphologies of Au@ATA with different electrochemical

deposition time. (a) and (b), (c) and (d), (e) and (f) are the SEM images and Au-NPs size distribution with the deposition time of 1 min, 3 min, 8 min, respectively.

In addition, a representative current-time curve recorded on ATA working electrode in $0.1 \text{ mol}\cdot\text{dm}^{-3} \text{ Na}_2\text{SO}_4$ solution with $0.25 \text{ mmol}\cdot\text{dm}^{-3} \text{ HAuCl}_4$ during the electrochemical postdepositing process is plotted into Figure 4.7. After 3 min electrochemical deposition, the overall charge is integrated as $2.7 \times 10^{-4} \text{ C}$. Therefore, 1.40×10^{14} Au are postdeposited on ATA structure. On the other hand, by analyzing the SEM images of Au@ATA with 3 min electrochemical deposition, there are about 1.15×10^{14} Au postdeposited on ATA structure. Therefore, the Faradic efficiency for 3 min deposition was 82.4 %. This result indicates that most of the reductive current is used to postdeposit Au on the original Au-NPs of ATA structure.

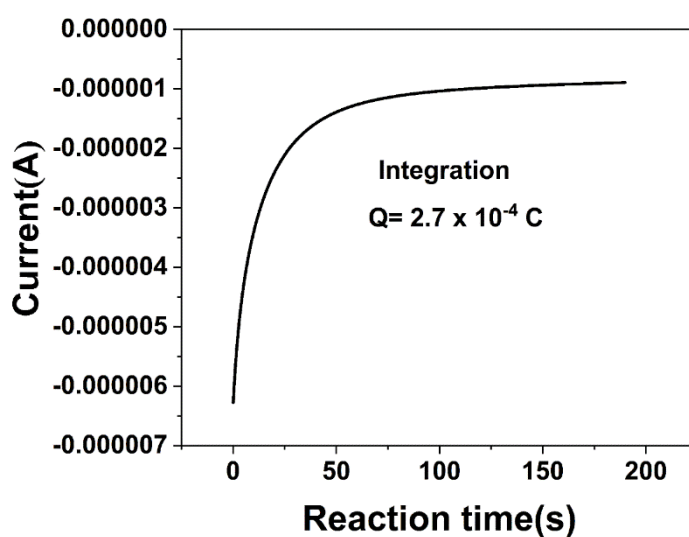


Figure 4.7 The current-time curve recorded on ATA working electrode. The applied potential is + 0.3 V vs SCE.

Therefore, according to the aforementioned analysis result, it can be concluded that the electrochemically postdeposited Au prefers to deposit on the original Au-NPs of ATA structure, and it is negligible for the generation of new Au on TiO_2 film.

Scanning transmission electron microscopy (STEM) images are measured to observe the cross-sectional shape of Au-NPs before and after postdepositing Au. The

results are summarized in Figure 4.8a-4.8d. As shown in Figure 4.8a, the size of the original Au-NPs on ATA structure is about 10 nm and is in accordance with the SEM result. The energy-dispersive X-ray spectrometry (EDX) mapping in Figure 4.8b illustrates that Au-NPs are partially embedded in the TiO₂ film. After postdepositing Au on the original Au-NPs of ATA structure, as shown in Figure 4.8c, the Au-NPs become larger, which are further confirmed by the EDX mapping in Figure 4.8d. It should be mentioned that it is difficult to distinguish the Au-NPs and the postdeposited Au from the STEM image and EDX mapping.³² In line with the parameters of postdeposited Au, platinum (Pt) is electrochemically postdeposited on ATA structures with an applied potential of -0.1 V vs. SCE. Figure 4.8e and 4.8f are the STEM image and EDX of ATA structure with postdeposited Pt (Pt@ATA). It is obvious that small Pt nanoparticles are closely deposited on the ATA structure. The corresponding EDX mapping is given in Figure 4.8f and clearly shows that the Pt nanoparticles are uniformly deposited on the ATA structure. Therefore, from the control experiment of electrochemically postdepositing Pt on ATA, it can be concluded that the original Au-NPs are intimately embraced by the postdeposited metals (Pt, Au). As for the surface morphologies and cross-sections of ATA and Au @ ATA structures, the postdeposited Au is tightly assembled on the original Au-NPs of ATA structure without self-agglomeration. Under this condition, near-field enhancement is expected at the interface between postdeposited Au and TiO₂, as the simulation results summarized in Figure 4.1 and Figure 4.2.

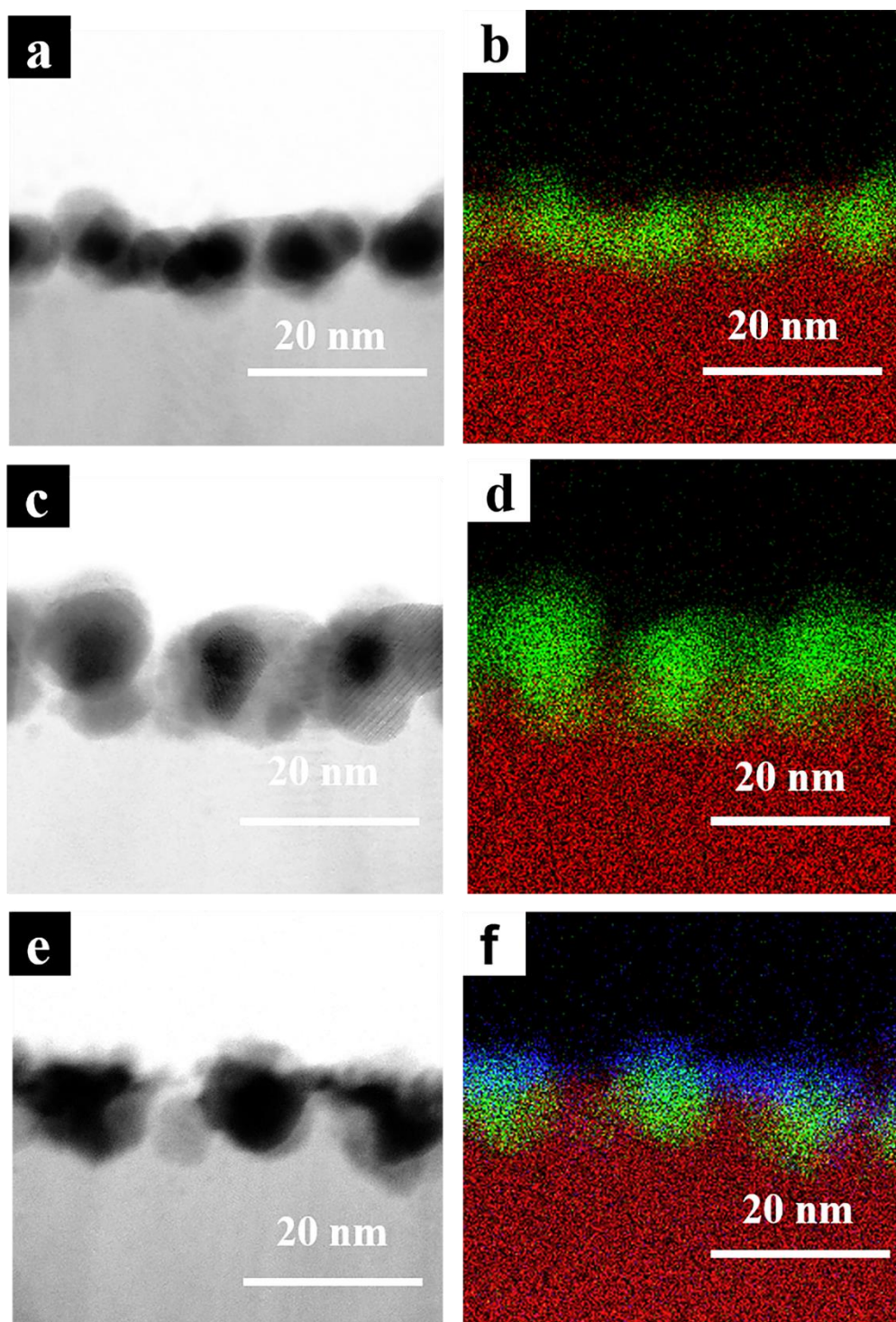


Figure 4.8 (a) and (b) are the STEM image and EDX profile of ATA, (b) and (c) are the STEM image and EDX profile of Au@ATA with 3 min deposition, (e) and (f) are the STEM image and EDX of ATA with electrochemically postdeposited Pt (Pt@ATA). Pt is electrodeposited in presence of $0.25 \text{ mmol}\cdot\text{dm}^{-3}$ H_2PtCl_6 (Chloroplatinic acid hexahydrate) with $0.1 \text{ mol}\cdot\text{dm}^{-3}$ Na_2SO_4 aqueous solution with an applied potential -

0.1 V vs SCE for 3 min. The red, green and blue colours depict TiO₂, Au, Pt, respectively.

4.3.4 Optical properties

Au@ATA structures with different electrochemical deposition times are prepared to evaluate the influence of postdeposited Au on the optical properties of ATA structure, as shown in Figure 4.9. In order to observe the dual bands of Au@ATA structures with different deposition time, the absorbance spectra are obtained by measuring the transmittance T and reflectance R and calculating $-\log(T+R)$, as shown in Figure 4.9a. For all the investigated structures, the absorption with wavelength shorter than 500 nm can be mainly allocated to the interband transition of Au. Obvious dual bands are observed at the wavelength longer than 550 nm, which corresponds to the strong coupling induced energy level splitting into upper and lower modes.²⁵ With prolonging the deposition time, the dual bands can be almost kept. Furthermore, the absorption spectra calculated by $1-T-R$ (Figure 4.9b) can illustrate the absorption intensity of Au@ATA structures with different deposition time. With increasing the deposition time, the absorption spectra at the shorter wavelength bands change inconspicuously and only show slightly redshift. Additionally, more than 98% of the light are absorbed in this regime. However, the longer wavelength bands show blueshift and decreased absorption abilities with prolonging the deposition time owing to the detuning of the strong coupling condition by the postdeposited Au.

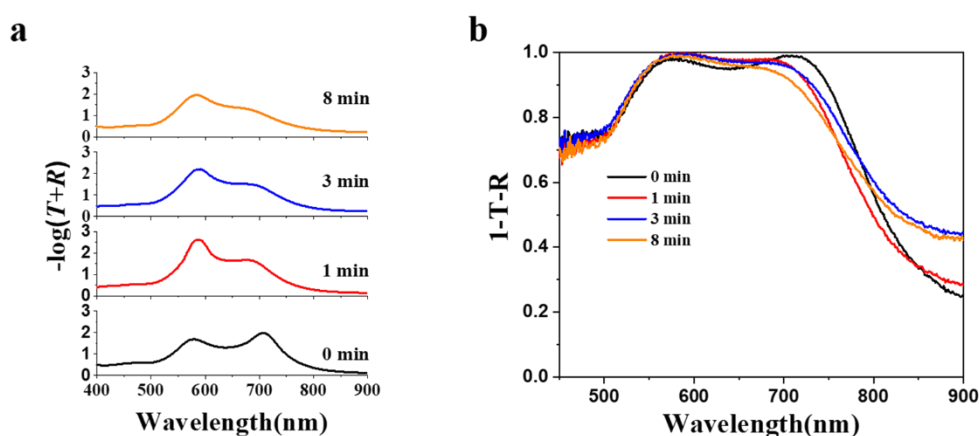


Figure 4.9 (a) Absorbance spectra, calculated using $-\log(T+R)$, (b) absorption spectra,

calculated using $I-T-R$, of the Au@ATA structures with various electrochemical postdeposition times.

Absorbance spectra for ATA and Au@ATA structures with various TiO₂ thicknesses (19~44 nm) are measured in order to further investigate the influence of postdeposited Au on the strong coupling condition. The absorbance spectra are summarized in Figure 4.10. For both ATA structures and Au@ATA structures, the interband transition of Au can mainly affect the upper branch of the splitting absorbance band with TiO₂ thickness smaller than 23 nm. As displayed in Figure 4.10a, obvious dual bands appear at the wavelengths longer than 550 nm. However, When the thicknesses of TiO₂ are larger than 28 nm, the dual bands phenomenon gradually vanish. When the TiO₂ thicknesses reach 38 nm, the dual bands turn into an uncoupled LSPR absorbance band.²⁵ In addition, the distinct dual bands are still obvious at wavelength longer than 550 nm after postdepositing Au on ATA structures (Figure 4.10b).

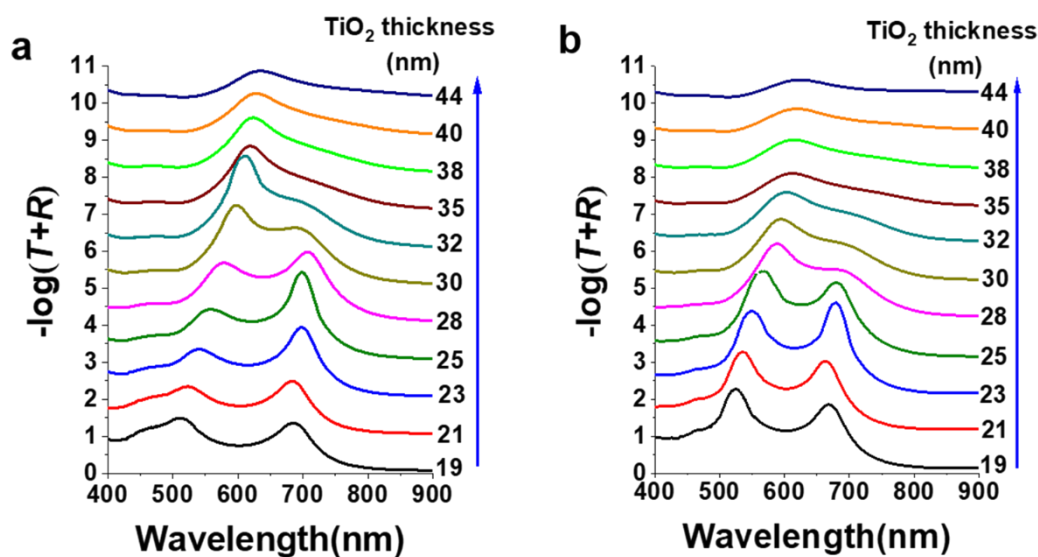


Figure 4.10 Absorbance spectra of (a) ATA and (b) Au@ATA structures with various TiO₂ thin-film thicknesses.

Figure 4.11 shows the dispersion curves by plotting the band energy of the absorbance spectra as a function of the resonant cavity energy. Due to the overlap of the interband transition of Au and the cavity mode at the wavelength shorter than 500

nm, the resonant cavity energy is obtained via peak separation based on the Lorentz fitting. On the basis of the coupled harmonic oscillator model,²⁵ the splitting energy of ATA structures is 340 ± 28 meV, and the splitting energy of Au@ATA structures is calculated to be 310 ± 30 meV. Since the splitting energy of Au@ATA is in proximity to that of ATA structures, it can be concluded that the strong coupling behaviour of Au@ATA is alike to that of ATA structures.²⁵

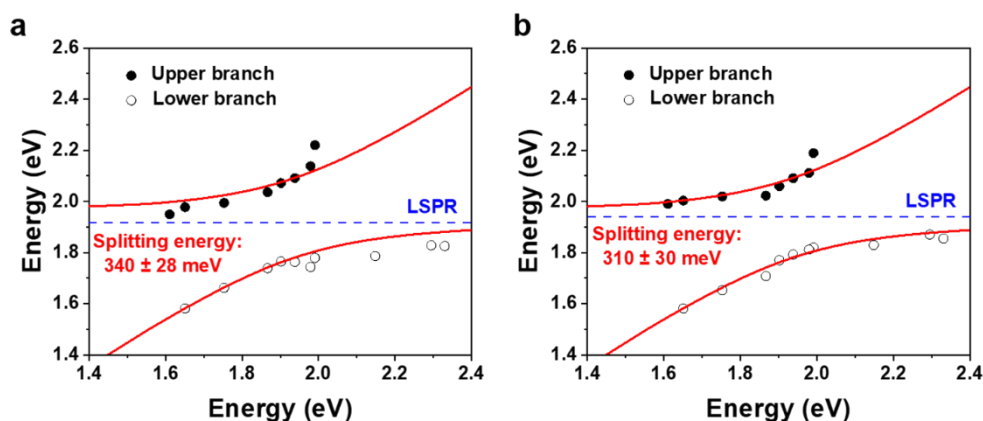


Figure 4.11 Dispersion curves of the splitting absorption band of (a) ATA and (b) Au@ATA. The red curves are the fittings using the coupled harmonic oscillator model. The blue dashed lines are the LSPR energies of the Au-NPs.

4.3.5 Photoelectrochemical activity

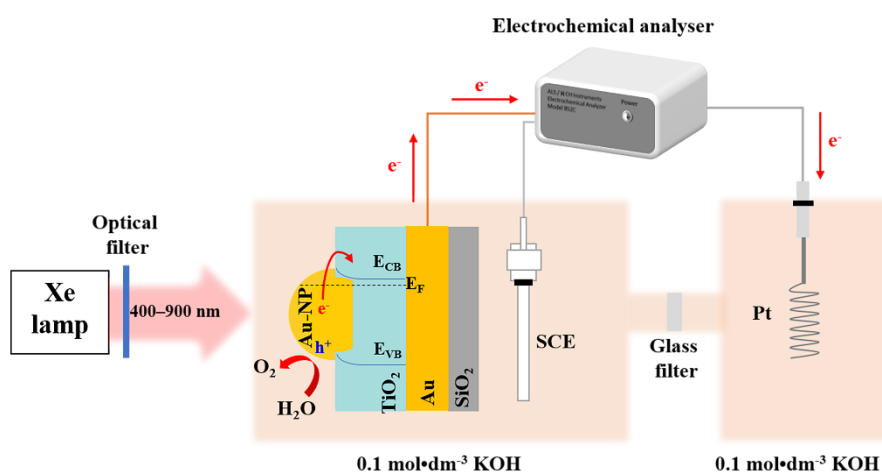


Figure 4.12 Schematic of the three-electrode system used for the photoelectrochemical measurements. E_{CB} and E_{VB} are the conduction band energy and valence band energy of TiO_2 . E_F is the Fermi level energy of Au and TiO_2 .

In order to evaluate the light-to-energy conversion efficiency of Au@ATA structures, the three-electrode system is used to execute the photoelectrochemical measurements (Figure 4.12).³³ What calls for special attention is that no sacrificial electron donor is added to the electrolyte. Therefore, only water participates in the oxidation reaction.

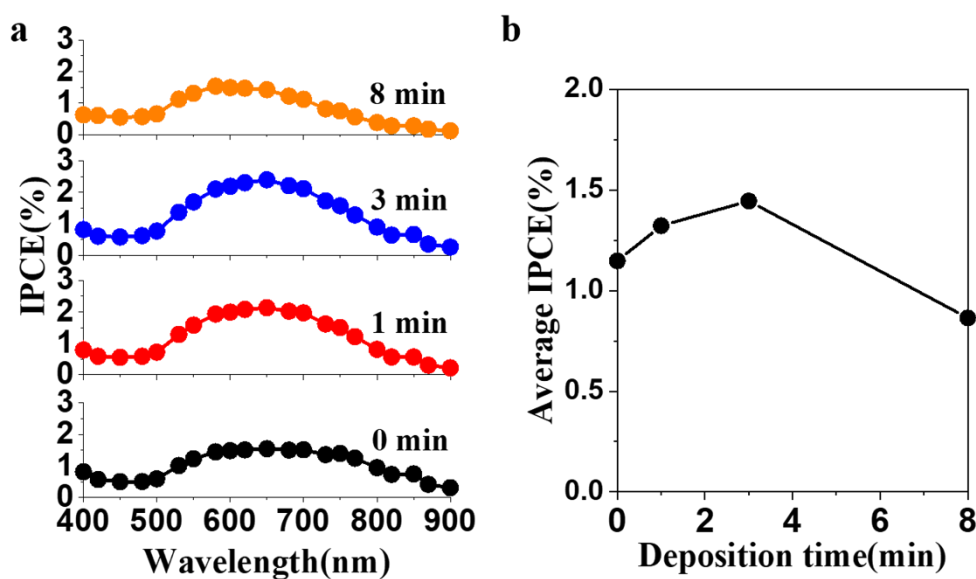


Figure 4.13 (a) IPCE spectra of Au@ATA photoelectrodes with different deposition times. (b) Average IPCE obtained from 500 nm to 900 nm corresponding to (a).

The monochromatic incident photon-to-current conversion efficiency (IPCE) spectra of ATA and Au@ATA are summarized in Figure 4.13a. When Au is postdeposited on the original Au-NPs of ATA structures, the IPCE values of Au@ATA structures gradually improve and reach the maximum values till the deposition time is up to 3 min. And then the IPCE values decrease when the deposition time reaches 8 min. It is interesting that the highest IPCE value of Au@ATA for 3 min deposition is about 2.5 %.

The size effect of Au-NPs on the IPCE increment of Au@ATA structures is firstly investigated in order to verify the significance of the interface generated between postdeposited Au and TiO₂. After the postdeposition of Au on ATA structures, the

average size of Au-NPs is enlarged from 10 nm to 12 nm. According to the experimental results of ATA with large Au-NPs, it can be concluded that the enhancement of the IPCE values is not mainly determined by the size of Au-NPs, as shown in Figure 4.14.

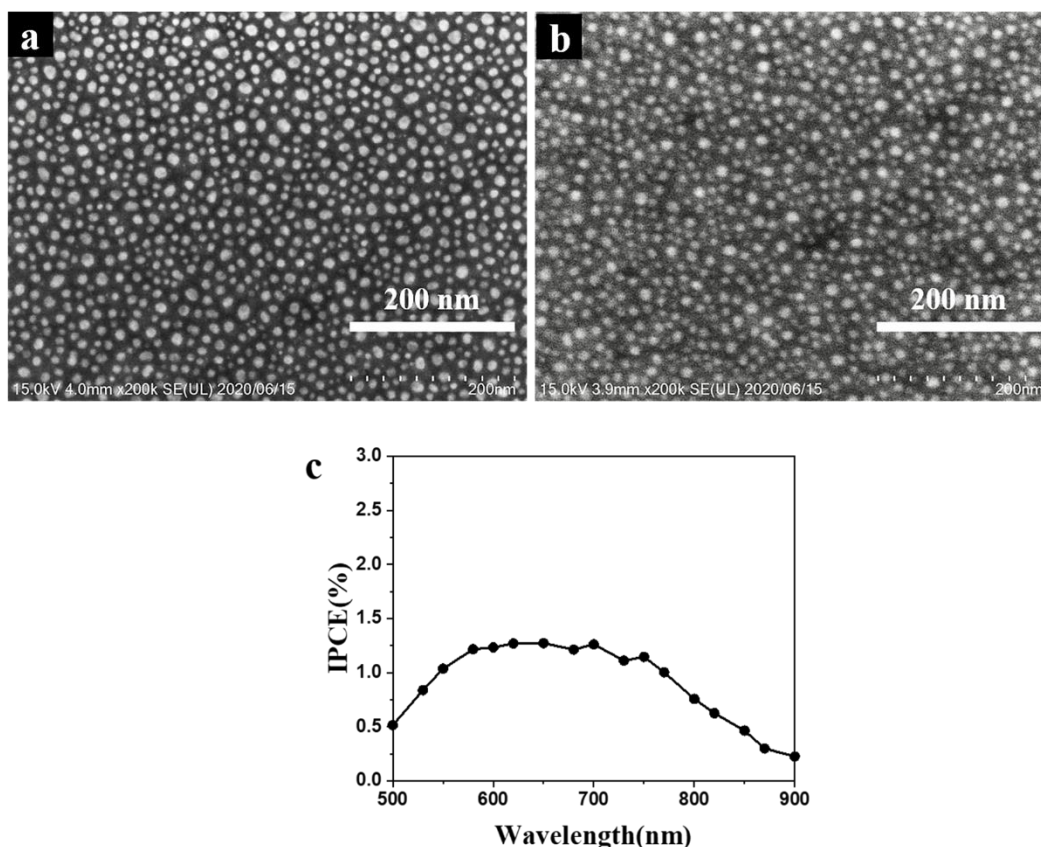


Figure 4.14 ATA with 20 nm Au-NP size and an embedded depth of 7 nm. SEM images before (a) and after (b) 7 nm embedding, (c) IPCE spectrum of the corresponding structure.

Since the generation of photocurrent at the wavelength greater than 500 nm can be ascribed to the plasmon-induced charge separation at the interface of Au-NP/TiO₂,^{26,27} the plasmon-induced water oxidation can be primarily determined by the three-phase boundary generated among Au-NPs, TiO₂ and solution. According to the simulation results in Figure 4.1 and Figure 4.2, As discussed in Figure 4.1 and Figure 4.2, the IPCE increment relates to the intensified near-field generated at the three-phase boundary. It is because the plasmon-induced hot electron-hole pairs are generated at this boundary.

The hot-electrons transfer to the conduction band of the connected TiO₂. And the holes have to transfer to the surface of TiO₂ to oxidize water since Au-NPs are partially embedded in the TiO₂. However, the recombination of holes and electrons may result in adverse effect on the transfer process. As displayed in Figure 4.1 and Figure 4.2, after Au is postdeposited on the original Au-NPs of ATA structure, the intensified near-field can be generated at the interface of postdeposited Au and TiO₂ which is close to the three-phase boundary. For Au@ATA structure, the near-field at the bottom of the original Au-NPs is still high energetic, but the holes generated at this position have to transfer much farther away to oxidize water because of the postdeposited Au. This transfer process may not have contribution to the improvement of IPCE values. Therefore, it can be concluded that the newly generated energetic near-field at the interface of TiO₂ and postdeposited Au and close to the three-phase boundary significantly accelerate the oxidation of water. As displayed in Figure 4.13b, the average IPCE of Au@ATA structure is improved about 1.3 times compared to that of the bare ATA structure. This significant IPCE improvement is beneficial to oxidizing water under visible light irradiation.

When prolonging the deposition time to 8 min, oversized Au nanostructures are generated partially due to the aggregation of the Au-NPs, resulting in a decrease of the IPCE values, which is even lower than that of the ATA structure at wavelength longer than 580 nm. From the SEM results, the total number of Au-NPs for 8 min deposition is decreased compared to that of the ATA structure, from 1023 to 618. Additionally, according to the calculation results from Figure 4.5 and Figure 4.6, the sum of the perimeter of the Au-NPs decreases from 4.1×10^4 nm for 3 min of deposition to 3.1×10^4 nm for 8 min of deposition, which means the effective reaction interface reduced and results in the decrease in the IPCE values. Therefore, for 8 min deposition, the oversized Au-NPs as well as the reduced three-phase boundary leads to the suppressive water oxidation.^{26,27} Moreover, it is much easier for large metal nanoparticles to scatter, which means it is much more difficult for them to absorb light. There is an optimal value for the scattering and absorption, because smaller nanoparticles result in weak absorption

and larger nanoparticles result in strong scattering. However, it is difficult to utilize the absorbed light 100 % and the IPCE values cannot completely correspond to the absorption spectra because there are three factors to determine the IPCE values of the structures: the intensity of light absorption, the efficiency of surface charge separation, and the efficiency of charge transfer to the surface. Furthermore, the IPCE values relate to the energy of incident photons. For example, with 700 nm illumination, the energy of the incident photons is relatively low, thereby most of the electrons cannot overcome the Schottky barrier to transfer to the conduction band of TiO₂ and participate reactions. In this case, the IPCE values are low even the absorption intensity is very strong.

4.4 Conclusions

In summary, a facile constant potential electrolysis technique is demonstrated to tailor the near-field distribution of Au-NPs on the ATA structure. This near-field engineering technology is proved to be beneficial to the water oxidation reaction. It is found that Au prefers to site-selectively postdeposit on the original Au-NPs of ATA structure. The newly generated energetic near-field at the interface of TiO₂ and postdeposited Au plays a vital role in improving the photoelectrochemical performances of the plasmonic nanocomposites. Compared to the average IPCE of ATA structure from 500 nm to 900nm, there is approximately 30 % increment in the average IPCE of Au@ATA structure. Therefore, it can be anticipated that the facile near-field engineering technique will trigger the exploration of more elaborated solar-to-energy systems, which can significantly improve the efficiency of photochemical reactions, such as carbon dioxide reduction, contamination degradation, and water splitting. This part of study can offer an easy and befitting method to further develop viable, superior, as well as low-cost plasmon-induced energy conversion systems.

4.5 References

- [1] K. Li, N. J. Hogan, M. J. Kale, N. J. Halas, P. Nordlander, P. Christopher, *Nano Lett.*, **2017**, *17*, 3710-3717.
- [2] Y. L. Li, Q. Sun, S. Zu, X. Shi, Y. Q. Liu, X. Y. Hu, K. Ueno, Q. H. Gong, H. Misawa, *Phys. Rev. Lett.*, **2020**,

124, 163901-6.

- [3] R. Bukasov, T. A. Ali, P. Nordlander, J. S. Shumaker-Parry, *ACS Nano*, **2010**, *4*, 6639-6650.
- [4] B. Wang, S. C. Singh, H. Y. Lu, C. L. Guo, *Plasmonics*, **2020**, *15*, 609-621.
- [5] W. Y. Tsai, J. S. Huang, C. B. Huang, *Nano Lett.*, **2014**, *14*, 547-552.
- [6] X. C. Ma, Y. Dai, L. B. Yu, B. Huang, *Light Sci. Appl.*, **2016**, *5*, e16017.
- [7] K. Ueno, T. Oshikiri, Q. Sun, X. Shi, H. Misawa, *Chem. Rev.*, **2018**, *118*, 2955-2993.
- [8] M. Kauranen, A. V. Zayats, *Nat. Photonics*, **2012**, *6*, 737-748.
- [9] L. N. Zhou, D. F. Swearer, C. Zhang, H. Robotjazi, H. Q. Zhao, H. Henderson, L. L. Dong, P. Christopher, E. A. Carter, P. Nordlander, N. J. Halas, *Science*, **2018**, *362*, 69-72.
- [10] Lal, S.; Link, S.; Halas, N. J. *Nat. Photonics*, **2007**, *1*, 641-648.
- [11] T. Oshikiri, K. Ueno, H. Misawa, *Angew. Chem. Int. Ed.*, **2014**, *53*, 9802-9805.
- [12] A. Furube, L. C. Du, K. Hara, R. Katoh, M. Tachiya, *J. Am. Chem. Soc.*, **2007**, *129*, 14852-14853.
- [13] S. V. Singh, M. P. Kumar, S. Anantharaj, B. Mukherjee, S. Kundu, B. N. Pal, *ACS Appl. Energy Mater.*, **2020**, *3*, 1821-1830.
- [14] X. M. Zhang, Y. L. Chen, R. S. Liu, D. P. Tsai, *Rep. Prog. Phys.*, **2013**, *76*, 046401 (41pp).
- [15] S. C. Warren, E. Thimsen, *Energy Environ. Sci.*, **2012**, *5*, 5133-5146.
- [16] Y. Tian, T. Tatsuma, *J. Am. Chem. Soc.*, **2005**, *127*, 7632-7637.
- [17] K. Wu, J. Chen, J. R. McBride, T. Lian, *Science*, **2015**, *349*, 632-635.
- [18] C. Clavero, *Nat. Photon.*, **2014**, *8*, 95-103.
- [19] S. Linic, P. Christopher, D. B. Ingram, *Nat. Mater.*, **2011**, *10*, 911-921.
- [20] D. B. Ingram, S. Linic, *J. Am. Chem. Soc.*, **2011**, *133*, 5202-5205.
- [21] M. L. Brongersma, N. J. Halas, P. Nordlander, *Nat. Nanotechnol.*, **2015**, *10*, 25-34.
- [22] Y. Nishijima, K. Ueno, Y. Yokota, K. Murakoshi, H. Misawa, *J. Phys. Chem. Lett.*, **2010**, *1*, 2031-2036.
- [23] X. Shi, K. Ueno, N. Takabayashi, H. Misawa, *J. Phys. Chem. C*, **2013**, *117*, 2494-2499.
- [24] X. Shi, X. W. Li, T. Toda, T. Oshikiri, K. Ueno, K. Suzuki, K. Murakoshi, H. Misawa, *ACS Appl. Energy Mater.*, **2020**, *3*, 5675-5683.
- [25] X. Shi, K. Ueno, T. Oshikiri, Q. Sun, K. Sasaki, H. Misawa, *Nat. Nanotechnol.*, **2018**, *13*, 953-958.
- [26] K. L. Kelly, E. Coronado, L. L. Zhao, G. C. Schatz, *J. Phys. Chem. B*, **2003**, *107*, 668-677.
- [27] P. Reineck, D. Brick, P. Mulvaney, U. Bach, *J. Phys. Chem. Lett.*, **2016**, *7*, 4137-4141.
- [28] P. B. Johnson, R. W. Christy, *Phys. Rev. B*, **1972**, *6*, 4370.
- [29] G. Gotti, K. Fajerweg, D. Evrard, P. Gros, *Electrochim. Acta*, **2014**, *128*, 412-419.
- [30] N. T. K. Thanh, N. Maclean, S. Mahiddine, *Chem. Rev.*, **2014**, *114*, 7610-7630.
- [31] L. Wu, F. Li, Y. Y. Xu, J. W. Zhang, D. Q. Zhang, G. S. Li, H. X. Li, *Appl. Catal. B: Environ.*, **2015**, *164*, 217-224.
- [32] F. X. Xiao, Z. P. Zeng, B. Liu, *J. Am. Chem. Soc.*, **2015**, *137*, 10735-10744.
- [33] Y. Nishijima, K. Ueno, Y. Yokota, K. Murakoshi, H. Inoue, H. Misawa, *J. Phys. Chem. Lett.*, **2012**, *3*, 1248-1252.

Chapter 5 Conclusions and future perspectives

5.1 Conclusions

This thesis is mainly focused on investigating and optimizing a novel modal strong coupling structure between the Fabry-Pérot nanocavity mode (TiO_2/Au -film) and the localized surface plasmon resonance (Au-NPs). Their strong coupling-induced hot electron-hole pairs generation and transfer properties as well as further modification for enhanced photoelectrochemical activities were investigated.

In Chapter 2, the strong coupling nanostructures between the Fabry-Pérot nanocavity mode and the localized surface plasmon resonance were developed based on our previous reports. For these three-dimensional strong coupling Au-NPs/ TiO_2/Au -film (ATA) structures, all the structures exhibited broad and intensive light absorption ability under visible light irradiation. The experimental results illustrated that Au-NPs with a size around 12 nm showed superior properties not only in photoelectrochemical performance but also were economically friendly. The photoelectrochemical measurement showed that the ATA structure exhibited obvious photocurrent enhancement.

In Chapter 3, a further study on the plasmon-induced hot-electron transfer efficiency under the strong coupling conditions was investigated by monitoring the photocurrent generated at the photoelectrode. The effect of the strong coupling on the incident photon-to-current conversion efficiency (IPCE) and internal quantum efficiency (IQE) in the presence of triethanolamine (TEOA) was investigated. With the addition of TEOA, the IPCE values on the upper and lower branches of the strong coupling were enhanced up to 4.5 and 4.0 times, respectively. Furthermore, the average IQE at wavelengths from 500 to 800 nm reached 3%. The Fermi level shifts due to the generation and consumption of hot-carriers were also investigated by comparing the in situ spectroelectrochemical measurements with and without TEOA.

In Chapter 4, a facile constant potential electrolysis technique was developed to

tailor the near-field distribution of Au-NPs on the ATA structure. It was proved that a strong near-field was generated at the interface between the postdeposited Au and the TiO₂ thin film, where the water oxidation reaction could occur effectively. It was discovered that Au prefers to site-selectively postdeposit on the original Au-NPs of ATA structure. The newly generated high energetic near-field at the interface of TiO₂ and postdeposited Au played an important role in boosting the photoelectrochemical activities of the plasmonic nanocomposites. It turned out that the average photocurrent conversion efficiency of Au@ATA was approximately 1.3-fold higher than that of ATA.

5.2 Future perspectives

The most significant discovery in this thesis is that a well-designed and easy-produced plasmon-based strong coupling nanostructures can bring about efficiently broad light absorption, high plasmon-induced hot-electron generation and transfer efficiency, and applicability to sophisticated plasmonic solar-energy devices. These studies will provide a better understanding and unique perspective to constructing strong coupled plasmonic nanostructures with high photoelectrochemical and photocatalytic performances.

Further studies will focus on the applications of the strong coupling plasmonic nanostructure in constructing water splitting devices and carbon dioxide reduction systems. Moreover, the further development and optimization of these strong coupling structures are necessary. For example, mesoporous TiO₂ layers can be fabricated by using solvent evaporation induced self-assembly method or templating method in order to improve the transfer efficiency of plasmon-induced hot carriers. In addition, further optimization of the strong coupled structures for higher photovoltaic performance and photostability via utilizing the plasmon-induced hot spots to deposit metals (such as Au, Pt, Cu) under irradiation.

Publications

1. **Y. F. Cao**, T. Oshikiri, X. Shi, K. Ueno, J. Li, H. Misawa,
“Efficient Hot-Electron Transfer under Modal Strong Coupling Conditions with
Sacrificial Electron Donors”
ChemNanoMat, **2019**, 5,1008-1014. (Chapter 3)
2. **Y. F. Cao**, X. Shi, T. Oshikiri, S. Zu, Y. Sunaba, K. Sasaki, H. Misawa,
“Near-Field Engineering for Boosting the Photoelectrochemical Activity to a Modal
Strong Coupling Structure”
Chem. Commun., **2021**, 57, 524-527. (Chapter 4)